Dynamic Wind Loads on Heliostats

Dynamische Windlasten auf Heliostaten

Von der Fakultät für Maschinenwesen der Rheinisch-Westfälischen Technischen Hochschule Aachen zur Erlangung des akademischen Grades eines Doktors der Ingenieurwissenschaften genehmigte Dissertation

vorgelegt von

Juan Felipe Vásquez Arango

Berichter: Univ.-Prof. Dr.-Ing. Robert Pitz-Paal
Univ.-Prof. Dr.-Ing. habil. Michael Breuer

Tag der mündlichen Prüfung: 1. Dezember 2016

The way of the wind is a strange, wild way.
— Ingram Crockett, *The Wind*

Abstract

This PhD thesis describes a methodology to determine dynamic wind loads on solar concentrators known as *Heliostats*. The methodology, which relies on numerical simulations, has been applied to a conventional heliostat design to predict the response of the structure subjected to the turbulent atmospheric boundary layer (ABL). Large-eddy simulations (LES) have been performed on a simplified model of a heliostat at different elevation angles to predict the time-dependent wind loads. Based on wind data analysis and information from the literature, the ABL has been reproduced at the inlet boundary of the flow simulations by generating synthetic turbulence via the *Vortex Method*. A detailed finite-element (FE) model of an $8\,m^2$ heliostat has been generated and validated with measurements by means of modal analysis. The results from the modal analysis helped to identify the modes most likely to be excited by fluctuating wind loads. The FE model in combination with the damping coefficients determined experimentally have been used to develop a dynamic FE model of the heliostat. The time signals of the pressure loads from the LES have been used as boundary condition in dynamic FE simulations to compute the response of the structure under critical wind conditions. By analyzing the transient FE results, it was found that the contribution of inertial forces and resonance effects is significant in the reaction loads. Moreover, a simplified procedure known as the *Admittance Method* was applied to the heliostat to estimate statistically the response of the structure. The method works in the frequency domain and uses transfer functions to determine the spectral distribution and statistical values of the loads and displacements. Using the load spectra, time signals have been recovered by inverse Fourier transform that provide valuable information for fatigue analysis. In addition, the admittance method was used in combination with wind data to predict the optical error, known as *slope error*, of the heliostat induced by the dynamic wind loads. It was found that the yearly average slope error is insignificant for the operating point considered compared to reference values from the literature.

Kurzfassung

Diese Doktorarbeit beschreibt eine Methodologie zur Bestimmung der dynamischen Windlasten auf solare Konzentratoren den sogenannten *Heliostaten*. Die Methodologie, die auf numerischen Simulationen basiert, wurde auf ein konventionelles Heliostatdesign angewendet, um die Reaktion der Struktur zu ermitteln, die der atmosphärischen Grenzschicht (AGS) ausgesetzt ist. Large-Eddy Simulationen (LES) wurden an einem vereinfachten Model eines Heliostaten bei verschiedenen Elevationswinkeln durchgeführt, um die zeitabhängigen Windlasten vorherzusagen. Anhand der Winddatenanalyse und Literaturdaten wurde die AGS als Einlassrandbedingung in den Strömungssimulationen über synthetische Turbulenzgenerierung mittels der *Vortex Method* abgebildet. Ein detailliertes Finite-Elemente (FE) Modell eines $8\,\mathrm{m}^2$ Heliostaten wurde erstellt und mit Messungen mittels Modalanalyse validiert. Mit Hilfe der Ergebnisse aus der Modalanalyse konnten die Moden identifiziert werden die anfällig sind, von fluktuierenden Windlasten angeregt zu werden. Das FE Modell in Kombination mit den experimentell ermittelten Dämpungskoeffizienten wurden verwendet, um ein dynamisches FE Modell des Heliostaten zu entwickeln. Die zeitabhängigen Signale der Drucklasten aus den LES wurden als Randbedingung in den dynamischen FE Simulationen verwendet, um die Antwort der Struktur unter kritischen Windbedingungen zu berechnen. Bei der Analyse der transienten FE Ergebnisse wurde festgestellt, dass der Beitrag der Trägheitskräfte und der Resonanzeffekte zu den Reaktionslasten signifikant ist. Darüber hinaus wurde ein vereinfachtes Verfahren, bekannt als *Spektralverfahren*, auf den Heliostat angewendet, um die Strukturantwort statistisch abzuschätzen. Das Verfahren arbeitet im Frequenzbereich und verwendet Übertragungsfunktionen, um die spektrale Verteilung und statistischen Werte der Lasten und Verschiebungen zu ermitteln. Unter Verwendung der Lastspektren wurden Zeitsignale mittels inverser Fourier Transformation zurückgewonnen, die wertvolle Information für die Dauerfestigkeitsanalyse liefern. Außerdem wurde das Spektralverfahren in Kombination mit Winddaten benutzt, um den optischen Fehler des Heliostaten, der durch dynamischen Windlasten induziert wird, vorauszuberechnen. Es wurde herausgefunden, dass der jährlich gemittelte optische Fehler für den betrachteten Betriebspunkt im Vergleich zu Referenzwerten aus der Literatur nicht signifikant ist.

Acknowledgments

I would like to thank the following people for their help and support during the course of this work that made it possible:

To Prof. Robert Pitz-Paal for giving me the opportunity to carry out this PhD work, for his patience and guidance during the last years and for the review of the manuscript. To Prof. Michael Breuer for his role as a supervisor of the PhD, for his valuable feedback on the numerical part and for his detailed review of the manuscript. To Dr. Reiner Buck for providing me the freedom and appropriate working environment to accomplish this project and for the review of the manuscript.

To Andreas Pfahl for his support and engagement in projects related to this investigation. To Fabian Wolfertstetter and Stefan Wilbert for providing me the meteorological data. To my current and former colleagues Phillip Liedke, Stefano Giuliano, Michael Wittmann, Fabian Feldhoff, Edgar Teufel and Csaba Singer for their support and advices. To the Center of Computing and Communication of the RWTH Aachen University for the invaluable IT support. To Prof. Jan Wörner and the DLR executive board for the grant for this work.

And finally, to my family and friends for encouraging me to achieve this PhD.

Contents

Nomenclature

Abbreviations

ABL	atmospheric boundary layer
CDS	central differencing scheme
CFD	computational fluid dynamics
CSP	concentrating solar power
CVs	control volumes
CWE	computational wind engineering
DLR	Deutsches Zentrum für Luft- und Raumfahrt
DNS	direct numerical simulation
DOF	degree of freedom
FDM	finite-difference method
FE	finite-element
FRF	frequency response function
FSM	fractional step method
FST	free-stream turbulence
FVM	finite-volume method
LES	large-eddy simulation
MDOF	multi-degree of freedom
OMA	operational modal analysis
PDF	probability density function
PSA	Plataforma Solar de Almeria
PSD	power spectral density
RANS	Reynolds-averaged Navier-Stokes equations
RFP-Z	rational fraction polynomial method
RMS	root-mean-square
SGS	subgrid-scale
SIMO	single-input multiple-output
SIMPLEC	semi-implicit method for pressure-linked equations consistent
VM	vortex method
WALE	wall-adapted local eddy viscosity

Roman letters

Symbol	Description	Units
a	general variable	[[a]]
A	area	[m^2]
b	plate width	[m]
c	chord length	[m]
$[C]$	damping matrix	[Ns/m]
C_d	drag coefficient	[-]
CFL	Courant-Friedrichs-Lewy number	[-]
C_l	lift coefficient	[-]
C_{mx}	moment coefficient about x_t-axis	[-]
C_{my}	moment coefficient about x-axis	[-]
C_p	pressure coefficient	[-]
DNI	direct normal irradiance	[W/m^2]
e	Euler number	[-]
f	frequency	[Hz]
f_n	natural frequency	[Hz]
F	general wind load	[N]
F_l	lift force	[N]
F_d	drag force	[N]
GHI	global horizontal irradiance	[W/m^2]
G_{M_y}	gain factor of moment about y-axis	[-]
h	height of heliostat in horizontal position	[m]
h_0	average height of roughness elements	[m]
H_{M_y}	transfer function of moment about y-axis	[-]
I	total turbulence intensity	[-]
I_u	turbulence intensity of longitudinal velocity component	[-]
I_v	turbulence intensity of lateral velocity component	[-]
I_w	turbulence intensity of vertical velocity component	[-]
k_a	peak factor of variable a	[-]
k_t	turbulent kinetic energy	[m^2/s^2]
k_u	gust factor	[-]
k_x	rotational stiffness about x_t-axis	[Nm/rad]
k_y	rotational stiffness about y-axis	[Nm/rad]
$[K]$	stiffness matrix	[N/m]
l	length	[m]
L	characteristic length	[m]
$[M]$	mass matrix	[kg]

M_x	moment about x_t-axis	[Nm]
M_y	moment about y-axis	[Nm]
$M_{y,out}$	reaction moment about y-axis	[Nm]
n	normalized frequency	[-]
p	static pressure	[Pa]
p_b	static pressure on bottom surface of plate	[Pa]
p_t	static pressure on top surface of plate	[Pa]
p_∞	free-stream static pressure	[Pa]
r	displacement	[m]
r_z	displacement in z_n-direction	[m]
Re	Reynolds number	[-]
R_M	mass Rayleigh parameter	[1/s]
R_K	stiffness Rayleigh parameter	[s]
s	plate thickness	[m]
S_a	power spectral density of variable a	$[[a]^2/Hz]$
S_{ij}	rate of strain tensor	[1/s]
St	Strouhal number	[-]
t	time	[s]
$T_{M_{y,out}}$	ratio of standard deviation to mean value of $M_{y,out}$	[-]
u	x-component of velocity	[m/s]
u_i	velocity vector	[m/s]
u_τ	friction velocity	[m/s]
u^+	normalized velocity	[-]
$\overline{u'^2}$	x-component of the Reynolds stresses	$[m^2/s^2]$
U	mean wind speed	[m/s]
U_h	mean wind speed at height h	[m/s]
U_∞	free stream (reference) velocity	[m/s]
v	y-component of velocity	[m/s]
$\overline{v'^2}$	y-component of the Reynolds stresses	$[m^2/s^2]$
w	z-component of velocity	[m/s]
$\overline{w'^2}$	z-component of the Reynolds stresses	$[m^2/s^2]$
x, y, z	Cartesian coordinates	[m]
x_i	position vector	[m]
x_t	tangential coordinate	[m]
y_n	wall-normal coordinate	[m]
y^+	normalized wall-normal distance	[-]
z_0	roughness height	[m]
z_n	wall-normal coordinate	[m]

Greek letters

Symbol	Description	Units
α	elevation angle, angle of attack about y-axis	[deg]
β	wind angle, angle of attack about x_t-axis	[deg]
γ	Euler constant	[-]
Γ_i	circulation	[m^2/s]
δ	angular deviation of the mirror surface normal vector	[rad]
δ_x	angular deviation about x_t-axis	[rad]
δ_y	angular deviation about y-axis	[rad]
Δp	pressure difference	[Pa]
Δt	time step	[s]
Δx	cell dimension	[m]
ε	turbulent dissipation rate	[m^2/s^3]
η	spatial distribution of vortices	[m]
κ	von Kármán constant	[-]
κ	wave number	[rad/m]
λ	eigenvalue	[rad^2/s^2]
μ	molecular viscosity	[kg/(m s)]
ν	kinematic viscosity	[m^2/s]
ν_t	subgrid-scale (eddy) viscosity	[m^2/s]
ξ	damping ratio	[-]
ρ	fluid density	[kg/m^3]
σ_a	standard deviation of variable a	[[a]]
σ_a^2	variance of variable a	[[a]^2]
τ	time scale, time lag	[s]
τ_0	wall shear stress	[N/m^2]
τ_{ij}^s	subgrid-scale stress tensor	[N/m^2]
ϕ	phase angle	[rad]
$\{\phi_i\}$	eigenvector	[m]
Φ	vortex size	[m]
$\lvert\chi_{aero}(f)\rvert^2$	aerodynamic admittance function	[-]
$\lvert\chi_{mech}(f)\rvert^2$	mechanical admittance function	[-]
ψ	blending parameter	[-]
ω	eigenfrequency	[rad/s]
ω_x	x-component of the vorticity vector	[1/s]

Notations

Symbol	Description
$\dot{a}$	first time-derivative
$\ddot{a}$	second time-derivative
$\widetilde{a}$	resolved quantity
$\overline{a}$	time-averaged quantity
$\lvert a \rvert$	magnitude
$\hat{a}$	peak value
a'	fluctuating part
$\breve{a}$	complex quantity

1. Introduction

1.1. Motivation and literature review

Concentrating solar power (CSP), in combination with thermal energy storage, is a feasible alternative to conventional fossil fuel power plants for the generation of electricity and reduction of the global CO_2 emissions. One of the most promising technologies among CSP plants is the solar tower. Its main advantage, compared to other technologies, is the large concentration of solar radiation which leads to high overall efficiencies. The concentration is done by a large number of mirrored collectors called *Heliostats*. They track the sunlight during the day and focus it onto a heat exchanger, called *receiver*, located at the top of a central tower. At the receiver, the solar radiation is converted into heat and transferred to a fluid to produce steam, which is used to power a steam turbine that drives an electrical generator.

Heliostats are one of the main components of solar power tower plants. They represent about 40% of the total investment costs [1]. Hence, optimizing current designs to reduce the costs of this component is a key task for the power tower technology. When designing heliostats, it is essential to provide reliable loading data for dimensioning the structure and its components, especially the drives. The data includes information about static loads for designing against over-stressing, as well as dynamic loads to account for structural failure caused by fatigue. This data is also required to estimate the effect of wind loads on the pointing accuracy of the concentrators influenced by motions of the frame and deviations in the surface contour.

In the past, most investigations on heliostats dealt with mean and peak wind loads. Nevertheless, some of these investigations pointed out the importance of dynamic loads. In [2], the potential impact of fatigue loading was indicated from the range of maximum to minimum loading found experimentally, as well as by the existence of fluctuating loads that involved sign changes and large amplitude excursions. In [3] the following reviewer comment was cited: *I must highly emphasise to designers of large pedestal supported arrays that resonant vibrations must be considered. In our earlier designs, we experienced several drive failures in the field when only static wind loads were considered in the design. Naturally we were forced to consider dynamic effects to correct the problems.*

Only a few studies have investigated specifically dynamic wind loads on heliostats. In [4], a $37\,\mathrm{m}^2$ heliostat was tested in a large wind tunnel at high wind speeds and different operating points. They measured dynamic loads using accelerometers and identified the operating condition of the maximal load. The work was focused on the investigation of

the maximal operational wind speed, but did not consider turbulence fluctuations in the flow, which is an essential component in the study of dynamic wind loads.

More recently in [5], aeroelastic measurements were performed based on a 14.4 m^2 heliostat used in a commercially available power plant. Field observations of heliostat prototypes were the reason for the investigation and modification of conventional design procedures to include dynamic loads. The experiments were conducted in a wind tunnel using a 1:7 scale aeroelastic model designed to reproduce the first three modes of vibration. One subject of the investigation was the study of aerodynamic phenomena such as *galloping* and *flutter*, which are dynamic instabilities in one or two degrees of freedom, respectively. They occur when the aerodynamic forces act to reinforce motion in a dynamic mode and more energy is put into each cycle than can dissipate by structural and aerodynamic damping [6]. For the horizontal (stow) position of the mirror frame at wind speeds of up to 40 m/s, which are typically foreseen in the design, the results did not exhibit any signs of such instabilities. While the results obtained from such measurements may well reproduce the dynamic behavior of the structure, the experiments are associated with difficulties in the fabrication of a suitable model that possesses the same dynamic properties as the full-scale structure and the calibration of the wind tunnel to model the turbulence characteristics of the atmospheric boundary layer correctly.

In [7–10] a 37 m^2 U-shaped heliostat structure was investigated. Initially in [7], they conducted numerical and experimental modal analysis to determine the dynamic properties of the structure and validate a FE model. Later in [8], operational modal analysis (OMA) were accomplished to examine the dynamic behavior of the structure under real operating conditions. They found that the natural frequencies under wind speeds between 4-13 m/s were in very close agreement to the previous study and that the aerodynamic damping is very small under these conditions, with less than 0.3% of the critical damping. One of the difficulties associated to OMA in wind engineering applications, is the uncontrollable boundary conditions that lead to long extensive measurement campaigns in order to collect sufficient data under desired wind conditions. Similarly to aeroelastic measurements, the results obtained from OMA are only applicable to the specific structure investigated. An attempt to predict the wind loads by CFD simulations in the heliostat field was done in [9]. The numerical results compared to wind measurements inside the field show a significant overprediction of the wind loads, presumably due to the use of unsuitable turbulence models (which are not specified in the article) for such complex flows. Large discrepancies between simulations and experiments are also found in the prediction of the dynamic loads in [10]. They performed transient simulations on the validated FE model using synthetically generated load signals. The loads were generated by simply translating synthetic velocity signals into pressure loads using empirical load coefficients and then applying them on the mirror facets of the heliostat.

A similar investigation as above on a 120 m^2 conventional heliostat is found in [11]. Wind tunnel measurements were performed as well as full-scale field measurements to determine the wind loads experimentally. In addition, CFD simulations were performed

on a single heliostat and on a heliostat field section. Unfortunately, no information is given about the numerical methodology, but apparently transient simulations were performed. The CFD results were then coupled to a FE model to predict the dynamic response of the structure and then compared to full-scale field measurements. Most of the results presented have a qualitative character and show that the simulations over-predict the full-scale measurements.

There are no specific wind load guides for heliostats. For this reason, heliostat designers usually rely on the pioneer work [2, 3] mentioned before to determine mean and peak wind loads. To account for dynamic effects, experimental investigations are occasionally performed for particular heliostat structures as described above. Since such experiments are not always feasible, heliostat designers might fall back on standards commonly used in wind engineering [12, 13] to determine wind loads. These codes include simplified procedures to detect aerodynamic instabilities and resonance effects which are based on empirical parameters that depend on the shape and dynamic characteristics of the structure. Since such wind codes were conceived for buildings and civil engineering structures that differ significantly from conventional heliostats, the input parameters given in the codes are not suitable for the structural and geometrical characteristics of heliostats.

1.2. Objectives

Due to the difficulties and limitations of the experimental methods mentioned above and the absence of useful guides and procedures, alternatives to predict dynamic loads and the associated response of heliostat structures are needed. Unlike previous investigations, the present work focuses on the development of suitable numerical models to predict dynamic wind loads on heliostats. A methodology to tackle the problem is presented, which describes the interaction between various areas of analysis involved. It includes the generation of realistic wind conditions based on wind data analysis, the development and validation of a structural finite-element (FE) model that reproduces the dynamic properties of the structure, the simulation of wind loads via computational fluid dynamics (CFD) and the dynamic response analysis using FE simulations. Moreover, a simplified procedure is proposed to estimate the dynamic loads and response of the structure.

The main objective of this work is to define a general approach that can be applied to any heliostat structure to determine dynamic wind loads and study their effects on design and optical efficiency. To describe the methodology, a full-scale heliostat prototype with a conventional design commonly found in commercial power plants, was examined. Even though it is intended to provide the necessary information to evaluate the structural design against fatigue, no effort was taken to conduct such an analysis on the heliostat investigated, as it was developed for research purposes only. This type of analysis is, however, the final goal when applying the methodology on commercially available designs to be optimized.

1.3. Outline

The thesis starts with the theoretical background in Chap. 2 that summarizes the physical phenomena involved in this investigation and describes the numerical methods used. After that, a brief description of the problem is given and the methodology proposed to model dynamic loads is presented in Chap. 3. In the following chapters, the single components of the methodology are surveyed, starting with wind data analysis in Chap. 4, followed by numerical and experimental modal analysis in Chap. 5, flow and dynamic simulations in chapters 6 and 7 and a simplified method to predict dynamic loads in Chap. 8. Each of these chapters starts with a brief introduction and ends with a conclusion section to help keep the overview of the investigation. In Chap. 9 the thesis is summarized and the main conclusions are drawn. The document is finalized with the appendices that contain mathematical definitions and results of preliminary simulations that might be useful to readers aiming to perform similar studies.

2. Theoretical background

2.1. Wind loads on structures

Structures exposed to wind experience aerodynamic forces that can lead to mechanical failure if they are not accounted for correctly in the design process. Two types of mechanisms can be distinguished in the mechanical failure of a structure. One occurs when exceeding the maximal stress that the material can sustain, and the other is the repeated application of lower stresses that lead to fatigue failure. The former is associated with mean and peak values of the wind-induced forces, while the latter depends on the fluctuating part of the loads. Depending on the type of stress analysis to be performed and the reaction of the structure to the wind loads, a static approach or a more elaborated dynamic analysis needs to be conducted.

Apart from structural failure, deflections are often a design concern that must be considered in the analysis. In heliostat designs only small angular deviations of the ideal surface normal vector, known as *slope error*, are allowed to achieve high optical efficiencies of the heliostat field. This quantity is usually given by the standard deviation of the nominal direction. For cost efficient heliostat designs, slope errors of about 1 mrad are recommended [14]. Typical values ranging between 1-2 mrad are found in [15].

2.1.1. Static wind loads

If only mean and peak values of the stresses and displacements are of interest, a static approach is sufficient in the calculation of the wind loads. In most wind engineering applications, the inertial part of the wind forces dominate over viscous forces and the resulting wind loads can be determined from the pressure distribution on the surface of the body. For simple body shapes, normalized load coefficients can be found in wind codes [12] to estimate the effective loads. For non-conventional structures, wind tunnel measurements are usually accomplished on scaled model to determine these load coefficients. The following definitions are commonly used:

$$C_p = \frac{p - p_\infty}{\frac{1}{2}\,\rho\, U_h^2}, \qquad C_l = \frac{F_l}{\frac{1}{2}\,\rho\, U_h^2 A}, \qquad C_d = \frac{F_d}{\frac{1}{2}\,\rho\, U_h^2 A}, \tag{2.1a}$$

$$C_{mx} = \frac{M_x}{\frac{1}{2}\,\rho\, U_h^2 A\, b} \quad \text{and} \quad C_{my} = \frac{M_y}{\frac{1}{2}\,\rho\, U_h^2 A\, c}, \tag{2.1b}$$

where C_p is the pressure coefficient determined from the pressure difference between surface pressure and static pressure of the incoming flow $p - p_\infty$, divided by the dynamic

pressure $\frac{1}{2}\,\rho\,U_h^2$ computed from the air density ρ and the square of the mean wind speed at a reference height U_h. The lift coefficient C_l relates the vertical force F_l to the dynamic pressure multiplied by a characteristic area of the body A. Similarly, the drag coefficient is defined from the along-wind force F_d. The moment coefficients C_{mx} and C_{my} relate the moments about the longitudinal and lateral axis, respectively, with the dynamic pressure multiplied by a characteristic area A and lever arm b or c. The normalization of the forces and moments is based upon the linear relationship between the aerodynamic forces and the dynamic pressure, and can be used to determine the forces on geometrically similar bodies. The load coefficients are given as mean values over a period of time usually taken as 10 minutes. During this period, turbulent fluctuations can generate considerably higher loads above the mean values. The sources of the fluctuations are: the atmospheric turbulence and self-induced turbulence that depends on the body shape. If the latter is negligible, the so called *gust factor* approach [16] can be used to estimate maximal loads $\hat{F}$ based on the mean load $\overline{F}$ and the standard deviation σ_u of the wind speed as follows:

$$\hat{F} = \overline{F}\left(1 + k_u\, 2\,\frac{\sigma_u}{U_h}\right), \tag{2.2}$$

where k_u is the gust factor typically in the range between 3 and 5 [17].

2.1.2. Dynamic wind loads

Dynamic wind loads originate from the interaction between the time-dependent pressure on the surface of a structure and its dynamic characteristics, i.e. inertia, elasticity and damping. Two main sources of dynamic loads are of special interest in the present study: buffeting forces and wake-induced forces. Buffeting forces arise from pressure fluctuations induced by turbulence in the oncoming flow, whereas wake-induced forces are unsteady loads caused by the structure's own wake acting on the afterbody. They are also termed vortex shedding forces [18].

In case of flexible structures, magnification of the loads and displacements can occur when these turbulence phenomena induce oscillations near the natural frequencies of the structure. In such cases, a full description of the fluctuating loads and the dynamic behavior of the structure is pursued in order to determine if resonance effects are possible. This is accomplished by a dynamic analysis, where the main objective is to obtain the transient response of the structure under the action of fluctuating loads. The response of a structure includes information about deflections and stresses, which is essential for fatigue analysis and evaluation of design criteria regarding deformations.

A dynamic analysis requires an accurate description of the time-dependent quantities implicated in the problem. One alternative to investigate dynamic loads is in wind tunnels using aeroelastic models which are scaled according to modeling laws described in [18]. Sometimes these models can be very simple and it is sufficient to represent the dynamic behavior by a fundamental mode of vibration. However, in complex structures, it is necessary to reflect higher modes in the model to reproduce the dynamic behavior.

Quasi-steady approach

Analytical procedures can be developed for the treatment of turbulence-induced wind forces. These procedures use information of the turbulent flow and translate these into transient loads using quasi-steady aerodynamics. The quasi-steady approach links the transient wind loads to the time-dependent velocity by using the definition of the mean load coefficients. Applied to the drag force, it reads:

$$F_d(t) = \frac{1}{2}\,\rho\,A\,C_d\,u^2(t), \tag{2.3}$$

where $u(t)$ is the fluctuating longitudinal velocity component. This practical model assumes that the body in question is sufficiently small compared to the correlation distances of the velocity fluctuations [19].

Admittance method

For large structures, and in the presence of flow separation, the assumption of full correlation between velocity and load fluctuations in the model above does not hold and adjustment functions are introduced to account for the reduced spatial correlation. The approach, known as the admittance method [6], is illustrated in Fig. 2.1 according to [20]. It works entirely in the frequency domain and uses statistical quantities like standard deviations and spectral densities to describe wind velocities, forces and deflections. The main calculations are done in the bottom row, in which the total mean square fluctuating response (variance) is computed from the spectral density of the response. The latter is calculated from the spectrum of the aerodynamic forces, which are, in turn, calculated from the wind turbulence, or gust spectrum. The frequency-dependent aerodynamic and mechanical admittance functions form links between these spectra [21].

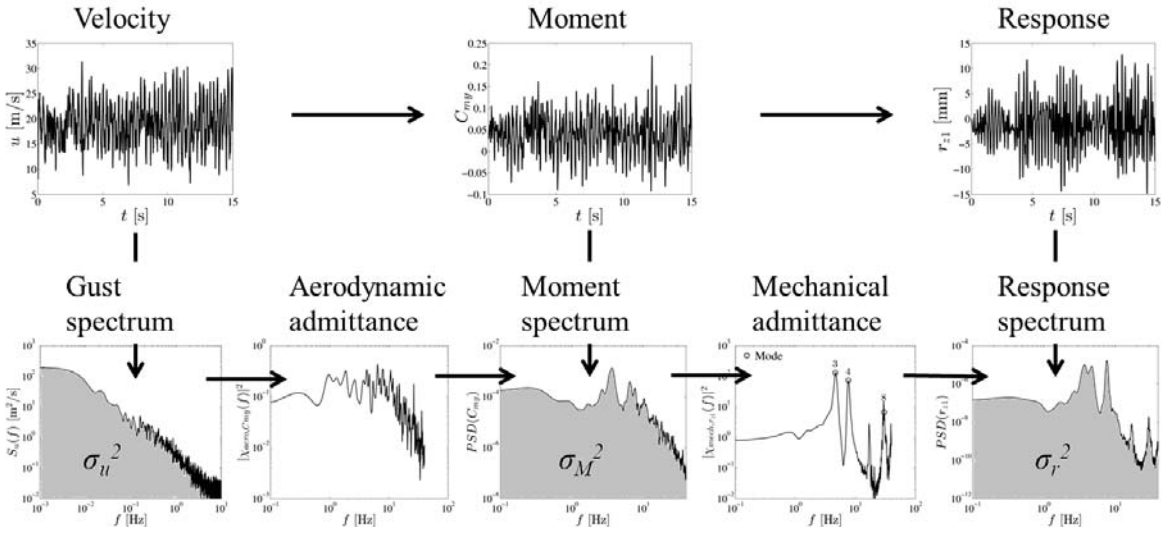

Figure 2.1.: Admittance method [20].

The admittance functions are usually determined experimentally for a given structure and can then be used to estimate load and response spectra from the turbulence spectrum and mean values of the velocity, load and displacement. The accuracy of the method is reasonable and the discrepancies are generally small and always conservative [6]. In Sect. 8.2 the method will be applied for to present application.

A less common alternative to determine dynamic wind loads is by direct measurement on the real object. Full-scale measurements are of no direct use to the designer. Nonetheless, they play an important role in the verification of model accuracy and calibration of wind codes and building regulations [6]. This can be accomplished by combining techniques from OMA to monitor the operating deflections on the structure and simultaneously recording the wind conditions to describe the response to the fluctuating wind as was proposed in [8]. For a complete dynamic analysis, information about the time-dependent loads is also required. A simultaneous measurement of the time-dependent pressure distribution on the surfaces of the structure can be conducted as in [22, 23]. However, maintaining sensitive electronics and keeping manometers air- and water-tight in field conditions complicates full-scale measurements. Calibration of the tubing system and preservation of sufficient frequency resolution is also a challenge for the experiments.

Numerical methods known as computational wind engineering (CWE) constitute a further alternative to study dynamic wind loads. They have gained popularity in the last decades due to enormous advances in computing performance. CWE is a very promising technique that can provide load and response information at much higher resolutions than conventional experimental techniques and thus, help to understand physical phenomena that require detail examination. It combines CFD and FEM methods that are well known from other applications in aerodynamics and structural mechanics. A detailed description of the methods will be given in Sect. 2.3 and 2.5.

2.1.3. Fatigue loading

Material failure caused by repetitive application of loads that are below the yield point is called fatigue. When a flexible structure is subjected to a large number of load cycles (typically above 10^4 for steel) with stress magnitudes within the elastic range, a type of fatigue loading, termed high-cycle fatigue, can occur. The main sources of high-cycle fatigue in wind engineering applications are buffeting loads and vortex shedding. They have variable amplitudes and are random in nature. For this reason, the fatigue life of the structure can not be determined directly from the well known S-N curve (Wöhler-diagram) for the material used. It is necessary to convert the complicated time-history of a real structure into some equivalent number of individual stress cycles for the evaluation of their cumulative effect [24]. A cumulative damage hypothesis called *Miner's rule* [25] is often selected for this purpose. The rule requires an appropriate counting method of the individual load cycles. The *rainflow counting* method [26] is a widely used method. It uses the time history of the stress amplitude to determine the number of individual load cycles. Hence, the time evolution of the loads needs to be estimated by calculations

or from measurements to apply the method.

2.1.4. Effects of Reynolds number

The most important quantity in the description of turbulence is the Reynolds number Re. It is the ratio of inertial forces to viscous forces acting on the fluid and is defined as:

$$Re = \frac{\rho U L}{\mu}, \tag{2.4}$$

where ρ is the fluid density, U a characteristic velocity, L a characteristic length and μ the dynamic viscosity. When Re is large, inertial forces predominate and the flow is turbulent, while low values of Re indicate a laminar flow. When modeling wind loads experimentally or numerically, the dimensions of the object investigated or the velocities that it is exposed to, are usually reduced in order to conduct the investigations at reasonable costs. This reduction yields Reynolds numbers much lower than the original problem. In order to provide results that can be scaled to real dimensions and be useful for design purposes, it is necessary to determine the influence of Re on the quantities of interest.

The effects of the Reynolds number on aerodynamic forces have been studied extensively in the past and are well-known for flows over bodies with simple geometries. These effects are closely related to flow separation. Flow separation occurs when the fluid in the boundary layer is sufficiently decelerated by inertial forces that the flow near the surface becomes reversed [19]. Separation takes place in the presence of adverse pressure gradients found, for example, in the flow over a corner or a curved surface. When flow separation is present, its location determines the pressure distribution on the surface of the body and thus, the integral forces.

On rounded bodies, the location of the separation is determined by the curvature and the state of the boundary layer. For small Re, the boundary layer is laminar, and the flow separates early. At higher Re, the separated laminar boundary layer undergoes transition to turbulence some small distance downstream from the separation point [27]. A turbulent boundary layer is capable of overcoming larger adverse pressure gradients by enhancing entrainment of the much more energetic surrounding fluid. This causes flow separation to take place at a later streamwise position for higher Re. A later separation narrows the wake region of lower pressure and reduces the drag forces.

The position at which flow separates is fixed for bodies with sharp edges. For this reason, aerodynamic forces are independent of Re at relatively low values. Re independent drag coefficients were found in [28] for square cylinders with sharp edges at $Re > 2.0 \times 10^4$, in [29] for circular and square flat plates at $Re > 1.0 \times 10^4$ and in [30] reported by [31] for a normal plate at $Re > 6.0 \times 10^4$. These findings suggest that wind load studies on objects with sharp edges can be extrapolated from Reynolds numbers in the order of 10^4 and above.

2.1.5. Effects of free-stream turbulence

Another factor that affects wind loads is turbulence in the oncoming flow, also known as free-stream turbulence (FST). FST is present in the natural wind and contains a wide range of turbulence scales. Low frequency velocity fluctuations control the instantaneous pressure on the upstream face of a body and are the origin of buffeting forces.

Small-scale turbulence, on the other hand, influences the mean flow around the body itself and thus, the mean pressure distribution. Thereby, two mechanisms are involved: transition and mixing. In the presence of FST, the laminar boundary layer over the surface of a body undergoes transition to turbulence at lower Re than for a smooth flow. This is a consequence of the excitation of the boundary layer by the effects of turbulence entrained into it and by pressure fluctuations in the free-stream [27]. In separated flows over curved surfaces this effect is comparable to an increase in Re and has, therefore, a similar influence as mentioned in Sect. 2.1.4 on the position of separation and thus, on the aerodynamic forces.

Turbulent mixing takes place in shear layers by the interaction of the two turbulent fields. The spreading rate of a shear layer is increased by the action of the normal component of FST [27]. In separated flows, where the wake region is bounded by the shear layer, fluid particles from the outer region with higher kinetic energy entrain into the wake region as result of the enhanced mixing. Unlike the effects of small-scale turbulence and Reynolds number, turbulent mixing affects also the flow over bodies with sharp edges. In measurements on flat plates normal to a turbulent flow [32] and on a long cylinder of square cross-section [33], the effects of FST were observed by an increase in the pressure difference between front and back surfaces. This is the result of a stronger suction in the wake region. For elongated bodies, such as plates with rectangular cross-section or obstacle with a large length to height ratio, where reattachment is possible, the increased entrainment always curves the separated shear layer inward towards the body [27]. A decrease in the reattachment length was observed for such cases in [34–36].

Based on the observations mentioned above, it can be concluded that FST needs to be accounted for in the determination of wind loads. For this reason, it has been included in wind tunnel measurements and also in design procedures found in wind codes for a long time. However, FST still constitutes a great challenge in approaches based on flow simulations, due to the complexity involved in modeling turbulence.

2.2. Atmospheric boundary layer

Wind is induced by pressure differences in the atmosphere. In the vicinity of the earth's surface, the moving air is affected by frictional forces that decelerate the wind. This effect decreases with height and becomes negligible at a height above the ground called *gradient height*. This height is typically 1000 m or about 10% of the height of the troposphere, but may range between 200 m and 5000 m [18]. The region below this

height is the *atmospheric boundary layer* (ABL).

2.2.1. Mean velocity profile

The ABL can be broken down into at least two sublayers, principally the *surface layer*, in which the shearing stress is approximately constant, and a transition region in which the shearing stress falls off from the constant value of the surface layer to the practically zero value in the free atmosphere [37]. Another simplifying feature of the surface layer is that wind direction remains more or less constant with height [18]. In the surface layer, which extends up to roughly 100 m, the wind velocity profile $U(z)$ appears to be accurately defined by Prandtl's logarithmic profile (log-law) [37]:

$$U(z) = \frac{u_\tau}{\kappa} \ln\left(\frac{z}{z_0}\right), \tag{2.5}$$

where z is the height above the ground, z_0 is the roughness height, $\kappa = 0.4$ is the von Kármán constant and u_τ is the friction velocity defined by

$$u_\tau = \sqrt{\frac{\tau_0}{\rho}}, \tag{2.6}$$

where ρ is the air density and τ_0 is the wall shear stress.

The most important parameter in Eq. (2.5) is z_0. It depends on the roughness characteristics of the terrain: the nature, height and distribution of roughness elements [19]. Over a rough terrain, the wind is subjected to higher frictional forces compared to a flat terrain. The resulting shear stress is responsible for the generation of turbulence in the surface layer. The turbulence motions detract kinetic energy from the mean flow. This affects the velocity gradient which is larger on flat terrains. Thus, under the same conditions outside the ABL, the mean wind speed at a given height is larger for lower z_0.

In practice, u_τ and z_0 are determined by fitting the log-law to measured values of the mean wind speed over the height. Values of z_0 for a variety of natural surfaces are given in [18]. For a so-called *open terrain*, which represents a farmland with low vegetation and few trees, z_0 lies between 1 cm and 10 cm.

Equation (2.5) is not expected to remain valid for such low heights z_0, which fall well below the tops of the individual roughness elements characterizing the surface. The assumptions made in deriving Eq. (2.5) can not be justified for $z < h_0$, where h_0 is the average height of roughness elements. The ratio z_0/h_0 falls within a range between 0.03 and 0.25 [18].

Weather conditions also have an impact on the wind velocity. Solar radiation absorbed by the surface during the daytime increases free convection and is responsible for the diurnal variations of the atmospheric pressure. This, in turn, causes variations in the wind velocity whose maximum occurs during the daytime and is reached before the maximum

of the air temperature, while its minimum occurs at night [18]. Long term observations have shown annual variations of the horizontal mean wind speed as well. In continental regions, a main maximum can be found in winter, and a main minimum in summer [18]. The horizontal mean wind speed U fits a Weibull distribution very well [16]. Hence, the Weibull probability density function PDF(U) in Eq. (2.7) can be used to estimate annual extreme velocities.

$$\mathrm{PDF}(U) = b\,\frac{U^{b-1}}{a^b}\,e^{-\left(\frac{U}{a}\right)^b}, \tag{2.7}$$

where a and b are the scale and shape parameters, respectively.

2.2.2. Atmospheric turbulence

Turbulence is characterized by random variations of the velocity field in time and space[1]. The reason for the randomness, is the high sensitivity of the flow to perturbations when inertial forces acting on the fluid particles are large enough to overcome the constraining effect of viscosity, which is given at high Reynolds numbers. In the atmosphere, these conditions prevail almost always, in particular in the ABL which is the region of greatest interest in wind engineering [18].

Due to the random nature of turbulence, statistical methods are used to describe the fluctuating components of the wind in the ABL. The main statistical characteristics are the turbulence intensity, the power spectral density and the probability distribution. The simplest descriptor of atmospheric turbulence is the turbulence intensity I. It is defined as the ratio of the standard deviation σ of the velocity components to the mean velocity $U(z)$ as follows:

$$I_u(z) = \frac{\sigma_u}{U(z)}, \qquad I_v(z) = \frac{\sigma_v}{U(z)} \quad \text{and} \quad I_w(z) = \frac{\sigma_w}{U(z)}, \tag{2.8}$$

where the subscripts u, v and w indicate the longitudinal, lateral and vertical components, respectively. Observations suggest that the standard deviations are almost constant in the surface layer. For an homogeneous open terrain, they are approximately [16]:

$$\sigma_u \approx 2.5 \times u_\tau, \qquad \sigma_v \approx 0.75 \times \sigma_u \quad \text{and} \quad \sigma_w \approx 0.5 \times \sigma_u, \tag{2.9}$$

where u_τ is the friction velocity. From Eq. (2.5) and Eq. (2.9) it follows that the turbulence intensity is related to the roughness height z_0 and the height above the ground z as:

$$I_u(z) = \frac{1}{\ln\left(\frac{z}{z_0}\right)}. \tag{2.10}$$

[1] However, within the apparently chaotic turbulent flows organized or *coherent* structures exist [38], as well as correlations between the fluctuating velocity components. That the velocity field is random only means that it does not have a unique value, which is the same every time the flow is analyzed under the same conditions [39, p. 34].

Turbulence as a stationary stochastic process is described in its most general form by the probability density function of the velocities. Experiments have shown that in fully developed (homogeneous, isotropic) turbulence, this function is closely described by a normal (or Gaussian) distribution [18]. For the longitudinal velocity component it reads:

$$\mathrm{PDF}(u) = \frac{1}{\sqrt{2\pi}\,\sigma_u}\, e^{-\frac{(u-\overline{u})^2}{2\sigma_u^2}}, \tag{2.11}$$

where $\overline{u}$ is the mean value.

The spectral distribution of the velocity fluctuations describes the contribution to the total variance of the time signals of the velocity attributed to individual frequencies. It is also known as power spectral density or energy spectrum. Figure 2.2 shows the spectrum of horizontal wind speed over a wide frequency range according to van der Hoven [40]. The spectrum is based on measurements over several months and contains contributions at very different scales. A major peak is found at about a 4-day period, which is the typical transit period of fully developed weather systems [6]. At a twelve hour period there is a minor peak corresponding to the lulls in wind speed which generally occur at sunrise and sunset [37]. These two peaks are found in the so called *macro-meteorological range*. A second major peak, comprising a range of higher frequencies which are associated with the turbulence of the boundary layer [6], is found in the period from about 5 minutes to less than 5 seconds termed *micro-meteorological range*. Between periods of 5 minutes and about 4-5 hours the spectrum contains very little energy implying that there is very little variation in wind speed occurring at these rates [37]. This well defined gap is called the *spectral gap* [6].

The existence of the spectral gap permits the independent assessment of the macro-

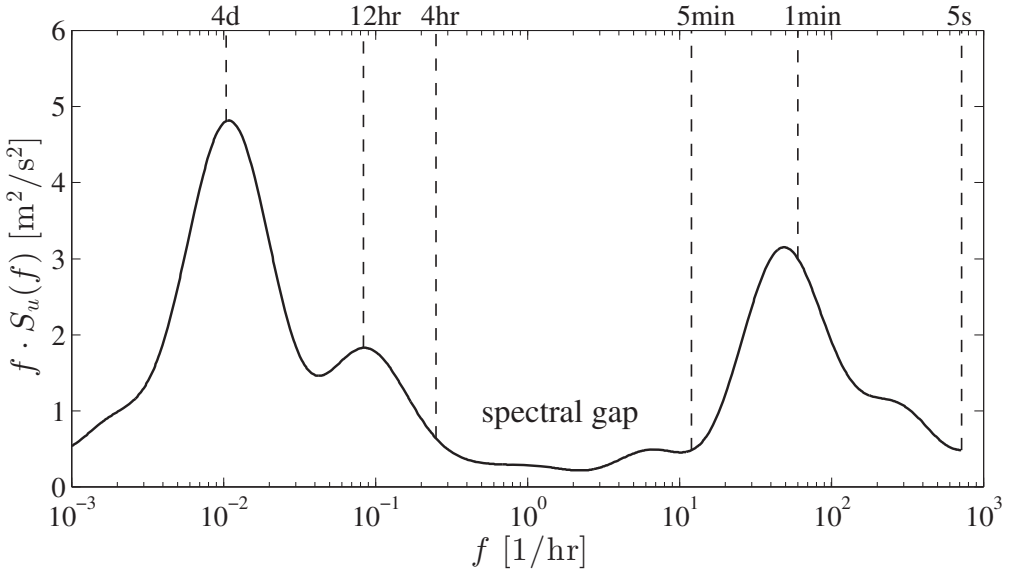

Figure 2.2.: Spectrum of horizontal wind speed by van der Hoven [40].

and micro-meteorological processes affecting wind. In most wind engineering applications only micro-meteorological processes are relevant, as they contain contributions in scales in the order of magnitude of the dimensions of structures and can, therefore, affect wind loading significantly. For this reason, statistical quantities to describe wind velocity are usually based upon periods above 5 minutes.

Empirical formulas based on a variety of wind measurements at different heights and over various terrains have been proposed in the literature to approximate the energy spectra of the individual velocity components. The formulas used in the present work to estimate the spectral distributions of the longitudinal and lateral components S_u and S_v are found in Kaimal et al. [41] and for the vertical component S_w in Panofsky et al. [42]. They are given in normalized form as:

$$\frac{fS_u(f)}{u_\tau^2} = \frac{200\,n}{(1+50\,n)^{5/3}}, \tag{2.12}$$

$$\frac{fS_v(f)}{u_\tau^2} = \frac{15\,n}{(1+9.5\,n)^{5/3}}, \tag{2.13}$$

$$\frac{fS_w(f)}{u_\tau^2} = \frac{3.36\,n}{1+10\,n^{5/3}}, \tag{2.14}$$

where f is the frequency in [Hz] and $n = fz/U$ is the non-dimensional frequency normalized by the height z and mean wind speed U. The power spectral densities (PSD) are computed by Fourier transforms and describe the frequency distribution of the squared magnitudes of the complex Fourier coefficients. The PSD has a unit of $[(\mathrm{m/s})^2/\mathrm{Hz}]$, and its integral over the frequency is equal to the variance:

$$\sigma_u^2 = \int_0^\infty S_u(f)df. \tag{2.15}$$

2.3. Flow simulation

In the present work it is assumed that the flow is incompressible, i.e. the density is constant in space and time. The fluid motion is, therefore, described by the incompressible continuity equation (2.16) representing the conservation of mass, and the incompressible Navier-Stokes (NS) equations (2.17) representing the conservation of momentum. Derivation of these equations can be found in [43]. They constitute a system of partial non-linear differential equations and can be written in the differential form using index notation ($i, j = 1, 2, 3$) in Cartesian coordinates as:

$$\frac{\partial u_i}{\partial x_i} = 0, \tag{2.16}$$

$$\frac{\partial u_i}{\partial t} + \frac{\partial\left(u_i u_j\right)}{\partial x_j} = -\frac{1}{\rho}\frac{\partial p}{\partial x_i} + \frac{\partial}{\partial x_j}\left[\nu\left(\frac{\partial u_i}{\partial x_j} + \frac{\partial u_j}{\partial x_i}\right)\right], \tag{2.17}$$

where u_i is the velocity vector, t the time, x_i the Cartesian coordinates, p the pressure, ρ the density and ν the kinematic viscosity. Analytical solutions of the equations above are only possible for a few flows with very simple boundary conditions. For this reason the equations are usually discretized by means of Finite-Volume (FVM) or Finite-Difference (FDM) methods and then solved by numerical algorithms. A detailed description of the numerical methods can be found in [43]. Before discretization, different adjustments of the conservation equations are commonly applied. They differ significantly in computational costs and modeling complexity and can be distinguished by the scales of turbulence being resolved or modeled.

Turbulent flows can be viewed as a superposition of eddies of different sizes and frequencies [38]. Their contribution to the total turbulent kinetic energy k_t can be examined in the energy spectrum. Figure 2.3 shows a model spectrum of isotropic turbulence [39] as a function of the wave number $\kappa = 2\pi/l$ where l is the characteristic length of the eddies. For a given Reynolds number of 2×10^6 the energy spectrum is divided in three distinctive regions according to [39]. The majority of k_t (about 80%) is found in the *energy-containing range* which is characterized by large eddies. They draw their energy from the velocity gradients in the mean flow and transfer it, through vortex stretching, to smaller eddies in a cascade process where energy is passed successively to smaller eddies. This process takes place in the *inertial subrange* and extends up to the *dissipation range*, where the energy is dissipated to heat by the action of viscosity. The energy spectrum has a universal form, depending only on the Reynolds number of the flow [44]. As *Re* increases, the separation between large and small scales increases as shown in Fig. 2.3. This implies the existence of a wide range of length and time scales in turbulent flows for most practical engineering applications.

In a direct numerical simulation (DNS) the discretized NS equations are solved without

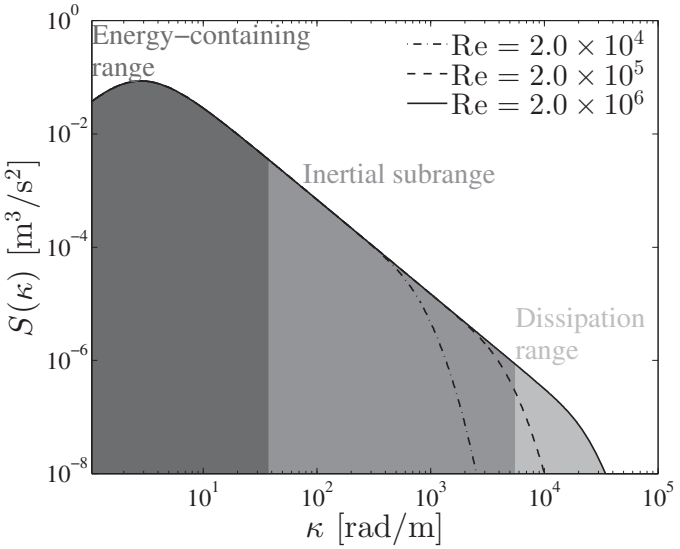

Figure 2.3.: Energy spectrum of isotropic turbulence [39].

any previous treatment. Hence, it requires resolving all turbulence scales existing in the flow. Due to the wide range of turbulence scales present in most practical engineering problems (including the present work), DNS leads to prohibitively expensive computations. Therefore, DNS is normally used only for fundamental investigations on very simple flows at low Re.

Different approaches for the NS equations have been proposed to model the unresolved scales of motion at high Re. The most popular group of CFD methods are based on the Reynolds-Averaged Navier-Stokes (RANS) equations. They are derived by time averaging the NS equations and then applying empirical models to describe the unknown terms (Reynolds stresses) that arise from the procedure. RANS methods model all scales of turbulence and are therefore very useful at high Re. They provide results for mean quantities with engineering accuracy at moderate cost for a wide range of flows [45]. However, in situations dominated by large-scale anisotropic vortical structures like wakes of bluff bodies, the averaged quantities are often less satisfactory when a RANS model is employed [46]. Moreover, the time averaging implied in RANS disqualifies the method for predicting unsteady phenomena such as fluctuating forces caused by turbulence.

A more appropriate method for time-dependent three-dimensional turbulent flows is the Large-Eddy Simulation (LES). It performs generally better than RANS and bears less modeling uncertainties [46]. The concept of LES arises from the fact that large eddies tend to be highly anisotropic and quite variable from flow to flow [47], whereas small eddies are much more universal and nearly isotropic. The basic idea is that large eddies cannot and should not be modeled, but the small eddies might be modeled successfully [47]. The objective of LES is to resolve only the large eddies, containing the majority of k_t, and reproduce the dissipative effects of the small eddies by using relatively simple models. LES is comparably more expensive than RANS methods, but not quite as DNS. Thanks to the advances in high-performance computing in recent years, LES has gained popularity in many industrial applications, including wind engineering problems. Due to its capabilities, LES has been chosen for the present investigation and will be described in the following section.

2.3.1. Large-eddy simulation

The LES method is based on a filtering operation, i.e., a spatial averaging of the velocity field. The filter width, which is usually defined by the local grid spacing, separates the large- and small-scale turbulence. The large scales are computed explicitly, whereas the small scales necessarily are modeled [47]. The filtered NS equations read:

$$\frac{\partial \widetilde{u}_i}{\partial t} + \frac{\partial \left(\widetilde{u}_i \widetilde{u}_j\right)}{\partial x_j} = -\frac{1}{\rho}\frac{\partial \widetilde{p}}{\partial x_i} + \frac{\partial}{\partial x_j}\left[\nu\left(\frac{\partial \widetilde{u}_i}{\partial x_j} + \frac{\partial \widetilde{u}_j}{\partial x_i}\right)\right] - \frac{\partial \tau_{ij}^s}{\partial x_j}, \tag{2.18}$$

where the tildes denote the resolved large-scale quantities. The subgrid-scale (SGS) stress $\tau_{ij}^s = \widetilde{u_i u_j} - \widetilde{u}_i \widetilde{u}_j$ must be introduced to approximate the term $\widetilde{u_i u_j}$ that arises from filtering the non-linear term on the left-hand side of Eq. (2.17) and that can not be

computed explicitly. The effect of τ_{ij}^s is somehow comparable to the Reynolds stresses in the time-averaged equations; here it represents the effect of SGS eddies on the large-scale eddies. Since the predominant role of the small-scale eddies is to act as acceptors of energy and to dissipate it, they are modeled using the eddy viscosity concept which relies on the Boussinesq approximation and is derived from dimensional analysis yielding:

$$\tau_{ij}^s - \frac{1}{3}\delta_{ij}\tau_{kk}^s = -\nu_t \left(\frac{\partial \widetilde{u_i}}{\partial x_j} + \frac{\partial \widetilde{u_j}}{\partial x_i} \right), \tag{2.19}$$

where the trace τ_{kk} is lumped into a modified pressure [48] and the SGS viscosity ν_t is determined, in the present work, by the Wall-Adapted Local Eddy (WALE) viscosity model [49]. It is specifically designed to return the correct wall-asymptotic variation of the SGS viscosity [50] that vanishes at solid walls where the turbulent fluctuations drop to zero. It is also effective in separated shear layers remote from walls as shown in [48].

LES simulations require special attention to the selection of the numerical methods. It is necessary to use numerical schemes of at least second-order of accuracy and with low numerical dissipation. For the discretization of the convective terms the central differencing scheme is usually recommended [51]. The convergence behavior of LES is very sensitive to the grid quality. Block-structured hexahedral grids are usually selected with low cell expansion ratios (<1.1). Orthogonal grids are recommended with smooth transitions between blocks. Grid resolution is one of the most important parameters. Specially at the walls, the resolution should be fine enough to resolve the boundary layer with the first grid point usually placed in the viscous sublayer. About 80% of the turbulent kinetic energy should be resolved according to [39]. As this condition is not easy to verify, it is best practice to perform grid dependence tests and evaluate quantities such as velocity profiles, Reynolds-stresses and eddy viscosity ratios. The temporal resolution is as important as the grid resolution and has an effect on the convergence behavior as well as on the solution itself. The time step can be estimated based on the Courant-Friedrichs-Lewy number CFL defined as

$$CFL = \frac{\Delta t}{\frac{\Delta x_{min}}{u_{max}}}, \tag{2.20}$$

where u_{max} is the maximum velocity, Δt the time step and Δx_{min} the minimum cell dimension. With the restriction $CFL < 1$, a fluid particle can not move more than one cell length in a single time step [43].

The LES in the present work are performed using the commercially available CFD code ANSYS Fluent R15.0 [52]. Details on the selected numerical methods are given in Sect. 6.1.2.

2.3.2. Synthetic turbulence

The importance of accounting for FST in the prediction of aerodynamic forces was already mentioned in Sect. 2.1.5. For this purpose, several methods have been implemented

in the past in combination with LES. An extensive review of the methods available can be found in [53]. The underlying idea of the methods is to artificially generate velocity fluctuations and add them to the mean flow field at the inlet plane. The main challenge in the development of such methods is the generation of a turbulence field that possesses prescribed statistical characteristics and is realistic enough to retain them throughout the flow field.

A method originally proposed in [54] called the *vortex method* (VM) has been further developed and tested in [55] on a variety of flows with comparably better performance than other methods. In the VM, a perturbation is added on a specified mean velocity profile via a fluctuating two-dimensional vorticity field (two-dimensional in the $y-z$-plane normal to the streamwise direction x). The method is based on the 2D transport equation of the vorticity:

$$\frac{\partial \omega_x}{\partial t} + (\vec{u} \cdot \nabla)\omega_x = \nu \nabla^2 \omega_x, \tag{2.21}$$

where ω_x is the component of the vorticity vector in the streamwise direction. Equation (2.21) is solved using a particle discretization in a Lagrangian form (neglecting viscous terms). The center of the vortices $\vec{x}_i$ are convected randomly on the 2D plane of section area A. The amount of vorticity of each of the N number of vortices is represented by the circulation Γ_i and the spatial distribution η as:

$$\omega_x(\vec{x}, t) = \sum_{i=1}^{N} \Gamma_i(t) \eta(|\vec{x} - \vec{x}_i|, t) \tag{2.22}$$

with

$$\Gamma_i(y, z) = 4\sqrt{\frac{\pi A \, k_t(y, z)}{3N(2\ln(3) - 3\ln(2))}}, \tag{2.23}$$

$$\eta(\vec{x}) = \frac{1}{2\pi\Phi^2}\left(2e^{-\frac{|x|^2}{2\Phi^2}} - 1\right) 2e^{-\frac{|x|^2}{2\Phi^2}}. \tag{2.24}$$

Γ_i is determined locally by the level of turbulent kinetic energy $k_t(y, z)$. The size of the vortices is given by Φ which is specified by a mixing length hypothesis as:

$$\Phi = {C_\mu}^{3/4} \frac{{k_t}^{3/2}}{2\epsilon}, \tag{2.25}$$

where $C_\mu = 0.09$ and ϵ is the turbulent dissipation rate. The velocity field is obtained from the Biot-Savart law, formulated in discretized form by:

$$\vec{u}(\vec{x}) = \frac{1}{2\pi} \sum_{i=1}^{N} \Gamma_i \frac{(\vec{x}_i - \vec{x}) \times \vec{e}_x}{|\vec{x} - \vec{x}_i|^2} \left(1 - e^{-\frac{|\vec{x} - \vec{x}_i|^2}{2\Phi^2}}\right) e^{-\frac{|\vec{x} - \vec{x}_i|^2}{2\Phi^2}}, \tag{2.26}$$

where $\vec{e}_x$ is the unit vector in streamwise direction. The streamwise velocity fluctuation u' is computed from a linear kinematic model by:

$$u' = -\vec{u} \cdot \vec{e}_z, \tag{2.27}$$

where $\vec{e}_z$ is the unit vector aligned with the mean velocity gradient. A rescaling procedure is available in the CFD code Fluent [52] to prescribe the normal Reynolds stress components $\overline{u_i'^2}$ according to:

$$u_i'^* = u_i' \sqrt{\frac{\overline{u_i'^2}}{\frac{2}{3}k_t}}. \tag{2.28}$$

The sign of the circulation of each vortex is changed randomly after each characteristic time scale τ, which is the time necessary for a 2D vortex to travel a distance 100 times its mean characteristic size. The vortices move randomly at each time step with a characteristic velocity equal to 5% of the mean inflow velocity. The value of these model parameters are fixed based on numerical testing [55].

The following steps are performed during calculation:

1. Initialize randomly vortex positions $\vec{x}_i$
2. Compute the circulation Γ_i from the prescribed turbulent kinetic energy k_t
3. Compute the local vortex size Φ from the prescribed k_t and ϵ
4. Compute tangential and normal fluctuations u_i'
5. Rescale fluctuations from the prescribed normal stresses $\overline{u_i'^2}$
6. Add fluctuations to the mean velocity profile
7. Move randomly each vortex
8. Change randomly the sign of Γ_i every $\tau/\Delta t$ time steps
9. Go back to 2.

2.4. Modal analysis

Modal analysis is a process to describe a structure in terms of its natural characteristics - its dynamic properties [56]. The dynamic properties depend on the mass distribution, stiffness and damping and are described by the *modal parameters*. The modal parameters are the *natural frequencies*, the *mode shapes* and the *damping ratios*. When a structure is subjected to a transient force with a rate of oscillation close to the natural frequencies, the response amplitude is increased compared to the same input force at a different frequency. This phenomenon is called *resonance*. The deformation patterns of the structure at resonance are the mode shapes. When the force is released, the amplitude of the vibrations decreases. This is mainly caused by friction between the components of the structure and internal energy dissipation in the material. The rate at which the amplitude decreases is described by the damping ratio.

Modal analysis is primarily a tool for deriving reliable models to represent the dynamics of structures. A broad range of applications can be found for modal analysis such as: identification and evaluation of vibration phenomena, development of experimentally based dynamic models, validation of analytical and numerical models that may be used with confidence in further analysis [57].

2.4.1. Experimental modal analysis

The experimental determination of the modal parameters is accomplished by exciting the structure with a quantified force and measuring simultaneously the response of the structure. The input force is measured by a force transducer while the output response is usually measured by an accelerometer. Both time signals of the force and the acceleration are transformed in the frequency domain via a Fast Fourier Transform (FFT) algorithm. The ratio of the output to input signal is called the Frequency Response Function (FRF). The FRF are complex functions which can be easily converted to magnitude and phase. The natural frequencies are extracted from the peak magnitudes of the FRF. The phase information is used to determine the mode shapes by combining a set of FRF. In order to resolve the mode shapes accurately, the FRFs are measured at different positions and directions called Degree of Freedom (DOF). The required number (N) of DOFs depends on the complexity of the structure and the objectives of the tests. Preliminary numerical simulations can help to determine the number and locations of the DOFs.

The position and direction of the output response is called reference DOF. In order to capture multiple modes, it is necessary to define more than one reference DOF, otherwise it is possible that the response at a single reference DOF is too weak or even zero for a given mode shape. This type of measurements are called multi-reference and are performed by exciting the structure at different positions while measuring the response at multiple fixed locations simultaneously. If an impact hammer, with a force transducer attached to it, is used for this purpose, the type of measurement is called Single-Input-Multiple-Output (SIMO).

A fundamental assumption in modal analysis is a linear behavior of the structure, i.e., the response is directly proportional to the input force and the proportionality can be described by a constant stiffness. This assumption is usually violated when large deformations are present. For this reason the excitation of the structure must remain in the linear elastic range of the materials.

An extensive description of the methods to perform modal analysis and extract the modal parameters can be found in [57, 58].

2.4.2. Numerical modal analysis

The equation to be solved in a numerical modal analysis reads:

$$[M]\{\ddot{r}\} + [K]\{r\} = 0, \tag{2.29}$$

where $[M]$ and $[K]$ are the mass and stiffness matrices, respectively of dimension $N \times N$ with N being the number of DOFs. $\{\ddot{r}\}$ is the second time-derivative of the displacement $\{r\}$ with both being vectors of size N. The equation is derived from the general equation of motion (Eq. (2.32)). Thereby, external forces are neglected, since the free vibration problem is being modeled. To simplify the solution, damping is not accounted for in the

equation. This simplification is valid, as the solution is nearly independent of damping for low damping ratios typically found in practical problems [59]. As mentioned before, linearity is assumed, i.e., $[M]$ and $[K]$ have constant values.

A harmonic solution $\{r\} = \{\phi_i\}cos(\omega_i t)$ is assumed to solve Eq. (2.29) where $\{\phi_i\}$ is the eigenvector and ω_i the eigenfrequency of mode i. After substitution it follows:

$$\big[[K] - \lambda_i[M]\big]\{\phi_i\} = 0, \tag{2.30}$$

where $\lambda_i = \omega_i^2$ is the eigenvalue. The solution is obtained by solving the eigenvalue problem:

$$det\left([K] - \lambda_i[M]\right) = 0. \tag{2.31}$$

The natural frequencies are defined by $f_i = \omega_i/2\pi$. The mode shapes are extracted from the eigenvectors in Eq. (2.30) which are normalized by $\{\phi_i\}^T[M]\{\phi_i\} = 1$.

The mass and stiffness matrices are obtained after discretization of the structural model via the FE method. The eigenvalue problem is solved using the state-of-the-art Block-Lanczos algorithm in combination with the sparse direct solver [60]. The numerical solution depends, as usual, on the grid. Elements of second-order accuracy are required and grid dependence tests are recommended to determine the resolution.

2.5. Dynamic FE analysis

In order to predict the deformations and to derive the internal forces and stresses of a structure subjected to time varying loads, a dynamic analysis is performed. Unlike a static analysis, inertial and damping forces are included. For this purpose, the general equation of motion is considered:

$$[M]\{\ddot{r}(t)\} + [C]\{\dot{r}(t)\} + [K]\{r(t))\} = \{F(t)\}, \tag{2.32}$$

where the time-dependent quantities $\{\ddot{r}(t)\}, \{\dot{r}(t)\}, \{r(t))\}$ are the nodal vectors of acceleration, velocity and displacement, respectively. $\{F(t)\}$ is the time-dependent load vector defined by the boundary conditions. $[C]$ is the damping matrix which arises from the assumption of viscous damping, i.e., the damping force is proportional to the velocity.

A simple approach to estimate $[C]$ is called Rayleigh damping. Thereby, the damping is given by a linear combination of the mass and stiffness matrices as:

$$[C] = R_M[M] + R_K[K], \tag{2.33}$$

where R_M and R_K are the mass and stiffness Rayleigh coefficients. A relationship between a frequency-dependent damping ratio $\xi(f)$ and the Rayleigh coefficients can be derived [59] yielding:

$$\xi(f) = \frac{R_M}{4\pi f} + R_K \pi f. \tag{2.34}$$

This relationship can be used to estimate the Rayleigh parameters by interpolating damping ratios obtained experimentally.

The finite-element semi-discrete equation of motion (Eq. (2.32)) is solved by direct time integration methods. The methods available for this purpose are described in [59]. Second-order accurate methods are recommended [60] with a time step size fine enough to resolve the input loads and expected maximal response frequencies.

3. Methodology for modeling dynamic wind loads

Before explaining the strategy followed in the present work to study dynamic wind loads on heliostats, a brief description of the problem is given in this chapter together with some conventions related to the object of investigation and boundary conditions used throughout the thesis.

3.1. Description of the problem

The heliostat field displayed in Fig. 3.1 corresponds to a virtual solar tower power plant with a thermal power of 150 MW. The heliostat field consists of approx. 35×10^3 units distributed over a radius of approx. 500 m. Each heliostat has a mirror surface area of $8\,\mathrm{m}^2$. The methodology developed in the present investigation to predict dynamic wind loads, is applied to a heliostat unit located at the edge of the field as displayed in Fig. 3.1(a). Such heliostats are of especial interest for design purpose, since they are exposed directly to the ABL, and thus to the highest wind speeds. For this reason, they are expected to withstand the largest wind loads. For the selected case, an isolated heliostat unit is considered where the inflow boundary conditions are fully described by the ABL. Although the wind direction changes over time (as will be shown in Sect. 4.3), the angle of attack in the horizontal plane is not varied in the present model due to the

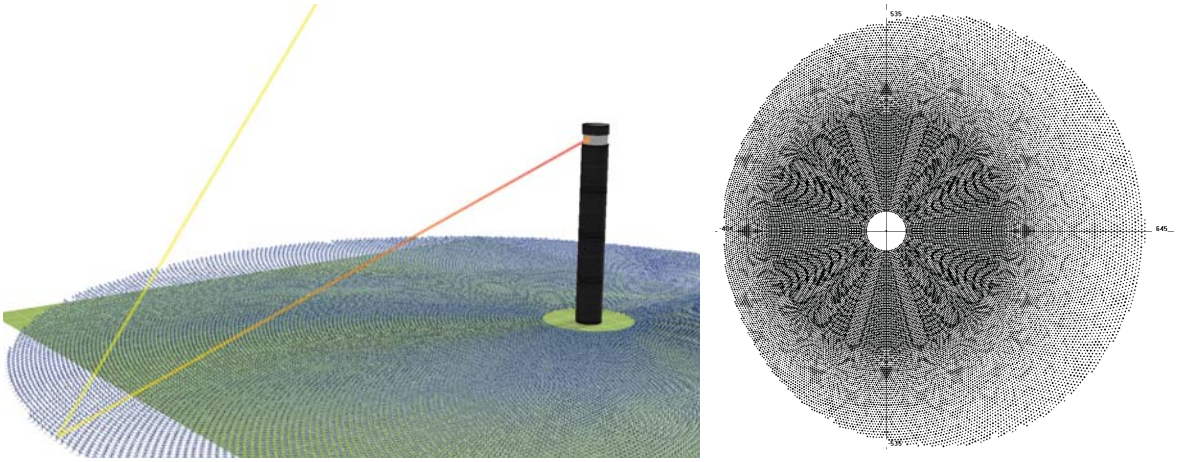

(a) Rays on edge heliostat

(b) Top view of heliostat field

Figure 3.1.: Solar tower power plant.

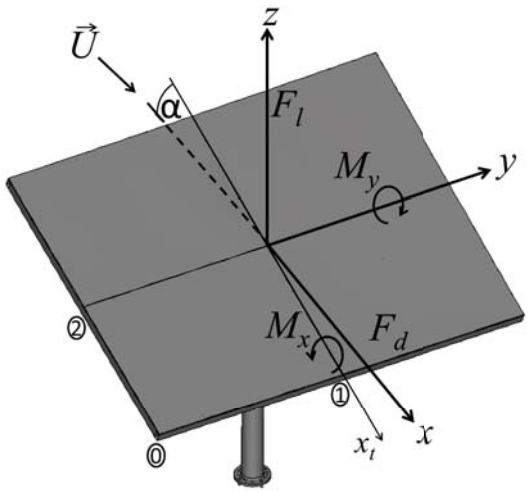

Figure 3.2.: Global coordinate system and main load components.

considerable computational costs associated with it. Hence, the wind direction is along the longitudinal axis x. However, the elevation angle α, defined as the rotation about the lateral axis y, is changed during the analysis to investigate effects of self-induced dynamic loads. During operation, a wide range of elevation angles are found in the heliostats located at the edge of the field, with values of α between 13° and 77°. During night and under strong wind conditions, the heliostats are driven to the horizontal position to protect the mirrors from damage by keeping the loads at a low level. As will be shown in Sect. 5.4.4, critical operating conditions can arise at low elevation angles under high wind speeds. Thus, this investigation focuses on low elevation angles and high wind speeds.

Figure 3.2 shows the coordinate system that defines velocity and load components. The direction of the lift force F_l and the drag force F_d is defined by the vertical axis z and longitudinal axis x, respectively. The moment about the y-axis is denoted by M_y while M_x is the moment about the tangential axis along the plate center x_t. On the lower left facet three positions marked by the numbers 0, 1 and 2 are used later for the analysis of the dynamic results.

3.2. System components

The problem of predicting dynamic wind loads and the associated response of a heliostat structure can be represented by a system where the input data are received from the wind conditions and the output provides information about the loads and deformations of the structure. Between input and output, different areas of analysis are implicated in the problem which are connected in a certain way with each other. In the present work, the system is subdivided in different fields of analysis that are treated separately. Figure 3.3 shows a graphical representation of the individual components of the system.

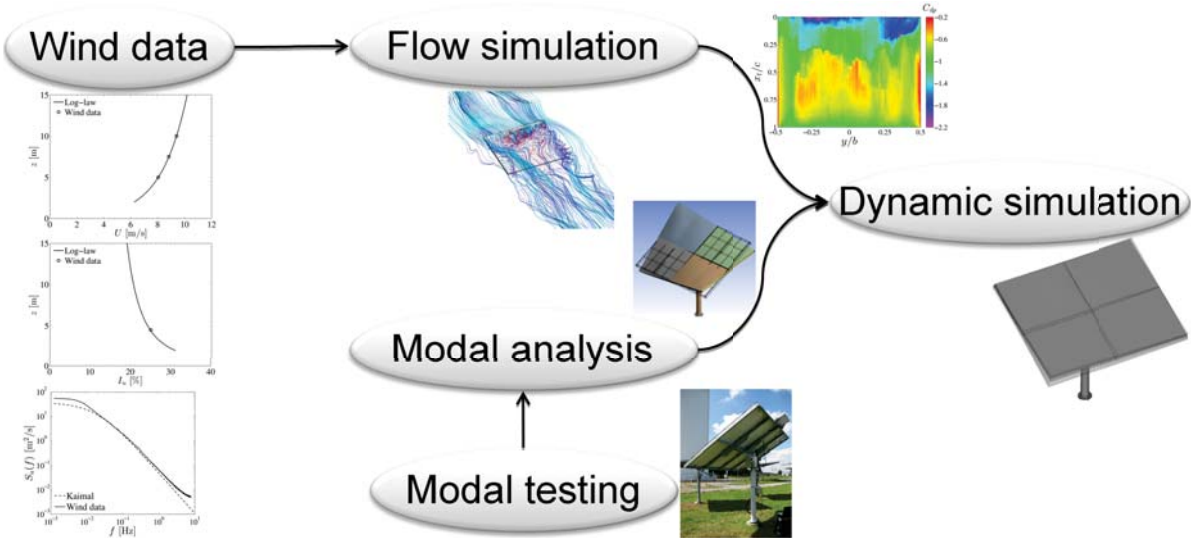

Figure 3.3.: Modeling strategy.

The subsystem **wind data** uses wind data analysis and information from the literature to describe the wind conditions and provide the necessary information to define the boundary conditions in a CFD model. **Flow simulations** are performed to compute the time-dependent wind loads acting on the heliostat. The results from the **flow simulations**, given by transient pressure loads, are used in a FE model to predict the deformations of the structure over time via **dynamic simulations**. The FE model is developed from **modal analysis** that determines the dynamic properties of the structure independently from the loads. The FE model is validated by modal tests that also provide information about the structural damping required for the dynamic model.

In the methodology described above, the information between **flow simulations** and **dynamic simulations** goes in one direction only. This is known as one-way-coupling and is used to reduce the computational effort. The flow simulations are performed on a rigid body and interactions of the deformations with the flow field are not accounted for. This implies that aerodynamic instabilities, e.g., galloping and flutter, can not be reproduced. For this reason, this simplification can only be justified if the deformations are small compared to the dimensions of the structure and the aerodynamic damping is insignificant. The results from [5] and [8] (see Sect. 1.1) suggest that under realistic operating conditions effects of aerodynamic damping and instabilities can be neglected.

Even though the problem described above is based on a particular heliostat under specific boundary conditions, the same modeling strategy can be applied to investigate other heliostat types under different boundary conditions, provided that the same assumptions hold. However, in order to examine heliostat units inside the field the boundary conditions must be modified, since the effects of self-induced turbulence in the wake of upstream heliostats are expected to dominate over the atmospheric turbulence. For this purpose, a CFD model of a slice of the heliostat field with streamwise periodicity can be used. This second type of configuration was not investigated in the present study.

4. Wind data analysis

In this chapter, wind measurements performed by the DLR Institute of Solar Research are analyzed. The objective is to characterize the wind conditions on a typical solar site and evaluate commonly used formulas found in the literature to estimate the main statistical quantities of wind. The analysis provides the input to define boundary conditions in CFD simulations presented in Chap. 6 and gives valuable information for the prediction of the dynamic response under real operating conditions proposed in Chap. 8.

4.1. Experimental setup

Wind measurements took place at the Plataforma Solar de Almeria (PSA) in Spain located at a latitude 37.094° N, longitude +2.359° W and 500 m above sea level. Figure 4.1(a) shows an image of the site. Around the PSA, the terrain is rather flat with low vegetation and can be considered as an open terrain. The location of the measurements is marked by a red pin on the map. The wind mast shown in Fig. 4.1(b) holds different sensors at different heights. An ultrasonic anemometer is attached at 4.5 m above the ground. Three cup-anemometers are located at 5 m, 7.5 m and 10 m. At approx. 10 m above the ground, a wind vane is mounted. In addition, solar radiation is measured simultaneously at the site via pyrheliometers as described in [61].

(a) Aerial view [Map data ©2015 Google, BCNIGN España] (b) Wind mast and sensors.

Figure 4.1.: Plataforma Solar de Almeria and experimental equipment.

4.2. Data sets

The present analysis is based on unpublished data collected during several measurement campaigns [62]. The first data set was recorded in 2009 using a cup anemometer and a wind vane at 10 m above the ground. The data contains the horizontal wind speed and wind direction and was sampled over the entire year with a temporal resolution of 1 minute. A second campaign provided horizontal wind speed data from the cup-anemometers at three different heights (5 m, 7.5 m and 10 m) and was recorded during 2012 with a resolution of 5 s. The third measurement campaign was conducted in 2013-2014 and collected data using the ultrasonic anemometer. It measures the three velocity components at a sampling rate of 20 Hz.

4.3. Data analysis

4.3.1. Wind speed and direction

The horizontal wind speed and direction is analyzed over a year from the data set recorded every minute during 2009. The probability density function of the horizontal wind speed data is shown in Fig. 4.2(a) together with a Weibull distribution that fits very well the measurements with a shape factor of 1.5. The year average is 3.6 m/s while the maximum is found at 25.8 m/s. In Fig. 4.2(b) the distribution is divided into three ranges. Weak and medium wind speeds are defined within the operational conditions of heliostat fields, usually given by the maximal reference wind speed of 10 m/s. They represent, with 98%, the majority of the events. Half of the values are found between 3 m/s and 10 m/s and the other half is mostly below 3 m/s with only 2% above 10 m/s. By analyzing simultaneously wind and solar radiation data, the wind speed samples during operation and actual generation of power can be identified.

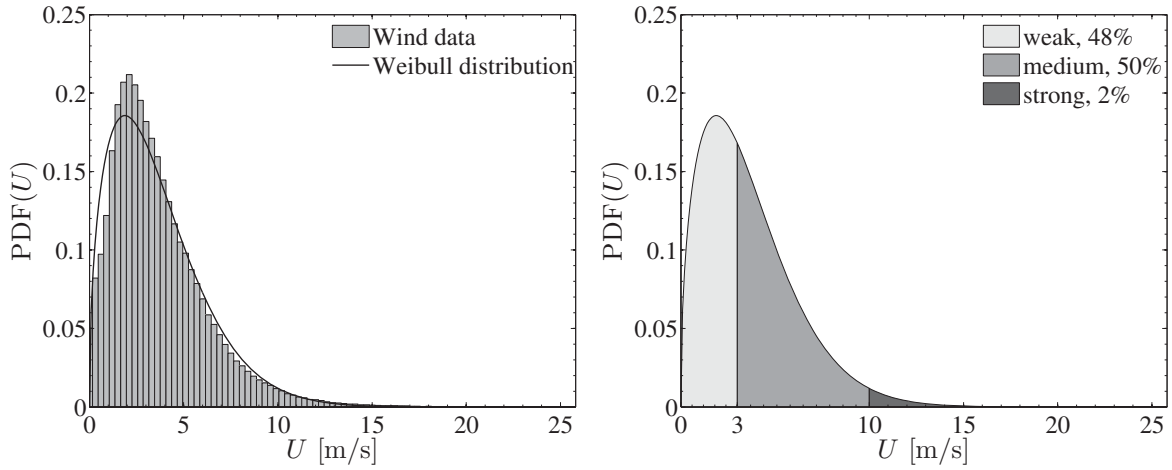

(a) Probability density function

(b) Wind speed ranges

Figure 4.2.: Yearly distribution of wind speed.

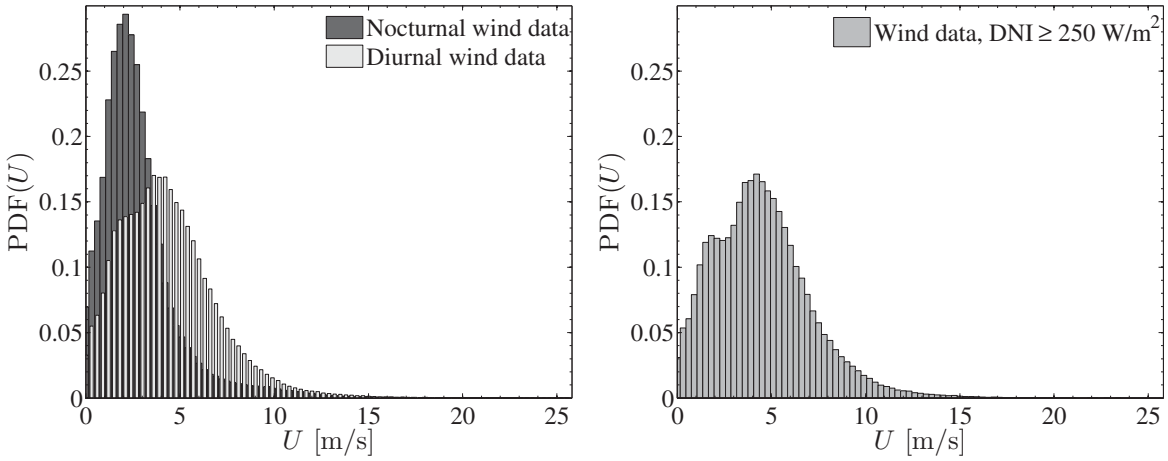

(a) Diurnal and nocturnal distributions (b) Distribution during power generation

Figure 4.3.: Wind speed distributions correlated with irradiance data.

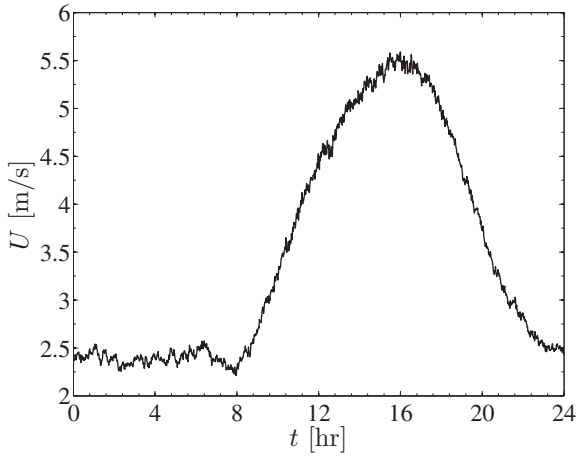

Figure 4.4.: Yearly averaged wind speed over the day.

The period between sunrise and sunset is referred to as diurnal and its counterpart is the nocturnal period. They can be determined from the *global horizontal irradiance* (GHI) which comprises diffuse and direct solar radiation. Within the diurnal period, the heliostats are in operation. However, the period of actual power generation of a CSP plant is limited to clear sky conditions when the solar radiation is above a threshold which depends on the efficiency of the heliostat field. The *direct normal irradiance* (DNI), defined as the radiation received from a small solid angle centered on the sun's disk [63], is used to define this threshold. The reference power plant described in Sect. 3.1 delivers power for DNI $\geq 250\,\mathrm{W/m^2}$. In Fig. 4.3(a) the distribution of the values during day and night is compared. The light gray bars in the foreground represent the diurnal data and exhibit more events toward higher wind speed than the dark bars in the background that represent the nocturnal data and are more concentrated at low speeds. The mean values are found at 4.3 m/s and 2.8 m/s during the day and night, respectively. This difference

is connected to the diurnal variation of the atmospheric pressure which is the mechanical driving force for the wind field and is influenced by free convection during the day as the ground surface is heated up by solar radiation. This can be clearly observed in Fig. 4.4 where the wind speed is plotted along a 24 hour period averaged over the year. Thereby the maximal wind speed values are found during the afternoon at around 16:00. The wind speed distribution during power generation shown in Fig. 4.3(b) is very similar to the diurnal distribution which indicates that clear sky conditions prevail during the day.

The distribution of the wind direction can be observed in Fig. 4.5. The shades of the bars in the wind rose give information about the wind speed ranges described above. The portion of each direction and wind speed range is measured by the length of the bars. It can be observed that about 30% of the values are attributed to east winds ($\pm 20°$) and are predominately in the medium range. Similarly, west and south-west winds are dominated by medium wind speeds. The high wind speed range is found mainly in the north-west to south-west direction, while the majority of the low speed winds are detected in the north-east quadrant. South winds contain also low speeds but are rather seldom.

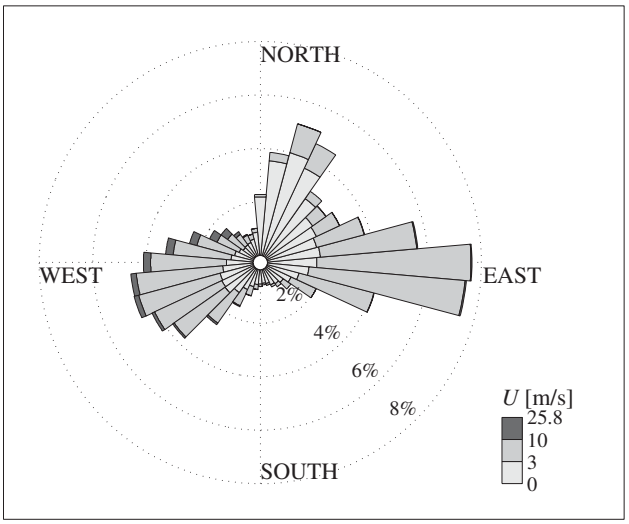

Figure 4.5.: Wind rose over a year.

4.3.2. Wind profile and turbulence

The profile of horizontal wind speed over the height z is displayed in Fig. 4.6. The wind data measured every 5 s at three different heights above the ground were averaged over a complete day with a relatively high wind speed of around 9.5 m/s at $z = 10$ m. The experimental data are compared with the log-law profile given by Eq. (2.5) for two different roughness heights. It can be noticed that the wind data is very well approximated by the profile with a roughness height $z_0 = 8$ cm. The profile computed for $z_0 = 4$ cm shows slightly higher values of U at low heights as can be expected for a smoother terrain where the shear forces are lower.

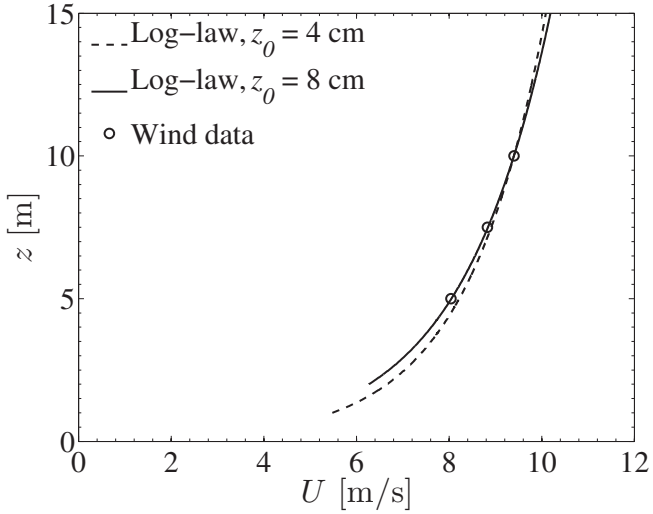

Figure 4.6.: Wind profile.

Turbulence quantities are determined from the measurements of the ultrasonic anemometer located at 4.5 m above the ground. The data recorded at a sampling rate of 20 Hz were analyzed in segments of 10 minutes during a windy week. Only data segments with mean wind speeds above 3 m/s were considered in the analysis, resulting in a total of 43 hrs of data. The turbulence quantities were computed by averaging over a total of 257 data blocks. The 10 min. period is chosen as it contains the scales of turbulence relevant in wind engineering applications (see Sect. 2.2.2).

Theoretical values of the longitudinal and vertical turbulence intensities for different roughness heights computed based on Eq. (2.8) are compared with the wind data in Tab. 4.1. The enhancement of turbulence by increasing the surface roughness is noticeable, especially for the longitudinal component. The turbulence intensities estimated for the larger roughness height are in better agreement with the experimental data.

	z_0 [cm]	I_u [%]	I_w [%]
Theoretical	4	21	11
Theoretical	8	25	12
Wind data		27	12

Table 4.1.: Turbulence intensities for different roughness heights.

Figure 4.7 shows the spectral distributions of the longitudinal and vertical velocity fluctuations from the wind data compared with the model spectra defined by Eq. (2.12) and (2.14) for two different roughness heights. The power spectral densities from the wind data were computed using Welch's method [64] available in Matlab®. The effects of z_0 on turbulence are well reproduced by the model spectra, which show an increase over the entire frequency range as z_0 increases. As observed above, the wind data results are very well approximated by the theoretical values for a roughness height $z_0 = 8$ cm.

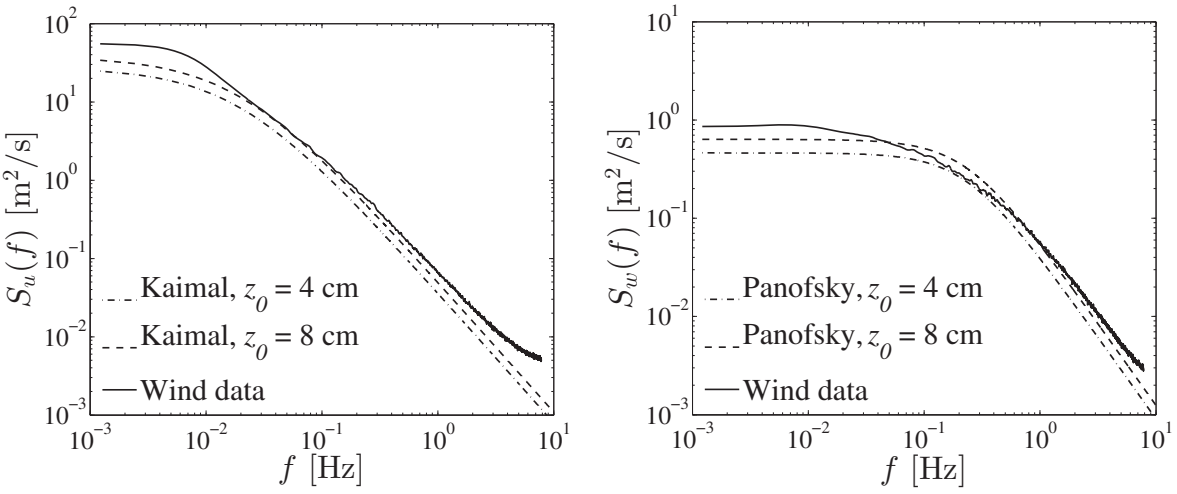

Figure 4.7.: Energy spectra of velocity components averaged over a week.

Turbulence quantities as well as the velocity profile from the wind data presented above correspond approximately to a terrain with a roughness height of 8 cm according to theoretical approximations. Even though $z_0 = 8\,\text{cm}$ can still be considered for an open terrain, the value is rather high as it is usually given between 3 cm and 5 cm [12, 65]. Based on the terrain characteristics of the site described above, a roughness height $z_0 \approx 4\,\text{cm}$ was expected from the analysis. The relatively high turbulence might be caused by nearby heliostats found in the direction of the oncoming flow (see Fig. D.1).

The probability density functions of the vertical and longitudinal velocity components were calculated for a single 10 min. period and the results are compared in Fig. 4.8 with the corresponding normal distributions. It is visible that the resolved velocity fluctuations follow a Gaussian distribution, as mentioned in Sect. 2.2.2.

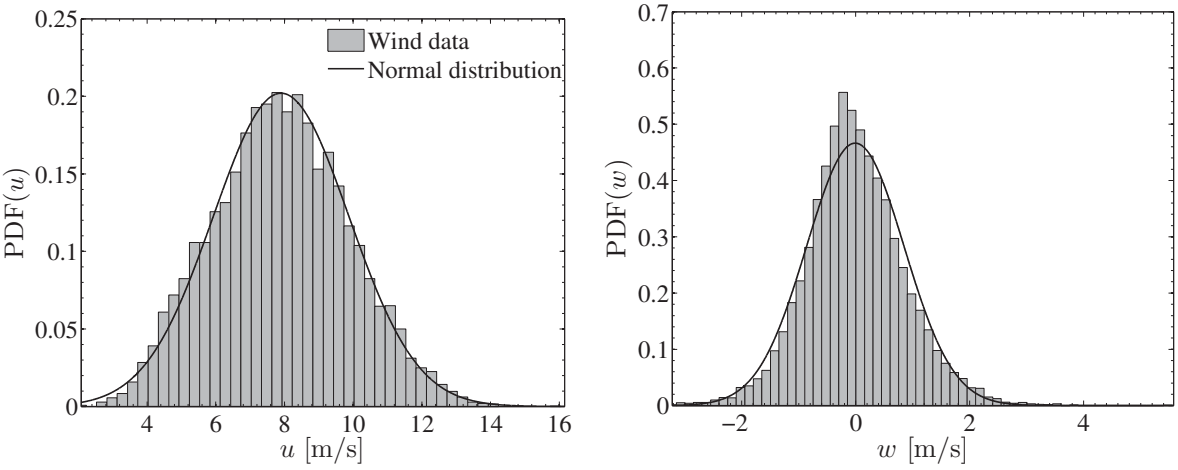

Figure 4.8.: Probability density functions of velocity components.

4.4. Conclusions from wind data analysis

The wind data recorded every minute during a year showed that the heliostats are exposed to wind speeds above 3 m/s for about 50% of the time, while only 2% of the values are expected above 10 m/s. During operation, higher wind speeds are more frequent than at night and the largest values are caused by west winds. Even though large values are seldom, the maximal wind speed found at 25.8 m/s was selected as reference to define boundary conditions in further flow simulations, considering thereby the worst case scenario.

It was demonstrated that theoretical formulas found in the literature represent accurately the main statistical properties of wind including standard deviations, probability densities and spectral distributions. The horizontal wind speed at different heights, as well as the turbulence intensities and spectral densities fit very well to a terrain with a roughness height $z_0 = 8\,\text{cm}$. Since this value is relatively high for an open terrain with the characteristics observed on the site, it is suspected that nearby obstacles such as heliostats are responsible for the high turbulence levels. Due to the limited amount of high resolution data available at the time of the analysis, it was not possible to evaluate signals from other wind directions in order to identify the sources of the high turbulence. Nevertheless, since the model proposed in the present work considers a heliostat unit at the edge of the field exposed to the undisturbed ABL, the roughness height $z_0 = 4\,\text{cm}$ was selected as reference in further CFD models (see Sect. 6.1.1) according to an open terrain.

5. Modal analysis of a heliostat

An experimental and numerical modal analysis was performed on a full-scale heliostat. The objective of the experiments was to obtain information about the dynamic properties of a conventional heliostat structure, i.e., determine its modal parameters. The experimental results were used to validate a numerical FE model by comparing natural frequencies and mode shapes. The purpose of the numerical study was to create a FE model that reproduces the dynamic behavior of the heliostat structure. The validated FE model and the damping coefficients determined experimentally, are used to generate a dynamic FE model to study the response of the structure under fluctuating wind loads. The investigation presented in this chapter has been published by the author in [66].

5.1. Description of test structure

The heliostat structure investigated is shown in Fig. 5.1(a). It consists of a tubular pedestal -or pylon- mounted on a poured-in-place concrete foundation. The azimuth drive is a worm gear attached to the top of the pylon. The elevation drive consists of a linear actuator mounted on a flange fixed to the azimuth drive (see Fig. 5.1(b)). The linear actuator is connected to a second flange attached to the mirror frame. Both flanges are joined by a shaft at the elevation axis located 2.4 m above the ground.

(a) Support structure (b) Drives and mounting

Figure 5.1.: Heliostat structure.

The mirror frame is made of construction steel profiles with rectangular cross-section.The mirror surface is divided into four flat facets attached to the steel frame. The size of the mirror frame is $3.2 \times 2.5\,\mathrm{m}$. The heliostat is located at the solar tower in Jülich, Germany.

5.2. Experimental methodology

Modal tests were carried out only on the mirror frame of the heliostat. One reason to restrict the experiments to this part of the structure is that dynamic wind loads, which are introduced by pressure fluctuations on the mirror surface, are supported in the first place by the frame. Due to its dimensions and central support it offers a large lever arm, and is therefore more susceptible to external excitations on the structure. Moreover, preliminary numerical analysis showed that the dominant modes take place in the frame.

In order to increase data consistency in the analysis, a multi-reference modal test was performed. Thereby, the FRFs were determined via single-input-multiple-output (SIMO) using an impact hammer on different locations and 9 accelerometers. The experimental equipment is shown in Fig. 5.2. The instrumented impact hammer holds a force transducer with a sensitivity of $1.14\,\mathrm{mV/N}$ and a head mass of 140 grams. A soft tip was used to provide sufficient energy at low frequencies. The accelerometers were selected based on their frequency response and sensitivity considering potential disturbances during experiments caused mainly by wind. The sensors have a sensitivity of $500\,\mathrm{mV/g}$. The relative deviations in the amplitude and phase are less than 4% and 1%, respectively for frequencies above 3 Hz. The sensors were attached directly to the frame using wax. The signals were recorded by a 12 channel Front-end connected via Ethernet to a Laptop running PULSE LabShop™ by Brüel & Kjaer [67].

(a) Impact hammer and front-end (b) Accelerometers

Figure 5.2.: Measurement system.

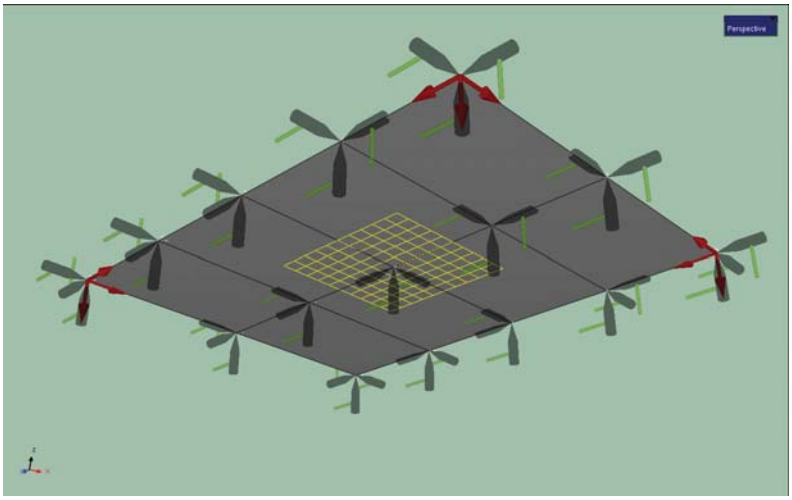

Figure 5.3.: Locations of sensors (red arrows) and impacts.

Three operating points were analyzed with elevation angles of $0°, 30°$ and $60°$. In order to define the locations of the sensors, preliminary numerical simulations were performed to provide information about the mode shapes. With the objective to resolve the most dominant modes, three different corners of the frame were selected where large displacements were predicted in different directions. At each corner three accelerometers were mounted in orthogonal directions indicated in Fig. 5.3 by red arrows. Each beam of the frame was represented as a rigid element in the modal model. Three orthogonal DOFs were defined at each intersection of the beams, resulting in 3×15 DOFs. All 45 DOFs were excited by the impact hammer as illustrated in Fig. 5.3 by the semi-transparent black hammer heads. Each impact measurement was averaged over 5 repetitions in order to remove spurious random noise from the signals caused by ambient conditions and electrical noise in the instrumentation. The averaging procedure also improves statistical reliability in the analysis, as the position and orientation of a single impact can eventually be inaccurate. Tests were executed at the heliostat field under very low wind wind speeds (estimated below 1 m/s), and the signal to noise ratio was measured above 26 dB.

The data analysis was performed using the software Pulse Reflex™ by Brüel & Kjaer [68]. A uniform window weighting function and an exponential window were applied to the input and output signals respectively to correct for *leakage* in the Fourier analysis, a problem which is a direct consequence of the need to take only a finite length of time history coupled with the assumption of periodicity [58]. Leakage shows up by the measured peaks being too broad and too low [69], as if energy was "leaked" from the resonant peaks to contiguous frequencies. The frequency span in the analysis was up to 50 Hz and each measurement had a duration of 8 s giving a frequency resolution of 125 mHz. Modal parameter estimation was accomplished by the RFP-Z method [58], which is a multi-degree of freedom (MDOF) method that operates in the frequency domain and analyzes multiple FRFs simultaneously. It is well-suitable for structures with closely-coupled modes and moderate damping [68].

5.3. Numerical methodology

The model was created and solved using ANSYS Mechanical R15.0 [60]. The FE model of the heliostat is shown in Fig. 5.4. The model consists of around 100 parts representing the main components of the structure. A fixed support is set at the bottom of the pylon as boundary condition. Simplifications were necessary in order to reduce the complexity and size of the model. Parts such as screws, bolts and gears were replaced by joint elements with corresponding degrees of freedom. The joint elements are indicated by their local coordinate axes in Fig. 5.5(b). The control unit and the gears of the azimuth drive were not explicitly modeled. Their inertial mass was represented by virtual mass points. The torsional stiffness in the joint element representing the azimuth drive was estimated based on data of a similar gear drive [70]. Backlash in the drives is neglected in the model since it violates the assumption of linearity required in the modal analysis, which implies a direct proportionality between input force and displacement. This simplification is less critical at the elevation drive, as it is pretensioned by gravity forces. However, it might have an effect on vibrations associated with the azimuth drive. Material properties were taken from the heliostat investigated experimentally, which is made from construction steel mainly.

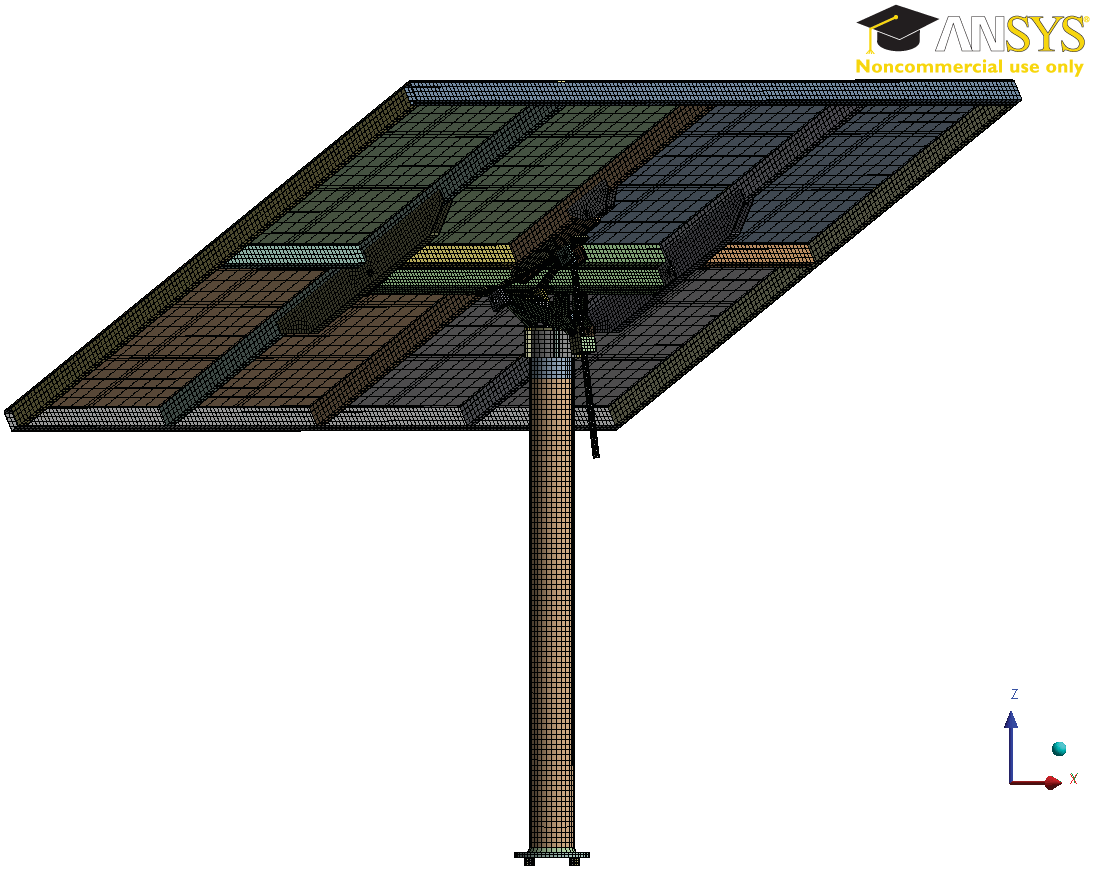

Figure 5.4.: FE model of the heliostat.

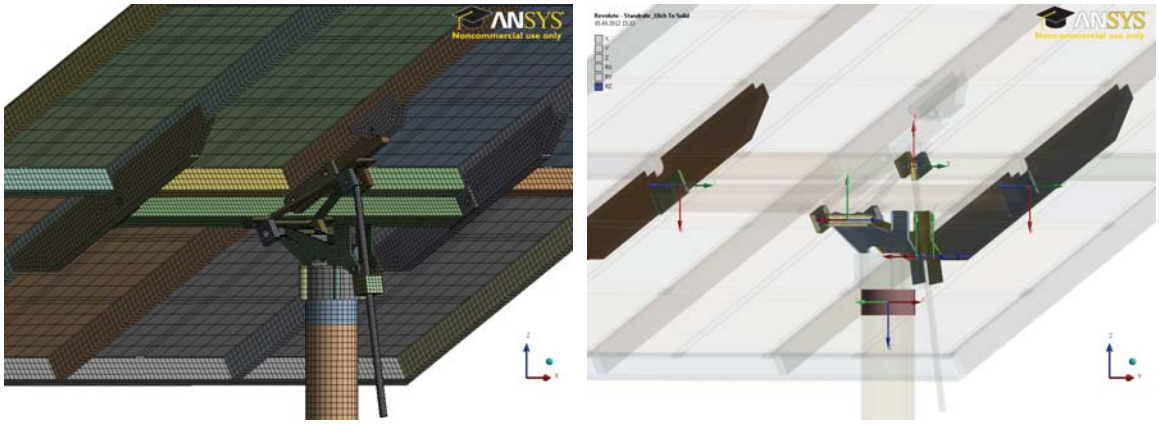

(a) Support structure (b) Joint elements

Figure 5.5.: Detailed view of FE model.

The block Lanczos algorithm [71] was selected to solve the eigenvalue problem. The frequency range to obtain the modes was limited to 50 Hz, since the dominant modes are expected withing this range as well as the majority of the excitation energy due to wind loads as will be shown later in Sect. 5.4.4 and 6.2.3. The first seven modes were selected and their mode shapes were extracted for further analysis as they involve more than 90% of the inertial mass of the structure. This is determined by the participation factors which are a by-product of the numerical simulations and give the contribution of each mode to the dynamic response in a specific direction.

The mesh consists of second-order hexahedral elements with middle nodes. Grid convergence was examined by evaluating the natural frequencies of the first seven modes for three different grid resolutions. Table 5.1 shows a comparison of the natural frequencies. Due to the small differences compared to the finest grid, the medium grid resolution was considered to be sufficient for further simulations.

		Mode						
Case	Num. nodes	1	2	3	4	5	6	7
Coarse	1.0×10^5	4.3	4.5	4.8	7.4	10.0	12.6	18.5
Medium	2.4×10^5	4.3	4.5	4.7	7.2	9.8	12.0	18.4
Fine	4.7×10^5	4.3	4.5	4.7	7.3	9.8	11.9	18.4

Table 5.1.: Natural frequencies [Hz] for different grid resolutions at $\alpha = 30°$.

5.4. Results and discussion

5.4.1. Mode shapes

A qualitative comparison between modal tests and numerical simulations is presented in the following figures. The first 6 mode shapes of one operating point are shown in Fig. 5.6. Similar results were obtained for the other two operating points investigated. The mode shapes are indicated by an augmented deformation of the structure (full surfaces) relative to the non-deformed state (black edge lines). The first mode is a rigid-body motion of the mirror frame described by an in-plane oscillation about the azimuth axis. The modes 2 and 3 are also rigid-body motions of the structure. The second mode indicates an oscillation about the shortest middle axis of the rectangular mirror frame, while the third mode oscillates about the longest middle axis. Modes 4 and 5 are similar to 3 and 2, respectively, with a superposition of a translation of the center caused by the bending vibration of the pylon. The sixth mode shape is a torsional mode, where corners on the same edge of the frame oscillate out-of-phase.

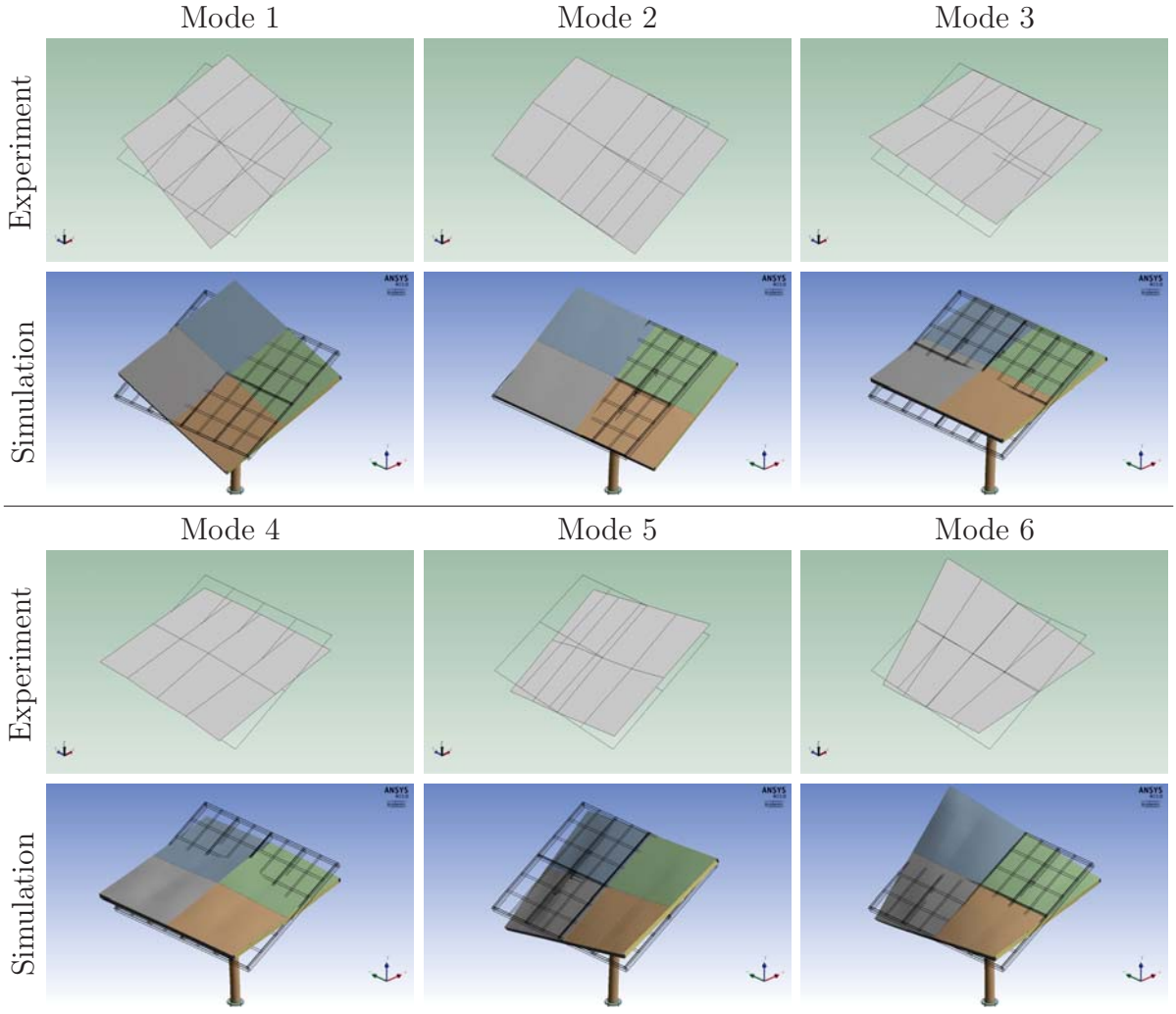

Figure 5.6.: Comparison of mode shapes at 30° elevation angle.

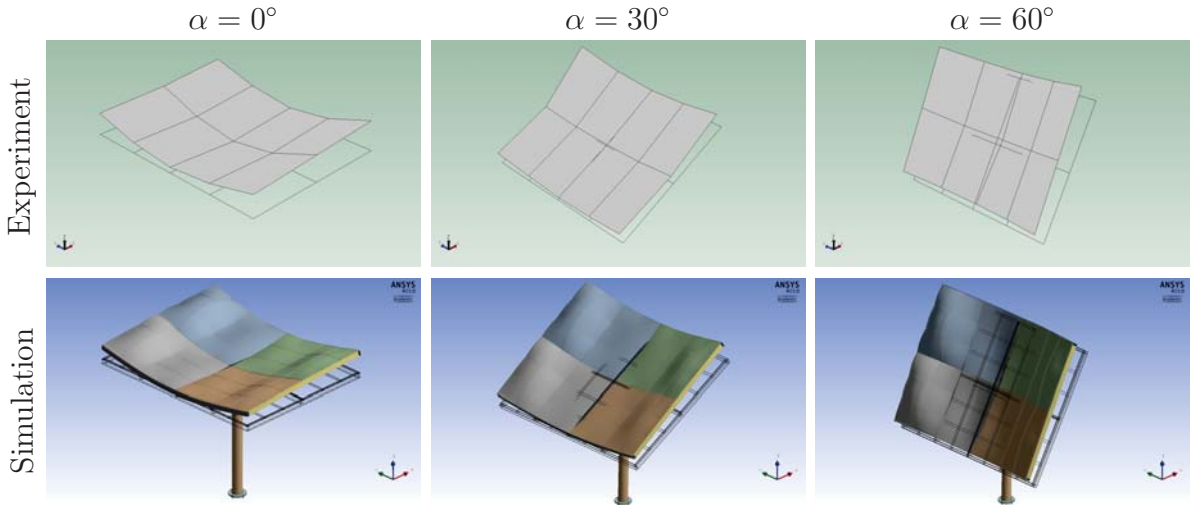

Figure 5.7.: Comparison of mode 7 at different elevation angles.

Figure 5.7 describes mode 7; a bending mode about the shortest middle axis of the mirror frame. It can be noticed that the mode shapes do not change with variation of the elevation angle. Except for the first mode, all mode shapes are out-of-plane motions which could possibly be excited by fluctuating wind loads, since pressure fluctuations act in the surface-normal direction. The good agreement between simulations and experiments holds for all mode shapes and operating points investigated (see Fig. C.1).

5.4.2. Natural frequencies

The natural frequencies of all operating points investigated are compared in Tab. 5.2. The frequencies are between 3.2 Hz and 21.2 Hz. The modes potentially affected by fluctuating wind loads (i.e., out-of-plane modes) are above 3.8 Hz. Only modes 4 and 7 show a minor dependency of the frequencies on the elevation angle. When increasing the elevation angle, the natural frequencies in the fourth mode decrease slightly while in the seventh mode they increase. This dependency is found in the experiments as well as in the simulations. The natural frequencies from the simulations are in general higher than the experimental results. This might be caused by an increased stiffness in the contact region between several parts of the support structure, which results from omitting rivets, screws and bolts and assuming that the adjacent surfaces are bonded. The largest discrepancies which are found in the first mode might also be associated with simplifications of the azimuth drive mentioned above.

5.4.3. Damping ratios

The values presented in Tab. 5.3 represent the level of damping relative to the critical damping, which is the threshold between oscillatory and non-oscillatory behavior. It is determined by the half power (-3 dB) points of the magnitude of the FRF at the resonance frequencies. Its prediction depends strongly on the frequency resolution and

		Mode						
	$\alpha[^\circ]$	1	2	3	4	5	6	7
Exp.	0	3.3	3.8	4.0	6.8	8.0	10.7	15.0
Sim.	0	4.3	4.5	4.6	7.7	10.1	11.9	17.2
Exp.	30	3.2	3.8	3.9	6.2	8.3	10.7	15.9
Sim.	30	4.3	4.5	4.7	7.2	9.8	12.0	18.4
Exp.	60	3.2	3.8	4.1	5.9	8.1	10.7	18.0
Sim.	60	4.3	4.7	4.8	6.8	9.3	12.1	21.2

Table 5.2.: Comparison of natural frequencies [Hz] between experiment and simulation.

	Mode						
$\alpha[^\circ]$	1	2	3	4	5	6	7
0	1.6	1.9	1.7	1.6	1.3	0.7	1.1
30	1.7	2.2	1.6	1.7	1.2	0.7	1.5
60	1.6	2.6	1.7	1.8	1.3	0.7	0.9

Table 5.3.: Damping ratios rel. to the critical values [%] determined experimentally.

the accuracy was estimated at ±0.5%. The results are in the range between 0.7% and 2.6% and correspond to a relatively light damped structure. The damping ratios do not exhibit a significant dependency on the elevation angle; the differences between the values are within the accuracy of this quantity.

5.4.4. Critical conditions

Vortex-induced vibrations occur when vortices are shed alternately from opposite sides of the structure. This gives rise to a fluctuating load perpendicular to the wind direction. Large vibrations may occur if the dominating frequency of vortex shedding f_s is the same as a natural frequency f_n for the structure vibrating in a mode in the cross-wind direction [16]. Vortex shedding frequencies can be determined from experimental data using the Strouhal number St:

$$f_s = \frac{St \cdot U}{L}, \tag{5.1}$$

where L is a characteristic length[1] and U a reference velocity. This simple approach applies to a unit located at the edge of the heliostat field that is exposed directly to the atmospheric wind in an open country terrain. Figure 5.8 shows the vortex shedding frequency vs. wind speed at different elevation angles. The curves were calculated from Strouhal numbers of inclined flat plates found in [72, 73] using a characteristic length of

[1]The projected height $c \cdot \sin(\alpha)$ is commonly used as characteristic length in the definition of St, giving an approximately constant value for flat plates and rectangular cylinders for $\alpha > 30^\circ$ [31, 72, 73]. However, since the present work will be focused on $\alpha < 30^\circ$, the definition $L = c$, which is also found in the literature used here [72, 74, 75], is preferred.

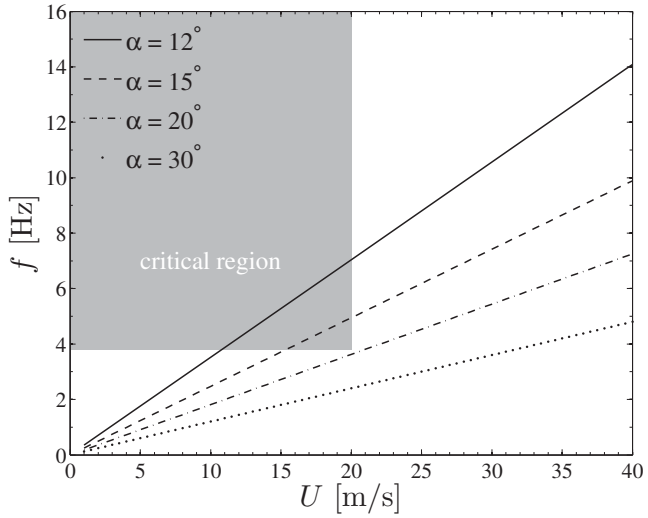

Figure 5.8.: Vortex shedding frequency of an inclined flat plate.

2.5 m according to the mirror frame dimensions. When the elevation angle decreases, the frequency increases for a given velocity and it can be expected that elevation angles below the values found in the literature are well within the gray area for velocities below 10 m/s. The gray area in the graph indicates potentially critical operating conditions where vortex shedding frequencies are in the range of the natural frequencies of the heliostat structure. The frequency range contains the natural frequencies from the out-of-plane modes mentioned above that are at risk to be excited by pressure fluctuations. The wind speed range was specified from the maximal wind speed expected at the elevation axis. The data was obtained from wind data presented in Sect. 4.3.1. It should be mentioned that higher wind speeds are possible and depend strongly on the conditions of the site considered. Furthermore, this simple approach does not account for free stream turbulence effects or tip vortices present under real conditions, which can be relevant for the dynamic wind loads and are investigated in detail in Chap. 6.

5.5. Conclusions from modal analysis

The present study served as a validation for a FE model of a conventional heliostat design. The mode shapes predicted by the model are in very good agreement with the experimental results in all operating points investigated. Mode shapes with a potential risk to be excited by fluctuating wind loads were identified above 3.8 Hz. The discrepancies in the natural frequencies between simulations and experiments are acceptable, taking into account the large number of parts and the complexity of the structure. Potentially critical conditions were found at elevation angles $< 20°$ using a simple approach. The FE model developed in the present study in combination with the damping coefficients determined experimentally will serve as the basis for a dynamic model to analyze the response of the structure under fluctuating wind loads.

6. Simulation of the flow over a heliostat

A CFD study with the objective to predict time-dependent wind loads on a heliostat is presented in this chapter. First, the numerical model is described in Sect. 6.1. After that, preliminary simulations required to ensure the quality and validity of the results are presented in Sect. 6.2.1 and 6.2.2. Before discussing final results in Sect. 6.3, the generation of realistic inflow boundary conditions is presented in Sect. 6.2.3. Finally, the conclusions from this study are summarized in Sect. 6.4.

6.1. Numerical methodology

6.1.1. Geometry and boundary conditions

The numerical model described here corresponds to a heliostat located at the edge of a heliostat field as shown in Fig. 3.1. The geometry displayed in Fig. 6.1 consists of an inclined flat plate with an elevation angle α varied at 5°, 10° and 20°. It is a simplified representation of the mirror frame of the heliostat structure presented in Chap. 5. The plate has a side length $c = 2.5\,\mathrm{m}$, a width $b = 3.22\,\mathrm{m}$ and a thickness $s = 0.09\,\mathrm{m}$. The plate center is located at a height above the ground $h = 2.4\,\mathrm{m}$ and a distance of $1.5 \times b$ from the lateral planes. The distance between the leading edge and the inflow plane is $2 \times c$ and between the trailing edge and the outflow plane is $3 \times c$. The dimensions of the surrounding domain are $6.25 \times h$ in vertical direction, $3 \times b$ in lateral direction and approximately $6 \times c$ in streamwise direction.

The inlet boundary is located at $x/c = 0$ and mimics the atmospheric boundary layer of an open country terrain. A mean velocity profile is prescribed using the log-law (Eq. (2.5)) with a roughness height $z_0 = 4\,\mathrm{cm}$ [18] and a reference velocity of $25.8\,\mathrm{m/s}$ at $z = 10\,\mathrm{m}$ corresponding to the maximal value found in the wind data analysis (see Sect. 4.3.1). This profile leads to a mean velocity of $U_\infty = 20\,\mathrm{m/s}$ at the height of the leading edge. Assuming that the flow is independent of the Reynolds number as discussed in Sect. 2.1.4, the computational effort is reduced by setting arbitrarily the dynamic viscosity $\mu = 3.06 \times 10^{-3}\,\mathrm{kg/(s\,m)}$ to obtain $Re = \rho\, U_\infty\, c/\mu = 2.0 \times 10^4$, with the air density $\rho = 1.225\,\mathrm{kg/m^3}$ and the chord length $c = 2.5\,\mathrm{m}$. The validity of this assumption is further examined in Sect. 6.2.2. Atmospheric turbulence is accounted for via the vortex method explained in Sect. 2.3.2. The model parameters of the VM were determined in a preliminary study presented in Sect. 6.2.3. The top ($z/h = 6.25$) and back ($x/c \approx 6$) planes are defined as pressure outlets using the weighting procedure

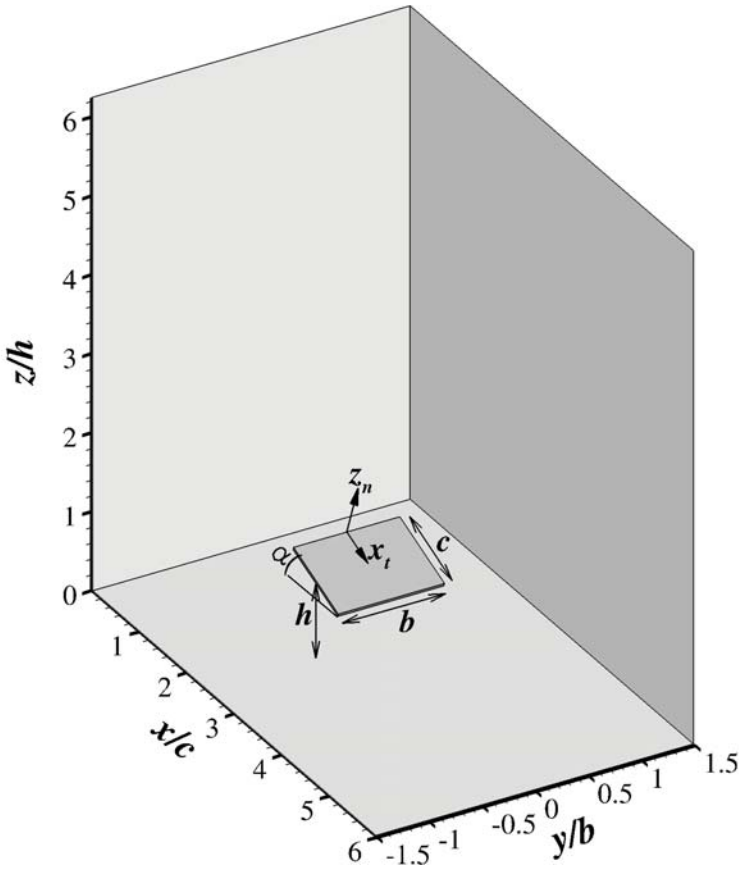

Figure 6.1.: Computational domain.

described in Appendix A.1 to reduce boundary effects. No-slip boundary conditions are applied to the plate and ground surface. Periodic boundaries are defined at the lateral planes ($y/b = \pm 1.5$).

6.1.2. Numerical setup and grid

The finite-volume code Fluent [52] was used to solve the incompressible filtered Navier-Stokes equations by means of Large-Eddy Simulation (LES). Thereby, the WALE model is responsible for the unresolved subgrid-scales. The SIMPLEC algorithm was selected for pressure-velocity coupling in the segregated solver. The convective terms in the momentum equations are approximated by the central differencing scheme (CDS). A second-order implicit time integration is used for temporal discretization and the equations are solved by the fractional step method (FSM), which is a non-iterative time-advancement scheme that significantly speeds up transient simulations by performing only a single outer iteration per time step. A time step $\Delta t = 0.001 \times c/U_\infty$ was selected to satisfy the Courant-Friedrichs-Lewy criterion (Eq. (2.20)) yielding $CFL < 0.7$. The calculations were performed for a total of 180 convective time units $t \cdot U_\infty/c$. However, only the last 120 convective units were considered for computing statistics in time in order to exclude initialization effects (see Fig. B.1).

The computational grid was created in ICEM CFD [76]. Figures 6.2(a)-(d) showcase different views of the grid. It consists of a block-structured grid with cells clustered in the vicinity of the plate. Grid coarsening was accomplished by an exponential law towards the outflow boundaries. A hyperbolic distribution of the grid points was selected for coarsening the mesh towards the inflow plane and the ground surface in order to limit the maximal cell size and to resolve the incoming turbulence. The grid spacing in wall-normal direction around the plate was designed to obtain values of $y^+ \leq 3$ with approximately 15 CVs located in the boundary layer. Unlike the plate, at the ground surface the wall adjacent cells are placed outside the viscous sublayer giving values of y^+ up to 25 (this subject is further discussed in Sect. 6.2.3). For $y^+ > 3$, a three-layer log-law [77] is used. In Appendix A the use of wall functions and the WALE model are evaluated in a benchmark test case [75]. The grid was smoothed by a built-in feature of ICEM CFD [78] that reduces sharp transitions between cell blocks and improves orthogonality at the boundaries. The number of CVs and further information about the grid resolution are given in Sect. 6.2.1.

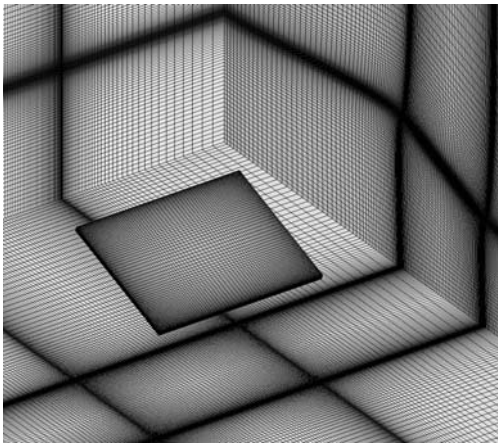

(a) Isometric view around the plate.

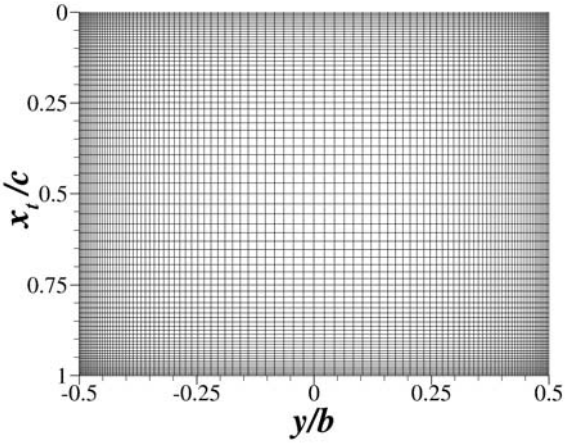

(b) Top view of the plate.

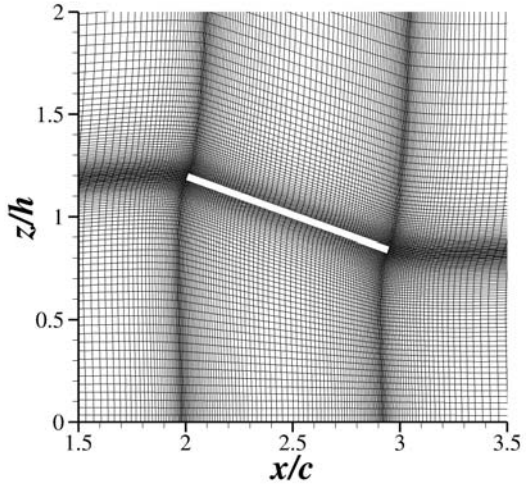

(c) Slice at mid-width position.

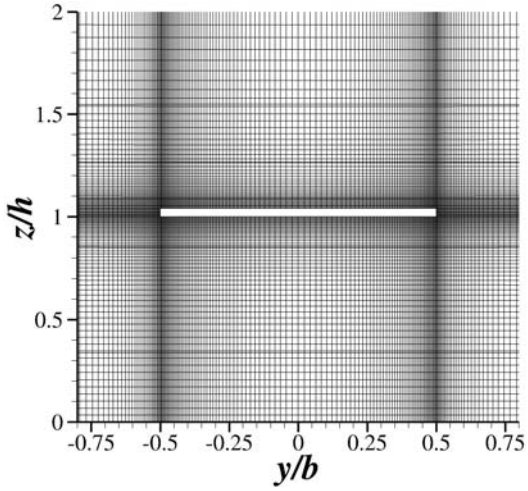

(d) Slice at mid-length position.

Figure 6.2.: Depictions of the grid.

6.2. Preliminary numerical tests

6.2.1. Grid resolution

Grid dependency of the solution was investigated using three different resolutions for the case $\alpha = 20°$. The grid refinement was carried out mainly along the edges of the plate, while the size of the wall adjacent cells in normal direction was kept the same in all cases. The grids are displayed in Fig. 6.3 and detailed information is given in Tab. 6.1.

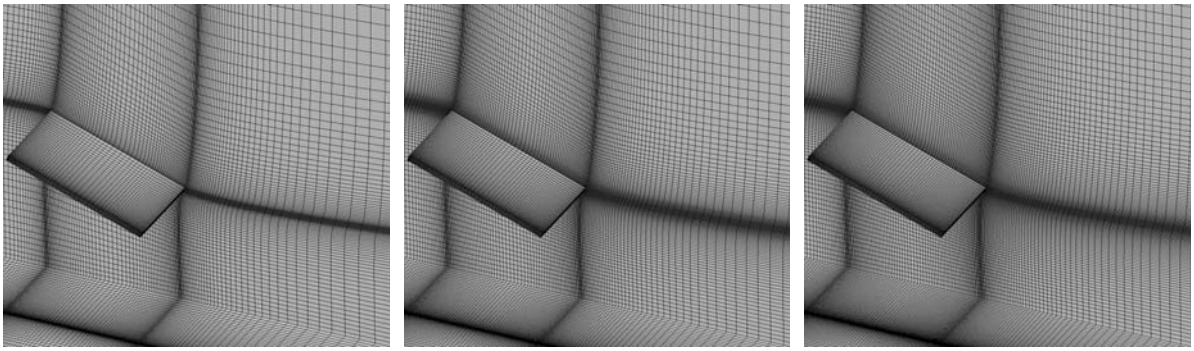

(a) coarse (b) medium (c) fine

Figure 6.3.: Different grid resolutions in the vicinity of the plate.

Case	Total No. of CVs	CVs along plate length	CVs along plate width	Wall-normal spacing	Streching ratio
Coarse	2.6×10^6	66	88	$0.002 \times c$	1.15
Medium	4.6×10^6	76	98	$0.002 \times c$	1.10
Fine	6.6×10^6	86	108	$0.002 \times c$	1.05

Table 6.1.: Grid information.

Time-averaged streamlines at the mid-span plane are displayed in Fig. 6.4 for different grid resolutions. As expected, the flow remains attached on the windward side of the plate, while on the leeward side flow separation takes place at the leading edge forming a clockwise rotating recirculation region. Unlike the flow over infinite plates (see Fig. A.3) and airfoils at high incidence [79], a counter-clockwise rotating trailing-edge vortex is not visible. This is due to the dominating transversally rotating flow induced by the tip vortices. Only at the tail of the separation bubble the coarse grid exhibits some differences compared to the other resolutions, which show streamlines emerging from a point close to the trailing edge whose origin is explained in Sect. 6.3, and entrainment from the wake in the upper region of the bubble. Despite these differences, the time-averaged pressure distribution on the plate is not affected as can be seen in the profiles of the pressure coefficient along two different sections presented in Fig. 6.5. The evaluation of the time-averaged flow field at other planes showed a very good agreement between the grid resolutions as well (see Appendix B.2).

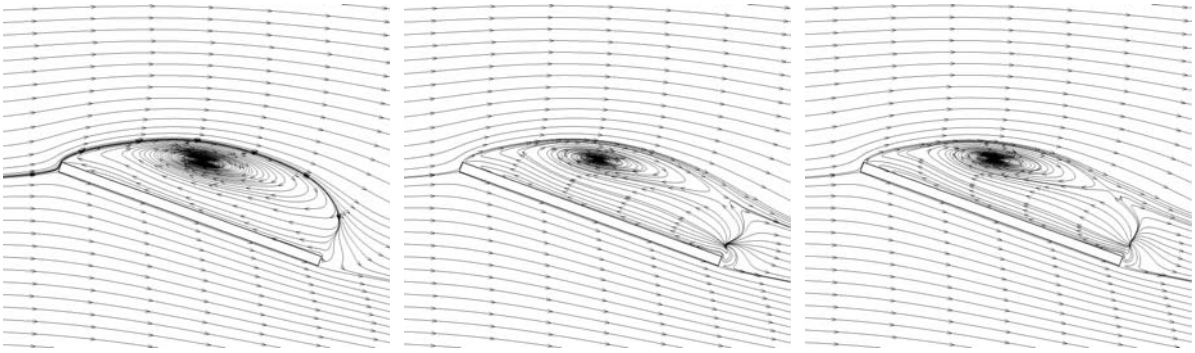

(a) coarse (b) medium (c) fine

Figure 6.4.: Time-averaged streamlines at mid-span plane $y/b = 0$.

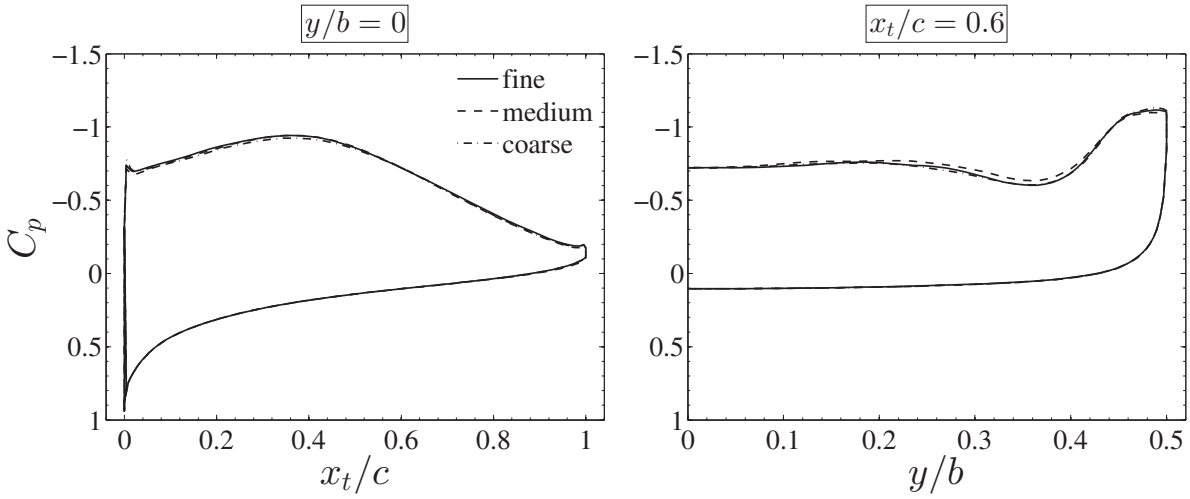

Figure 6.5.: Profiles of the time-averaged pressure coefficient along the mid-span section at $y/b = 0$ and along the lateral section at $x_t/c = 0.6$.

The mean and standard deviations of the lift (C_l), drag (C_d) and moments about the symmetry axes of the plate (C_{my}, C_{mx}[1]) are presented in Tab. 6.2. All coefficients show a very good agreement between the three different resolutions. This behavior holds also for the spectral distribution of the lift coefficient (see Fig. B.5).

Grid	$\overline{C}_l$	$\overline{C}_d$	$\overline{C}_{my}$	σ_{C_l}	σ_{C_d}	$\sigma_{C_{my}}$	$\sigma_{C_{mx}}$
Coarse	0.86	0.37	0.12	0.029	0.010	0.013	0.006
Medium	0.86	0.37	0.11	0.032	0.010	0.014	0.006
Fine	0.86	0.37	0.11	0.030	0.010	0.012	0.006

Table 6.2.: Statistical values of force and moment coefficients for different grid resolutions.

[1]Due to symmetry conditions about the x_t-axis follows $\overline{C}_{mx} = 0$, hence it is omitted in Tab. 6.2.

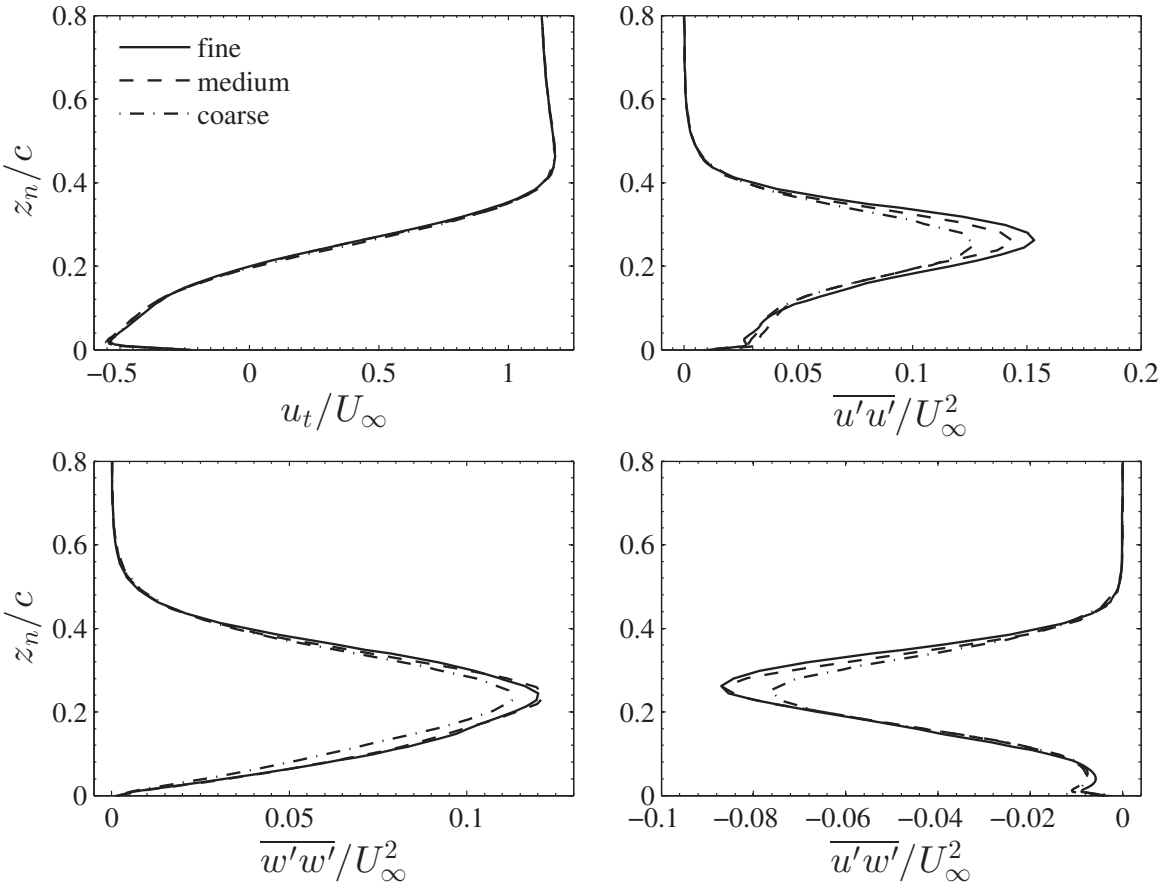

Figure 6.6.: Tangential velocity and Reynolds stresses at $x_t/c = 0.6, y/b = 0$.

The effects of the grid resolution are most notably in the profiles of the Reynolds stresses along a line normal to the plate shown in Fig. 6.6. Thereby, the agreement between the medium and fine grids can be distinguished, especially at the peaks of the Reynolds-stresses located at $z_n/c \approx 0.22$ where the coarse grid exhibits lower values.

The grid dependency of the solution is rather moderate for the grid resolutions examined here. Force coefficients along with the spectral distribution (see Fig. B.5) showed a very good agreement in all cases. Only minor differences could be noticed in the mean flow field and the resolved turbulence structures (see Fig. B.6). More clear indications of grid convergence were observed in the profiles of the Reynolds stresses, where the medium resolution was considered to be sufficient for further simulations.

6.2.2. Reynolds number dependency

Under extreme wind conditions found in Sect. 4.3.1, a Reynolds number $Re = 3.4 \times 10^6$ can be determined for the present study based on the dynamic viscosity of air $\mu = 1.79 \times 10^{-5}\,\mathrm{kg/(s\,m)}$, the air density $\rho = 1.225\,\mathrm{kg/m^3}$, the reference velocity $U_\infty = 20\,\mathrm{m/s}$ and the characteristic length $c = 2.5\,\mathrm{m}$. Such a large Re implies that the turbulent ki-

netic energy (k_t) is distributed over a wide range of turbulent scales present in the flow. For a reliable LES, the majority of this scales need to be resolved (at least 80% of k_t [39]). This leads to a substantial computational effort which increases exponentially with Re [80]. Thus, it is not feasible in the present study to perform simulations under realistic conditions. For this reason, the dynamic viscosity was set arbitrarily to obtain $Re = 2.0 \times 10^4$. This simplification is only valid if Reynolds effects are small for the flow under examination. As discussed in Sect. 2.1.4, it can be expected, at least for the mean loads, that this assumption holds, due to the fact that flow separation takes place at the sharp edges of the inclined flat plate presented here. Still, it is not clear how Re affects fluctuating loads and their spectral distribution, which is of great importance in the present study. To examine this subject, a new case was generated for $Re = 2.0 \times 10^5$, corresponding to an increase in Re by one order of magnitude compared to the base line case presented above. This assessment is still far from realistic conditions, nevertheless, it is suitable to evaluate the Reynolds dependency of the solution.

In order to resolve the majority of the eddies existent at a higher Re, the grid presented above was refined in all directions as shown in Tab. 6.3. The wall-normal distance of the adjacent cells was reduced to preserve $y^+ \leq 3$ and the time step was set to $\Delta t = 0.0004 \times c/U_\infty$ to satisfy the CFL-criterion with values of $CFL < 0.8$. The numerical setup used in this case was the same as described in the previous section, except for the discretization of the convective terms. Using CDS leads to nonphysical wiggles in the solution. For this reason, the bounded central differencing scheme (BCD) was adopted here, which is a blended scheme of CDS and second-order upwind scheme (UDS) and is based on the normalized variable diagram (NVD) approach [81].

Total No. of CVs	CVs along plate length	CVs along plate width	Wall-normal spacing	Stretching ratio
10.7×10^6	114	146	$0.0004 \times c$	1.10

Table 6.3.: Grid information of high Reynolds number case.

Figure 6.7 illustrates instantaneous snapshots of the flow field over the heliostat plate at both Re. The isosurfaces of the λ_2-criterion [82] visualize vortex cores in the separated flow. A distinctive pair of counter-rotating tip vortices can be observed along the lateral edges of the plate. They originate at the upper corners and grow in diameter downstream as the result of the increasing pressure difference between windward and leeward side responsible for the roll up of the vortices. The primary vortex is enclosed by a helical vortex sheet which disappears at some point after the trailing edge. From this position on, the more stable primary vortex core is convected downstream. Furthermore, arching structures are detected above the trailing edge. They arise from leading-edge vortices deformed by the counter-rotating flow induced by the tip vortices. These Ω-shaped vortices dissipate very quickly in the near-wake region. The same flow features can be found in experimental and numerical investigations on rectangular plates and delta wings [83, 84].

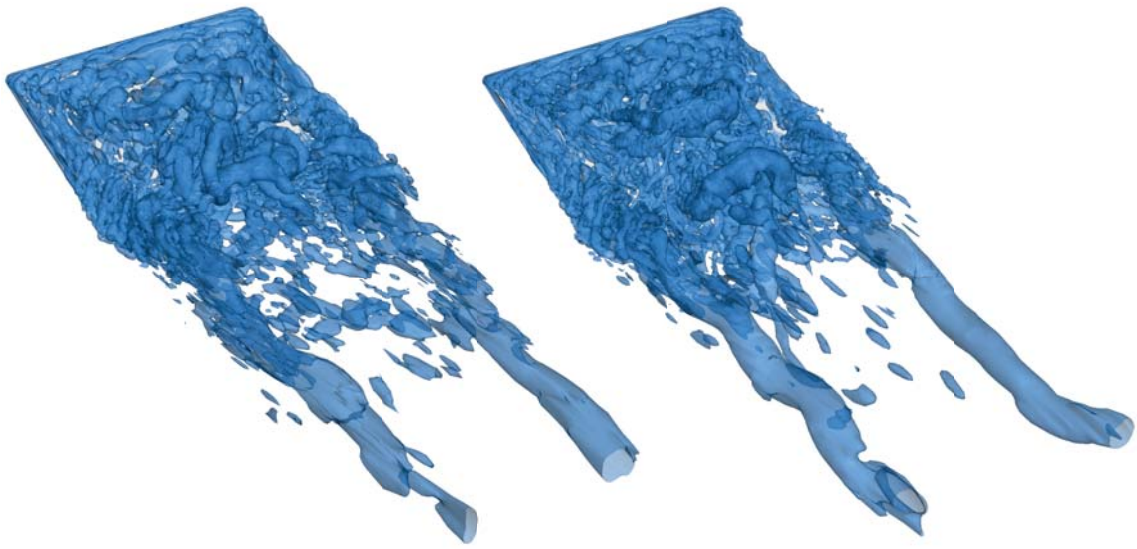

(a) $Re = 2.0 \times 10^4$ (b) $Re = 2.0 \times 10^5$

Figure 6.7.: Isosurfaces of $\lambda_2 = -500$ for different Reynolds numbers.

The overall topology of the instantaneous flow is very similar at both Reynolds numbers considered. Only minor differences can be noticed in the presence of small-scale turbulence structures, being more abundant at higher Re.

The time-averaged pressure coefficient on the leeward side is compared in Fig. 6.8. The presence of the separation bubble and tip vortices is clearly visible in the low pressure regions. The agreement in the pressure distribution is noticeable between both Re. However, at $Re = 2.0 \times 10^5$ the transition between the regions of separated and reattached flow are sharper (i.e. the gradients are more pronounced) and the absolute values towards the upper corners are higher .

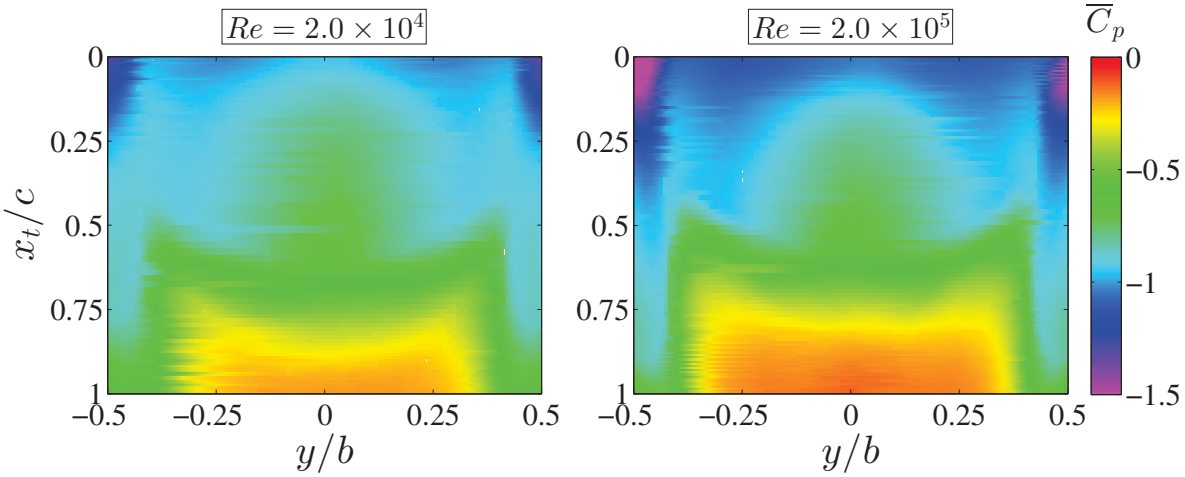

Figure 6.8.: Time-averaged pressure coefficient on the top surface of the plate for different Reynolds numbers.

Re	$\overline{C}_l$	$\overline{C}_d$	$\overline{C}_{my}$	σ_{C_l}	σ_{C_d}	$\sigma_{C_{my}}$	$\sigma_{C_{mx}}$
2.0×10^4	0.86	0.37	0.11	0.032	0.010	0.014	0.006
2.0×10^5	0.88	0.37	0.12	0.034	0.011	0.011	0.007

Table 6.4.: Statistical values of the force and moment coefficients for different Reynolds numbers.

The mean and standard deviation of the force and moment coefficients presented in Tab. 6.4 show a good agreement between both Reynolds numbers. The mean lift coefficients are in good agreement with the value of 0.9 ± 0.045 measured on a similar configuration at $Re = 1.0 \times 10^5$ in [85] (see Fig. 6.20).

The spectral distributions of the force and moment coefficients give essential information to the study of dynamic loads, as they describe the contribution of the fluctuations attributed to individual frequencies to the total variance of the signals. The power spectral density (PSD) of the lift and moment coefficients is compared in Fig. 6.9. Two distinctive peaks can be identified in the spectra at both Re. The first one, detected only in the lift and moment coefficient about the y-axis, is found at about 4 Hz and can be associated to vortex shedding, as it corresponds to a Strouhal number $St = f \cdot c/U_\infty \approx 0.5$ which agrees with experimental data found in [72]. The second one is found in all signals at about 40 Hz and might be related to the tip vortices, since it is detected as only distinctive peak in the signal of the moment about the symmetry axis of the plate in streamwise direction C_{mx}. The plots in Fig. 6.9 show a very good agreement between both Re for frequencies below 40 Hz. For $f > 40$ Hz the high Reynolds number case exhibits higher values of the spectral density. This behavior is attributed to the presence of smaller eddies fluctuating at higher frequencies as Re increases. However, the contribution to the total variance of the signals is less than 3% for $f > 40$ Hz. In analogy to the Reynolds dependency of the energy spectra in isotropic turbulence (see Sect. 2.1.4), it is expected here that larger Re only affects the high frequency range. For this reason, $Re = 2.0 \times 10^4$ can be considered sufficient for studying dynamic loads in the frequency range below 40 Hz. This applies to the heliostat structure presented in Sect. 5, which exhibits the dominant modes of vibration well within this frequency range.

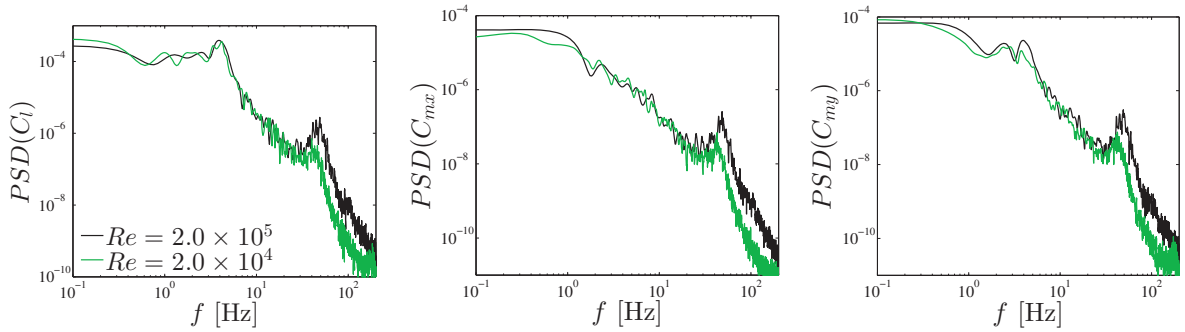

Figure 6.9.: Power spectral density of the lift and moment coefficients for different Reynolds numbers.

6.2.3. Inflow conditions

In addition to the mean velocity profile describing the atmospheric boundary layer, its turbulence characteristics need to be included in the model in order to account for free-stream turbulence effects mentioned in Sect. 2.1.5. For this purpose, the inlet boundary condition used above is extended by adding velocity fluctuations via the vortex method (VM) described in Sect. 2.3.2. To assess the VM and fit its parameters, a new CFD model was generated. It is basically the same model as presented above with the absence of the inclined plate. Thus, a lower grid resolution is required with a total of 1.9×10^6 CVs distributed by $179 \times 119 \times 89$ in streamwise, spanwise and vertical direction, respectively (see Fig. 6.10). Contrary to commonly used guidelines for LES of wall-bounded flows [86], the near-wall region at the ground surface is not fully resolved. Instead, the wall-normal cell distance is set equal to the smallest characteristic dimension of the terrain, i.e. the roughness height $z_0 = 4\,\mathrm{cm}$. This produced maximal values of $y^+ \approx 25$. At this location, the wall shear stress is obtained from the three-layer log-law[2] described in Appendix A.2. The use of wall functions leads to a substantial reduction in the computational effort. This simplification is justified by the following considerations: First, the main objective is to reproduce the overall features of the ABL and to provide realistic inflow conditions for the heliostat, and not to predict accurately the flow features at the ground surface. Second, the height of individual roughness elements on the ground surface is characterized by z_0. Hence, it is not feasible to resolve anything below it.

The model parameters of the VM are determined partly from the turbulence velocity components of the ABL in consideration. From Eq. (2.9) it follows for the normal stresses:

$$\overline{u'^2} = \sigma_u^2 = 21.8\,\mathrm{m^2/s^2} \qquad \overline{v'^2} = \sigma_v^2 = 12.3\,\mathrm{m^2/s^2} \qquad \overline{w'^2} = \sigma_w^2 = 5.5\,\mathrm{m^2/s^2} \tag{6.1}$$

The turbulent kinetic energy is then obtained by:

$$k_t = \frac{1}{2}\left(\overline{u'^2} + \overline{v'^2} + \overline{w'^2}\right) = 19.8\,\mathrm{m^2/s^2} \tag{6.2}$$

The size of the vortices, determined by the turbulent dissipation rate ϵ for a given k_t (see Eq. (2.25)), and the number of vortices N were varied in the ranges between 24-48 $\mathrm{m^2/s^3}$ and 100-500, respectively. The most satisfactory results during these tests were found at $\epsilon = 32\,\mathrm{m^2/s^3}$ and $N = 300$. The effects of ϵ on the results are discussed at the end of this section. Here, only the final results are presented.

Instantaneous snapshots of the flow field are displayed in Fig. 6.11. On the top left plane in Fig. 6.11(a), the generated vortices distributed along the inlet can be clearly observed. Within a short distance from the inlet plane in streamwise direction, three-dimensionality develops in the turbulence field. This can be noticed in the less coherent streamlines displayed in the following planes at $x/c = 2$ and $x/c = 4$. The isosurfaces of λ_2 in Fig. 6.11(b) give also an impression of this development, presenting a wide range of vortical structures preserved through the domain.

[2]The use of rough wall functions [87] is an alternative to predict ground effects more accurately.

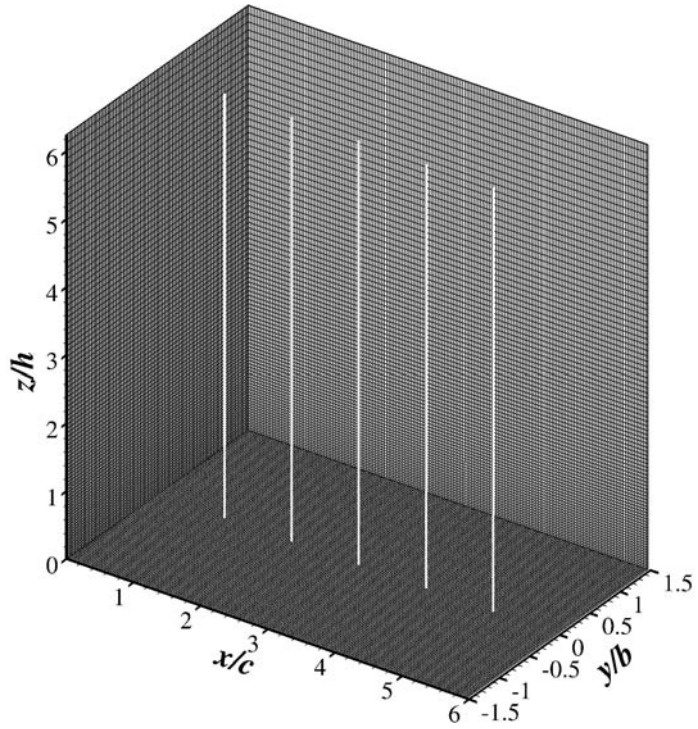

Figure 6.10.: Computational grid. The vertical white lines along the center illustrate the locations where the flow profiles are evaluated.

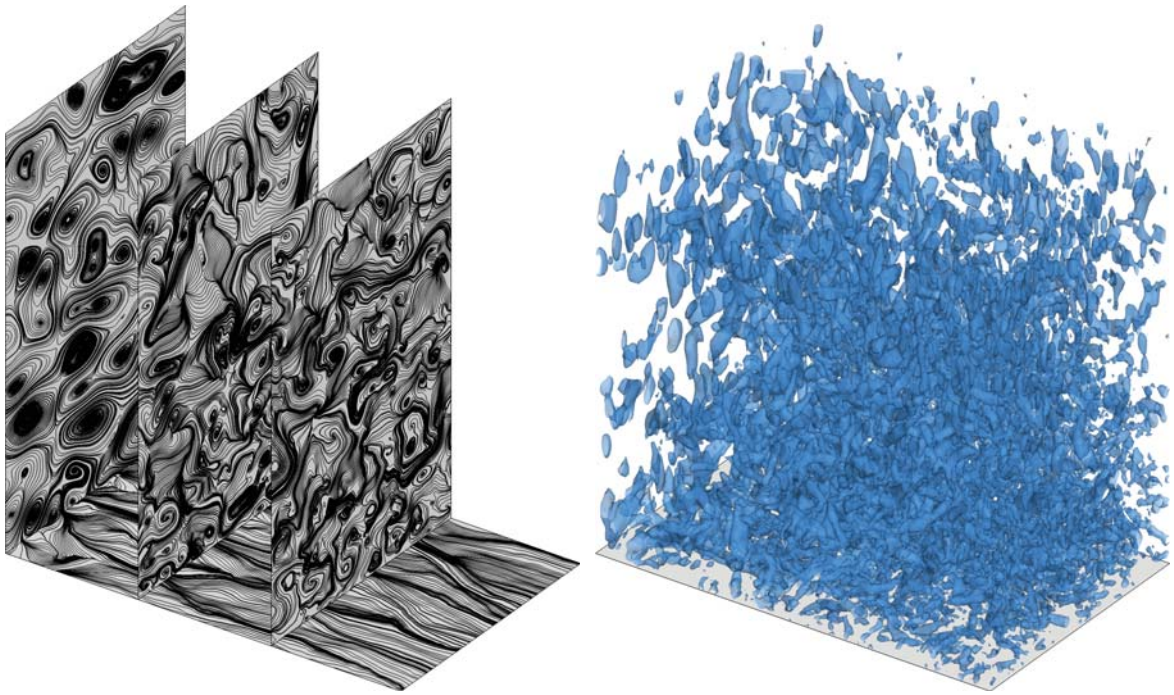

(a) Streamlines

(b) Isosurfaces of $\lambda_2 = -100$

Figure 6.11.: Instantaneous flow developing downstream of the synthetically generated turbulence.

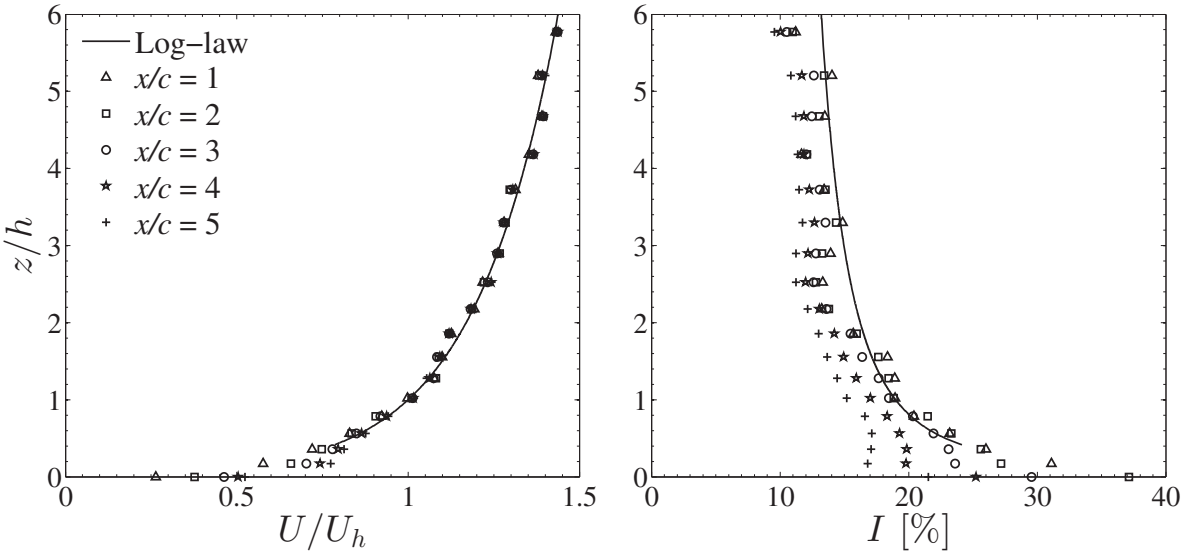

Figure 6.12.: Profiles of mean velocity and turbulence intensity.

Profiles of statistical quantities are evaluated at 5 different locations represented in Fig. 6.10. On the left hand side of Fig. 6.12, the mean velocity scaled by the value at $z = h$ is compared with the prescribed velocity profile. The agreement with the log-law is evident at all locations x/c. Some differences can be observed between the values towards $z/h = 0$ as the near-wall boundary layer develops in streamwise direction. It must be noted that the log-law is not valid close to the wall, hence it can only be displayed for $z/h > 0.4$.

On the right-hand side of Fig. 6.12, the comparison of the total turbulence intensity:

$$I(z) = \frac{\sqrt{\frac{1}{3}\left(\overline{u'^2} + \overline{v'^2} + \overline{w'^2}\right)}}{U(z)} \tag{6.3}$$

is depicted. The differences in the turbulence intensity between the streamwise locations are appreciable at all heights and most noticeable close to the ground. For $x/c > 3$ the turbulence intensity decreases a few percent points as the streamwise coordinate advances. This might be caused by vortex break up and especially by numerical dissipation. Nevertheless, the values in the region where the heliostat plate is located $(2 < x/c < 3, z/h = 1)$ agree very well with the reference. The individual turbulence intensities are analyzed on the left-hand side of Fig. 6.13. Here, the decrease of the intensity in streamwise direction is also noticeable. The streamwise component I_u exhibits the largest discrepancies with the prescribed profile and the magnitudes are comparable with the lateral component I_v. The spectral distribution of the velocity components (also referred to as energy spectra) is shown in the right-hand side of Fig. 6.13. In each plot, the model spectra are compared with the results obtained from two different locations in streamwise direction at the height $z = h$. In addition, a gray area indicates the frequency range where the dominant natural frequencies of the heliostat structure exist.

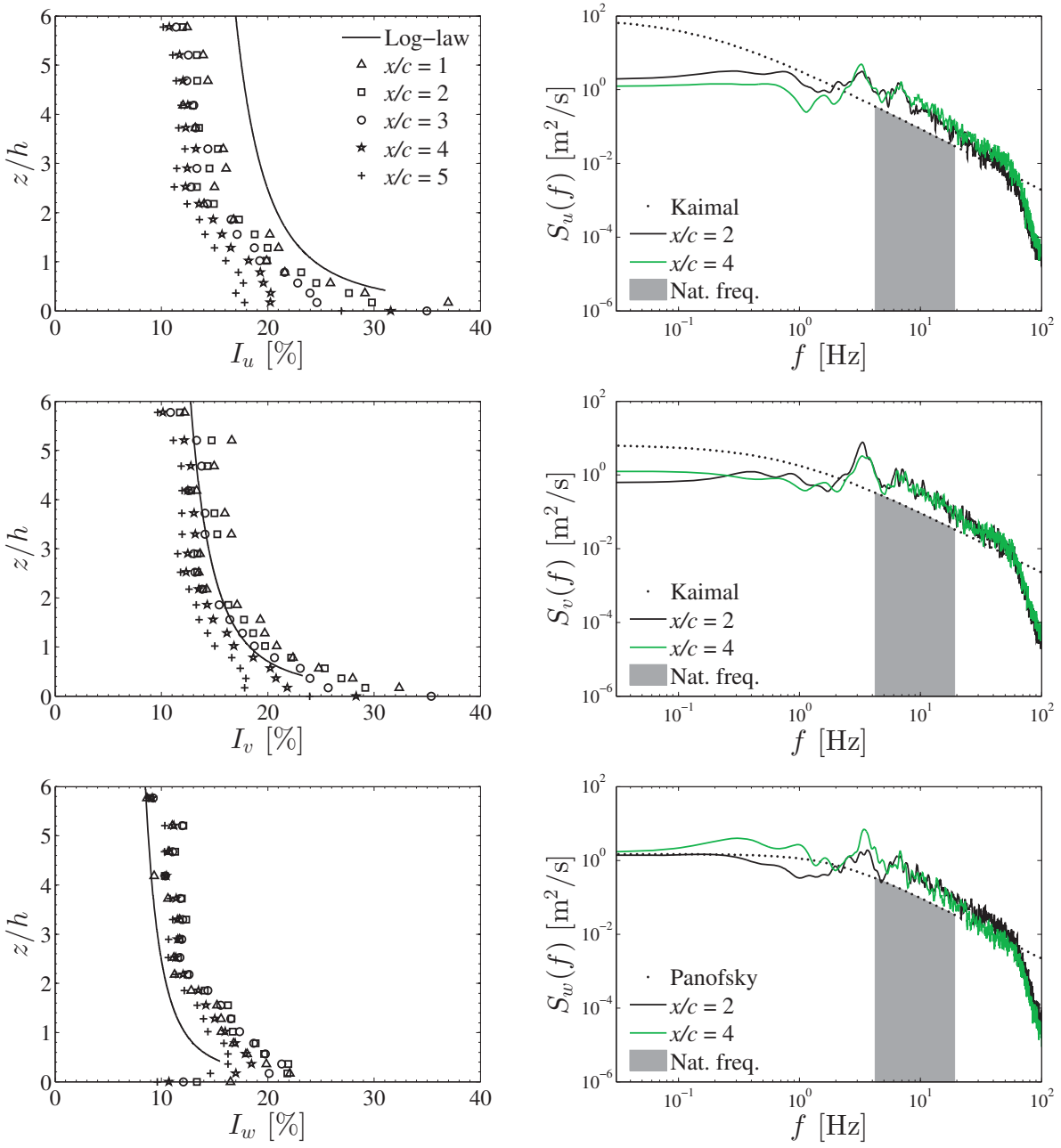

Figure 6.13.: Profiles of turbulence intensities and spectra of velocity components.

The agreement of the simulations with the model spectra is relatively good in the frequency range of interest (i.e., above the gray area) and up to about 50 Hz. For $f > 50$ Hz, the spectral distributions from the numerical results decrease rapidly revealing the unresolved small-scale turbulence which represents, however, less than 5% of the total turbulent kinetic energy estimated from the model spectra. The vertical component $S_w(f)$ presents the best agreement over a wide frequency range, while the largest discrepancies are found in the streamwise component $S_u(f)$ below 1 Hz. The agreement between the two different locations x/c is observable in all cases, indicating that the turbulent kinetic

energy is preserved between these locations. At $f \approx 3.3\,\mathrm{Hz}$ a peak in the spectra can be noticed. It is attributed to the largest eddies produced by the VM. Because velocity reverses across the diameter (D) of an eddy, D can be considered as half of the wavelength (λ) [88]. This simple approximation yields $D = \lambda/2 = U/(2\,f) = 0.9 \times b$ and agrees roughly to the largest eddy diameters that can be observed in Fig. 6.11(a).

Despite the differences identified above, the results are considered satisfactory in reproducing the turbulent ABL for the present application. The discrepancies observed in I_u, and the fact that its magnitudes are similar to I_v, indicate that the anisotropy of the individual components prescribed by the normal stresses in Eq. (6.1) is not fully reproduced by the VM, particularly for the streamwise component $\overline{u'^2}$.

During the tests only the parameter ϵ was varied. This quantity together with k_t is linked to the mean vortex size via the mixing length hypothesis (see Eq. (2.25)). It was found that for a given k_t, increasing ϵ leads to smaller eddies and vice versa. Furthermore, this behavior had an effect on the spectral densities, displacing the energy spectra, as well as the distinctive peak associated to the eddy size, towards higher frequencies as the vortex size decreases. The results of these parameter variations can be found in Appendix B.3. It should be mentioned that the dimensions of the domain have an indirect influence on the results, as they limit the size and number of vortices that can be generated. This is reflected in the discrepancies in the low frequency range of the spectral densities S_u and S_v. Furthermore, it was found that by generating eddies of large size relative to the dimensions of the inflow plane, the time-averaged flow field showed an asymmetrical shape.

6.3. Results and discussion

After finding the appropriate numerical setup and adopting $Re = 2.0 \times 10^4$, two sets of simulations were performed at three different inclinations. One set includes the turbulent ABL via the vortex method and is referred to as **Turbulent**, while the other does not include synthetic turbulence and is referred to as **Smooth**.

The three-dimensional mean flow field around the plate is depicted in Fig. 6.14 by the time-averaged streamlines which are colored by the mean streamwise velocity $\overline{u}$ scaled with the free-stream velocity U_∞. A pair of counter-rotating tip vortices that grow in diameter as they travel downstream along the side edges of the plate can be observed. A separation bubble on the leeward side of the plate that originates from the leading edge is visible at all cases. These characteristic flow features are more noticeable as α increases and under smooth inflow conditions. In the presence of free-stream turbulence the size of the separation bubble is reduced notably. The separation bubble at $\alpha = 20°$ under smooth inflow conditions adopts a v-shape due to the downward induced velocity from the rotation of the tip vortices. Inside the separation bubble a pair of symmetric vortices at each side of the centerline of the plate rotate in opposite directions on the top surface and drive the reversed flow from the center line towards the side edges.

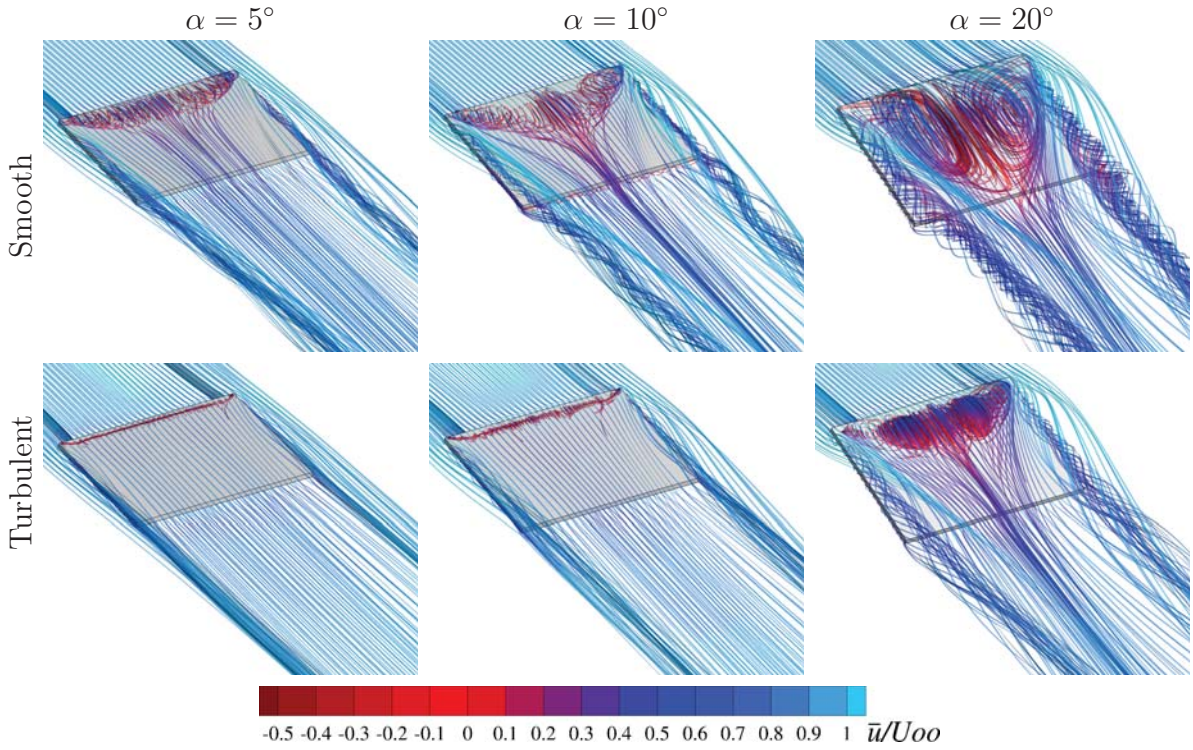

Figure 6.14.: Time-averaged streamlines colored by the scaled mean streamwise velocity.

A substantial reduction of the recirculation region and an earlier reattachment in the presence of free-stream turbulence can be clearly observed in the time-averaged flow field at the symmetry plane $z/b = 0$ shown in Fig. 6.15. This reduction distinguishes both cases at $\alpha = 20°$ particularly, as reattachment at the center of the plate does only take place under free-stream turbulence. The mechanism responsible for this behavior is turbulent mixing, which enhances the rate of entrainment of the fluid with increased turbulent intensity into the wake region as described in Sect. 2.1.5. What appears to be a source point (i.e., streamlines emerging from a point) above the trailing edge for $\alpha = 20°$ under smooth inflow conditions is caused by the 3D structures mentioned above that encounter at this point where the streamlines come from the normal direction of the plane $y/b = 0$. By taking a closer look at the cases for $\alpha = 5°$ in Fig. 6.15, it can be noticed that flow separation takes place on the windward side as well. Furthermore, a small pair of counter-rotating trailing-edge vortices can be identified.

The time-averaged surface streamlines in Fig. 6.16 show clearly the shape of the separation bubble and the region of reattachment. By examining the direction of the streamlines, the 3D flow inside the separation bubble mentioned above is revealed. In both cases at $\alpha = 20°$ the presence of a secondary separation bubble is detected in the upper region towards the leading edge. Similar observations have been found in measurements on inclined flat plates under smooth inflow conditions in [89–91].

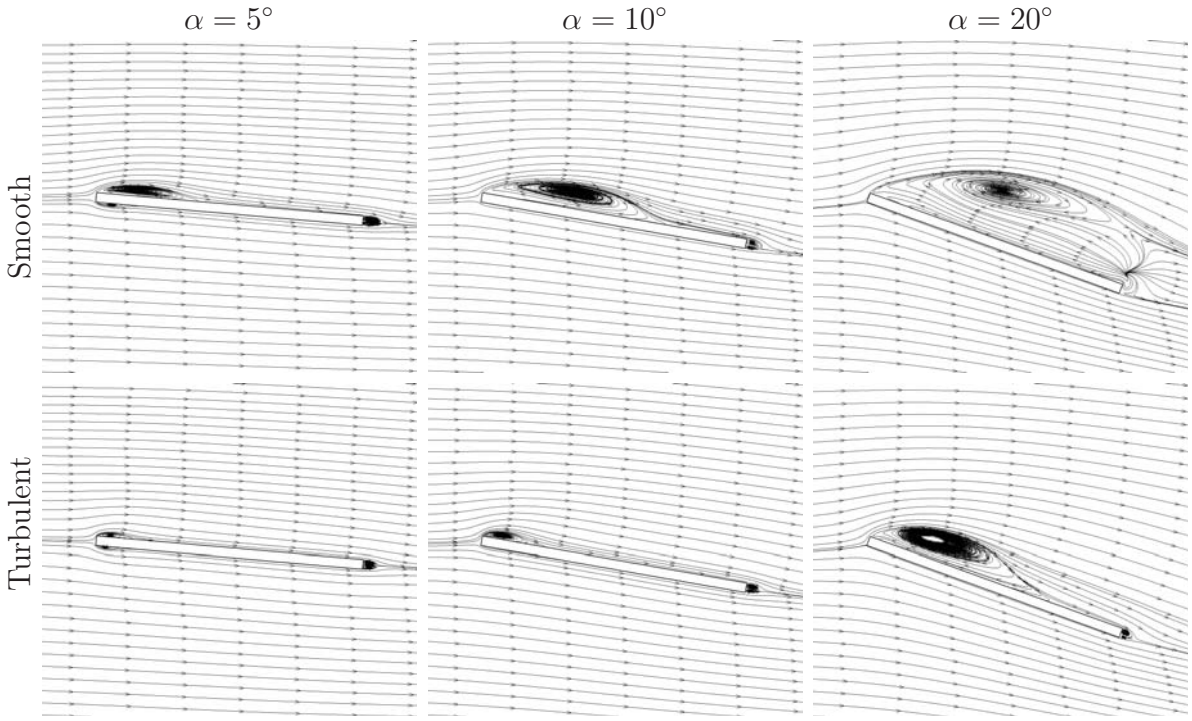

Figure 6.15.: Time-averaged streamlines at the mid-section $y/b = 0$.

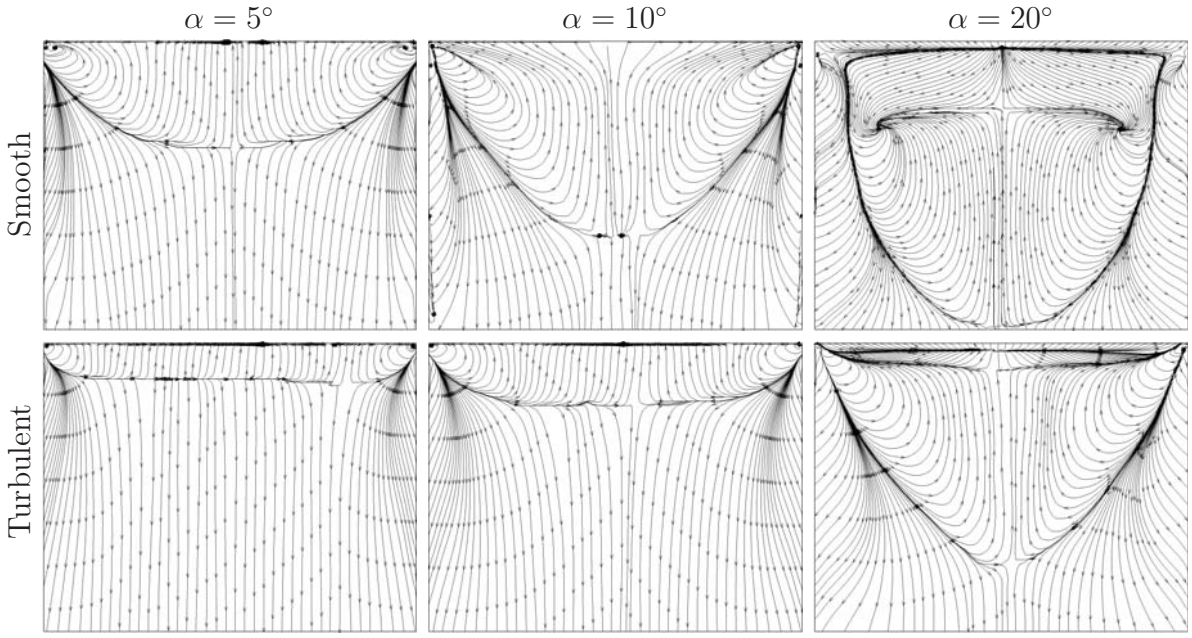

Figure 6.16.: Time-averaged streamlines on the top surface of the plate.

On the bottom surface (see Fig. 6.17), the influence of turbulence can only be noticed at $\alpha = 5°$ in the reduction of the separation bubble, since the flow remains attached for higher angles of attack.

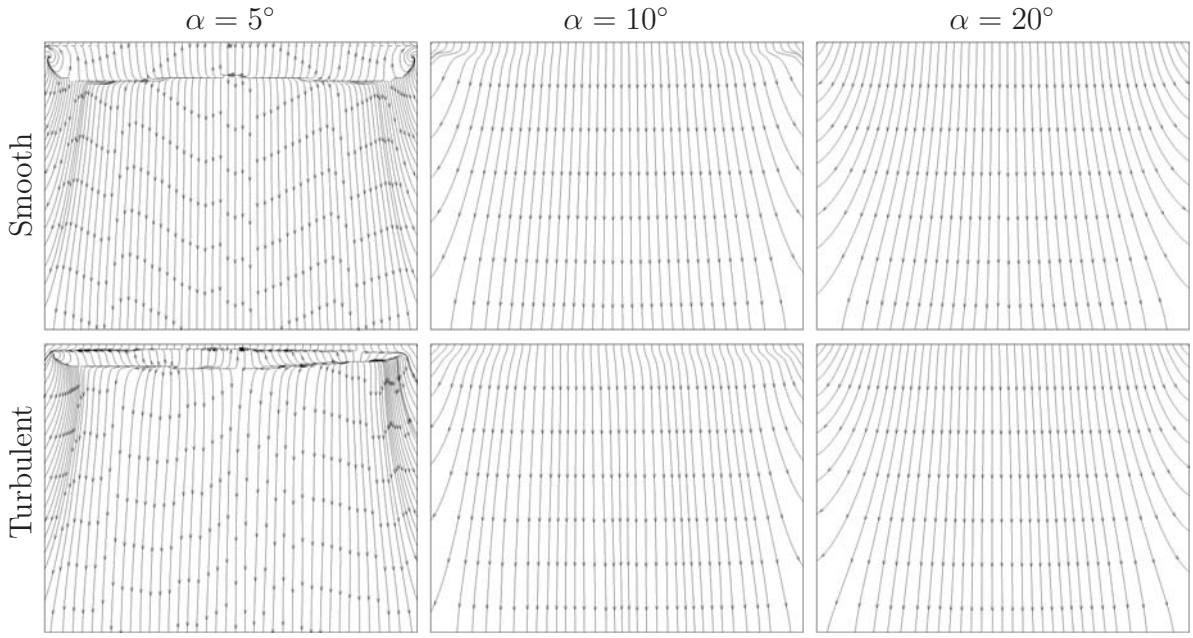

Figure 6.17.: Time-averaged streamlines on the bottom surface of the plate.

The effects of the inlet turbulence can be clearly observed in Fig. 6.18, which shows time-averaged streamlines at the mid-section of the plate in streamwise direction. The area is colored by the velocity magnitude at this plane scaled by the mean streamwise velocity at the height of the heliostat plate. The upper plots show a symmetrical flow field with two distinctive counter-rotating zones and a relatively weak downward flow from the top plane induced by the tip vortices. This is possible by applying the pressure boundary condition described in Appendix A.1 at the top plane that enables backflow for negative pressure gradients at the boundary. The plots at the bottom of Fig. 6.18 exhibit a non-symmetric distribution of the mean flow field with vortical structures distinguishable along the plane. This indicates that the averaging time of $t = 120 \times c/U$ is not sufficient in this case to obtain the mean flow field at this section.

As mentioned in Sect. 6.2.3, the asymmetry is related to the size of the vortices relative to the dimensions of the inflow plane. Large vortices that move relatively slow along planes normal to the streamwise direction induce long-wave fluctuations that increase the averaging period required to achieve a statistically stationary solution. However, the flow in the vicinity of the plate is less affected by the large vortices as shown in Fig. 6.16 and 6.19 where the time-averaged surface streamlines and pressure distribution on the plate show a nearly symmetrical solution. The effects of the averaging time on the load coefficients were analyzed by computing running averages. Within the averaging period used here, the lift coefficients present a statistically converged solution (see Fig. B.1).

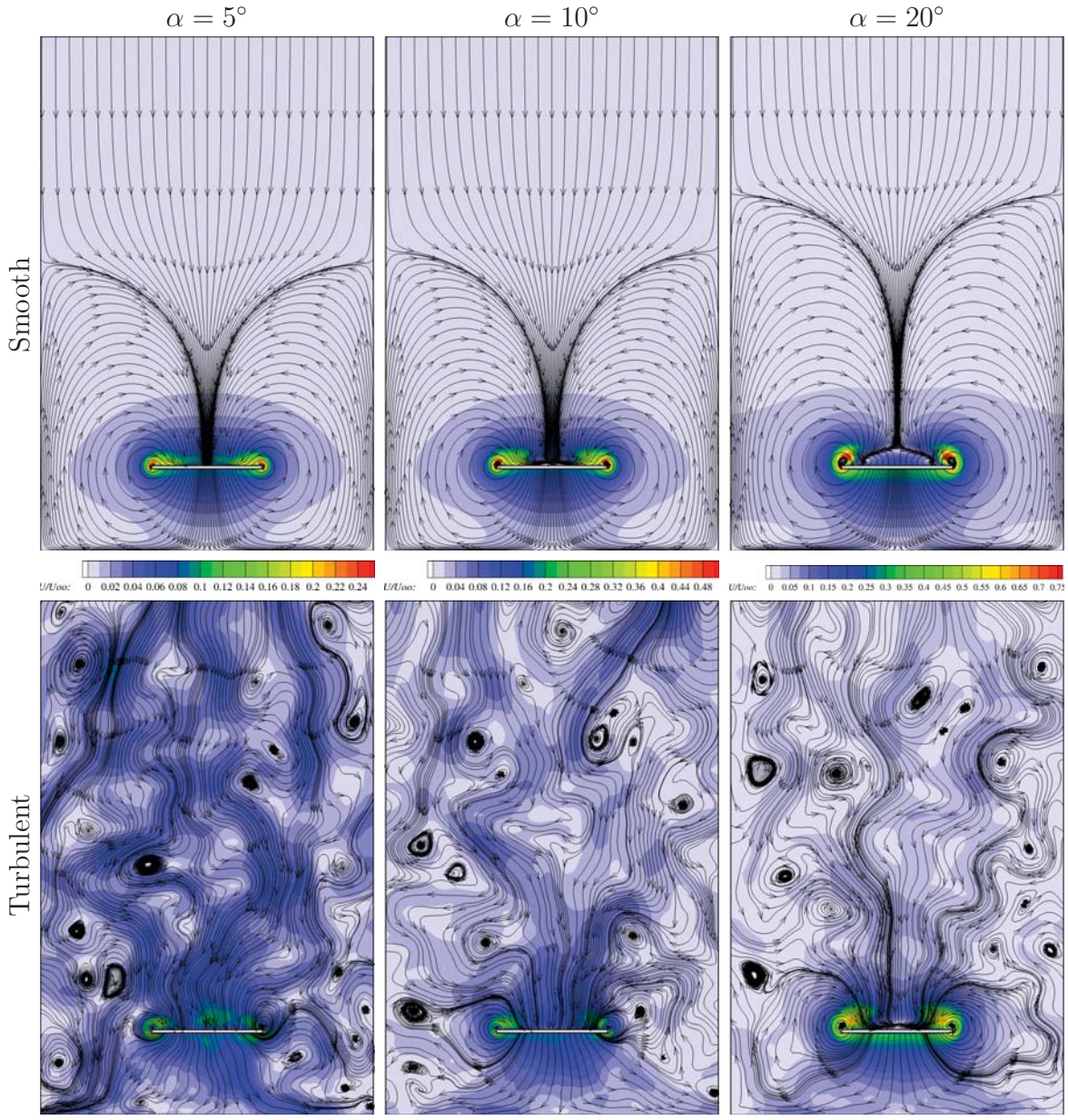

Figure 6.18.: Time-averaged streamlines at the mid-section $x_t/c = 0.5$.

The pressure distribution on the plate is visualized in Fig. 6.19 by the normalized time-averaged pressure difference:

$$\overline{C}_{dp} = \frac{\overline{p}_t - \overline{p}_b}{\frac{1}{2}\rho U_h^2} \tag{6.4}$$

where $\overline{p}_t$ and $\overline{p}_b$ are the time-averaged static pressures on the top and bottom surfaces, respectively, normalized by the dynamic pressure which is calculated with the mean velocity $U(z = h)$. This quantity is a measure of the strength and direction of the resulting wind loads acting on the plate. The influence of turbulence on the time-averaged pressure distribution is evident, and results from the changes in the separation bubbles.

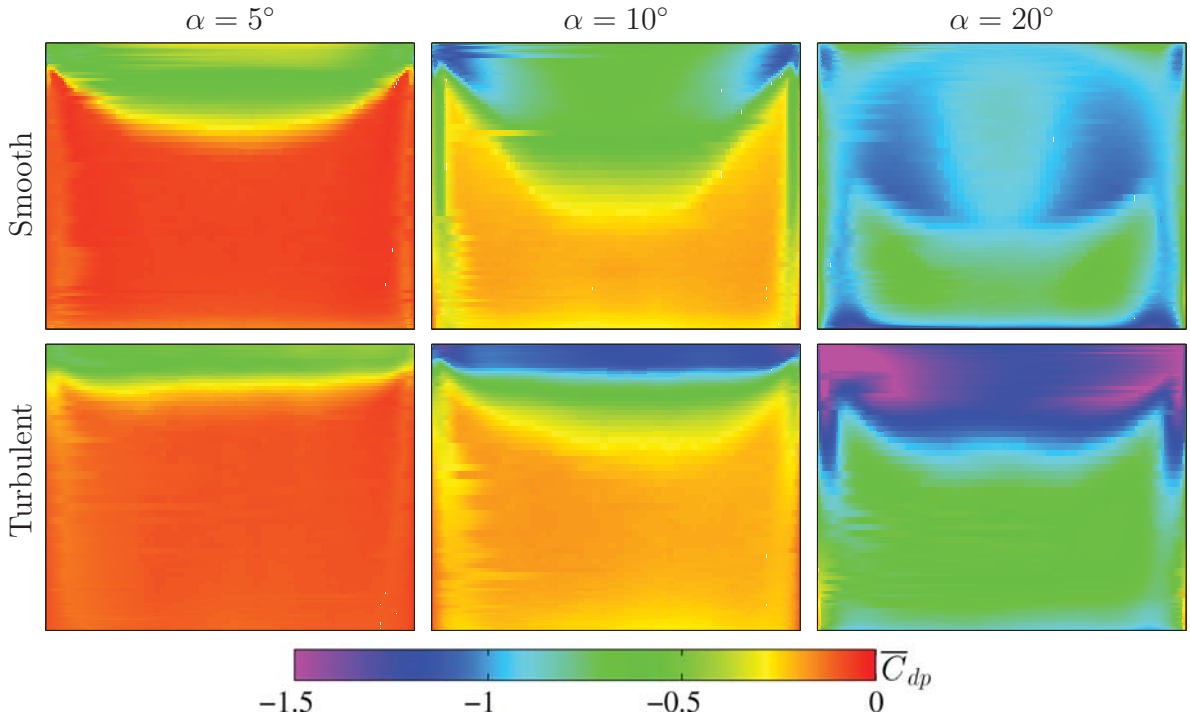

Figure 6.19.: Time-averaged pressure difference coefficient defined by Eq. (6.4).

Despite the differences in the pressure distribution, the mean values of the load coefficients presented in Tab. 6.5 are not affected significantly. Only the mean lift coefficient ($\overline{C}_l$) shows a small decrease with the introduction of the turbulent inflow condition, while the mean moment coefficient ($\overline{C}_{my}$) increases slightly at $\alpha = 20°$. The mean values of the lift coefficient under smooth inflow conditions agree very well with experimental data from [85] measured on a plate with side ratio $b/c = 1.25$ (see Fig. 6.20). Unlike the mean values, the raise in the standard deviations due to free-stream turbulence is substantial at all cases. The largest increments are found at $\alpha = 5°$ and the differences between both cases decrease when increasing the elevation angle. This is related to the weaker dependency on the elevation angle of the values belonging to the turbulent case, which is most notable in the moment coefficients.

Inlet BC	α	$\overline{C}_l$	$\overline{C}_d$	$\overline{C}_{my}$	σ_{C_l}	σ_{C_d}	$\sigma_{C_{my}}$	$\sigma_{C_{mx}}$
Smooth	5°	0.19	0.07	0.05	0.010	0.001	0.001	0.000
Turbulent	5°	0.17	0.07	0.04	0.219	0.051	0.042	0.025
Smooth	10°	0.41	0.13	0.09	0.011	0.002	0.002	0.001
Turbulent	10°	0.36	0.12	0.09	0.234	0.067	0.041	0.023
Smooth	20°	0.86	0.37	0.11	0.032	0.010	0.014	0.006
Turbulent	20°	0.83	0.36	0.17	0.300	0.138	0.035	0.025

Table 6.5.: Statistical values of force and moment coefficients for different inclinations and inlet boundary conditions.

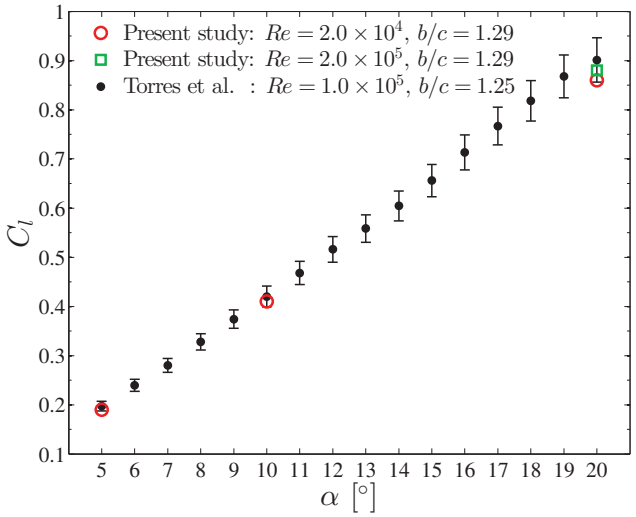

Figure 6.20.: Mean lift coefficient of a flat plate at different angles of attack α [85].

As can be expected, the spectral distributions of the moment coefficients are notably affected by the inclusion of turbulence in the oncoming flow. This is observable in the comparison shown in Fig. 6.21, where the values including turbulence exhibit higher magnitudes of the spectral density. The enhancement in the PSD curves for the moment coefficients can be noticed over almost the entire frequency range. However, at about 80 Hz the amplitudes are similar. As mentioned before, this frequency is associated with fluctuations generated by the tip vortices. In the presence of turbulence, this peak is no longer distinctive. This can be attributed to the amplification of the amplitudes below and above this peak, caused by fluctuations of the incident flow in this frequency range. In addition, the sustained shape of the tip vortices under smooth flow conditions is destructed by turbulence (see Fig. 6.22), affecting their contribution to the fluctuating loads.

At 3.8 Hz a pronounced peak is observed in the spectral distribution of the moment coefficients. Even though vortex shedding is expected near this frequency, no visual evidence of an enhancement of the leading or trailing edge vortices could be observed in the results. During the preliminary tests to determine the appropriate turbulent inflow conditions presented in Sect. 6.2.3 a peak in the velocity spectra was found close to this frequency. Therefore, this peak is attributed to the effects of the largest eddies of the oncoming flow on the loads (see Fig. 6.13).

Figure 6.22 illustrates how free-stream turbulence changes considerably the distinctive flow features appreciable under smooth inflow conditions. The separation bubble and the relatively stable tip vortices convected along the wake under smooth inflow conditions are not clearly visible in the presence of free-stream turbulence.

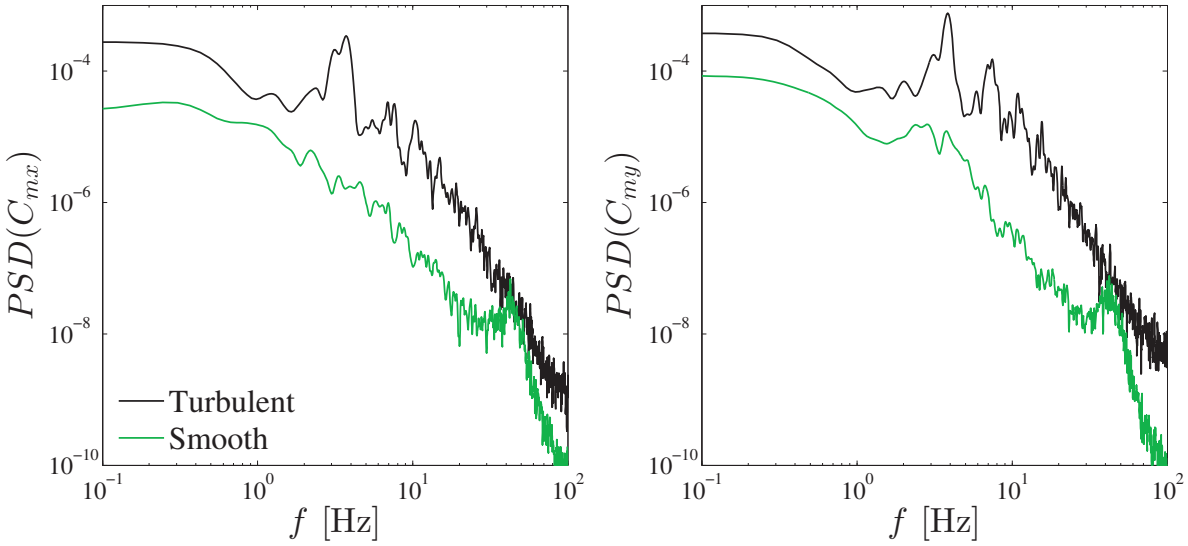

Figure 6.21.: Power spectral distributions of the moment coefficients for $\alpha = 20°$.

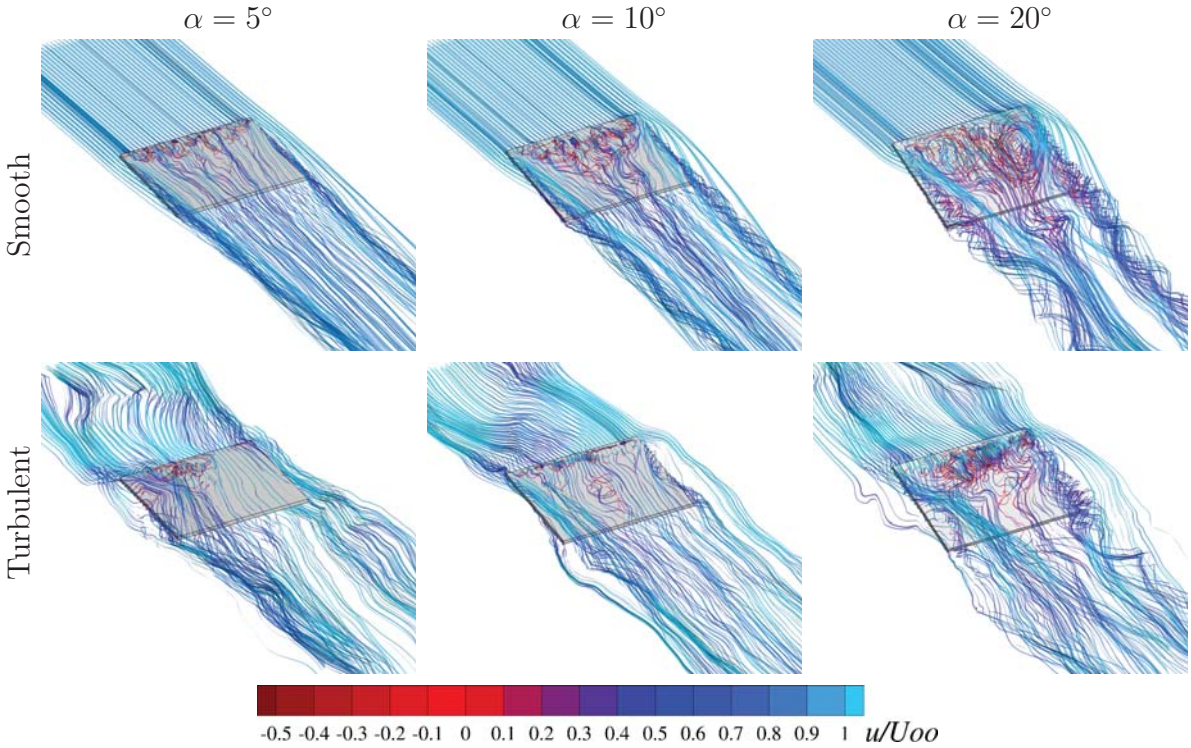

Figure 6.22.: Instantaneous streamlines colored by the scaled streamwise velocity.

6.4. Conclusions from flow simulations

The results of the flow simulations confirm the importance of accounting for turbulence when modeling the ABL. The enhancement of the fluctuating loads due to free-stream

turbulence is significant. The effects were observed over a wide spectral range, including the frequency range of interest. Even though the mean load coefficients are not affected substantially by turbulence, the resulting mean pressure distribution changes notably. The effects of free-stream turbulence on the flow field, known from other studies and described in Sect. 2.1.5, are clearly reproduced by the results. Likewise, the results obtained with smooth flow conditions are in accordance with experimental data found in [83, 85, 89, 90].

The time signals of the pressure difference along the plate were recorded during simulations for a period of $t = 120 \times c/U = 15\,\mathrm{s}$. The pressure difference represents the fluctuating wind loads and is used as boundary condition on the FE model to perform dynamic simulations. Furthermore, the spectral distributions of the velocity components u, v, w and load coefficients C_{mx} and C_{my} provide valuable information to derive relationships for the response prediction explained in the following chapters.

7. Dynamic simulation of the heliostat

After developing the FE model that reproduces the dynamic properties of the heliostat and generating time-dependent pressure loads via CFD simulations, a dynamic model is created by coupling the FE model with the CFD results and performing transient simulations. The objective here is to predict the dynamic behavior of the heliostat structure under realistic wind conditions at an acceptable computational effort. In Sect. 7.1, the numerical model is described and the necessary simplifications are explained. Numerical convergence is also discussed in this section. After that, the simulation results are presented and discussed in Sect. 7.2. Thereby, the effects of the dynamic loads on the quantities of interest are analyzed at specific operating conditions. The chapter ends with the conclusions from the dynamic simulations in Sect. 7.3.

7.1. Numerical methodology

The transient analysis is performed using the FE model described in Sect. 5.3. Initial conditions were obtained from a static simulation including only gravitational forces. A time-dependent pressure distribution was applied as load boundary condition on the mirror surface. The pressure load was obtained from the CFD results presented in Sect. 6.3 that include inflow turbulence by computing the pressure difference between the top and bottom surface of the plate at 225 points distributed as shown in Fig. 7.1. The points are clustered towards the edges to resolve the pressure gradients accurately.

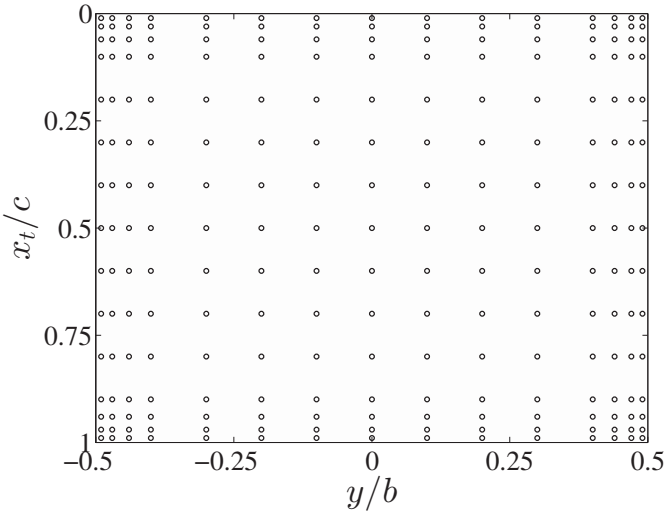

Figure 7.1.: Locations of pressure signals.

The semi-discrete equation of motion Eq. (2.32) needs to be integrated over time with a temporal resolution that resolves adequately the load signal. Thus, the temporal resolution of the load signal and its interval length have an effect on the computational effort. For this reason, the pressure signals were re-sampled from 8000 Hz, which corresponds to the full temporal resolution of the CFD simulations, down to 80 Hz by simply using every 100th sample. This is motivated by the fact that the expected response frequency of the structure, based on the modal analysis, is below 20 Hz. According to the Nyquist criterion [92], the re-sampled signals enable a maximal resolution of 40 Hz, i.e., two times the maximal frequency of interest.

In order to avoid errors by the loss of information or distortion of the load signals by aliasing[1] effects, it is important to evaluate the effects of the reduced spatial and temporal resolution. For this purpose, the moment coefficients were computed from the pressure signals of the 225 points sampled at 80 Hz and compared with the values obtained from a built-in function of the CFD code that computes the moment coefficients by integrating the pressure over all 7448 surface grid elements on the plate at every time step, i.e., a sampling rate of 8 kHz. Figures 7.2 and 7.3 present the effects of reducing the sampling rate on the moment coefficients. In Fig. 7.2 the comparison of the time signals of the moment coefficients show that the high frequency content of the original signal sampled at 8 kHz is filtered out, while keeping the principal fluctuations at lower frequencies when re-sampling at 80 Hz. In the frequency domain shown in Fig. 7.3, the filtering operation can be identified by the cut-off frequency at 40 Hz in the light gray surface. The spectral distributions agree very well over the entire frequency range, including the frequencies of interest. A difference of only 1% and less than 5% is found between the original and re-sampled signals in the mean and standard deviation of C_{my}, respectively.

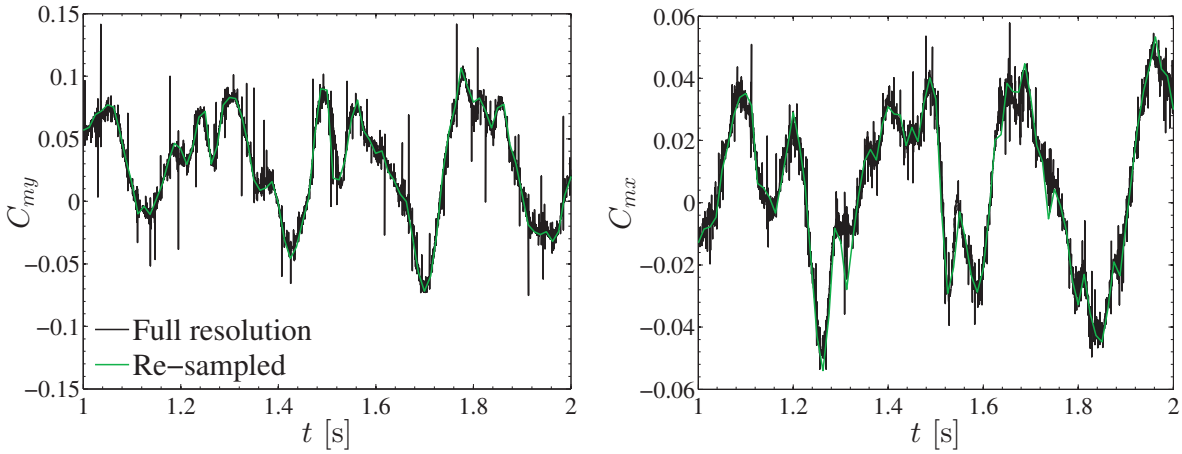

Figure 7.2.: Comparison of time signals of moment coefficients for different sampling rates and spatial resolutions.

[1] Aliasing is the introduction of non-existent low frequency components by using a too low sampling rate.

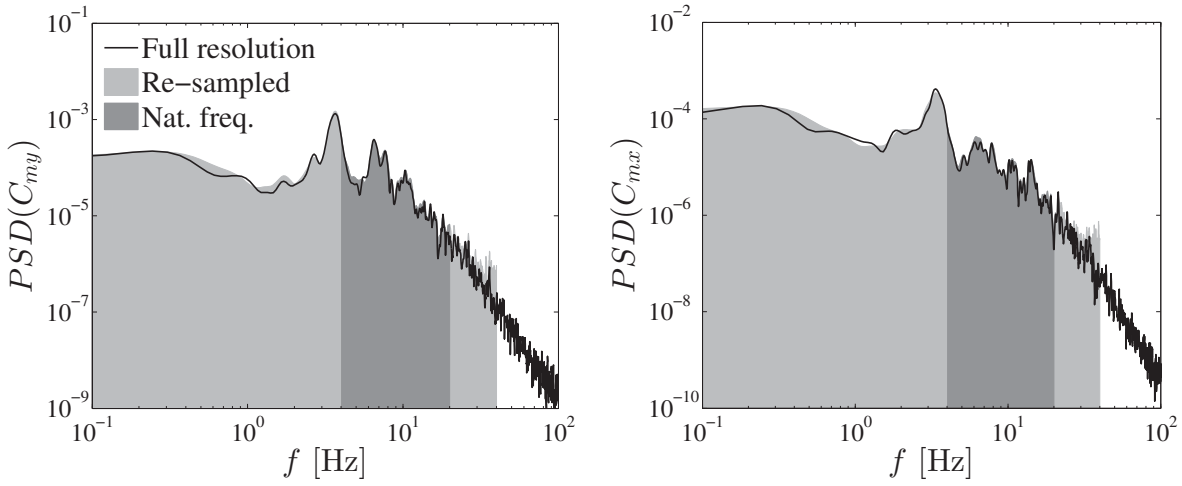

Figure 7.3.: Comparison of power spectral densities of moment coefficients for different sampling rates and spatial resolutions.

The semi-discrete equation of motion Eq. (2.32) is solved by the Hilber-Hughes-Taylor (HHT) method [93], which is a single-step implicit time integration algorithm of second-order accuracy. In order to obtain a converged solution and resolve adequately the load signals, several time steps are required between the time points at which the load signal is given (i.e., every $1/80 = 12.5 \times 10^{-3}$ s), called *load steps*. During integration, the load values are interpolated linearly at each time step. The following condition for the time step size is recommended in [59] to resolve accurately the response frequencies of the structure: $\Delta t \leq 1/(20 \times f_{max})$, where f_{max} is the highest frequency of interest. A time step size $\Delta t = 2.5 \times 10^{-3}$ s was selected after performing preliminary simulations. Figure 7.4 shows convergence in the solution of a response time signal for $\Delta t \leq 2.5 \times 10^{-3}$ s. This value satisfies the condition given above for $f_{max} = 20$ Hz equal to the highest frequency of interest taken from the modal analysis.

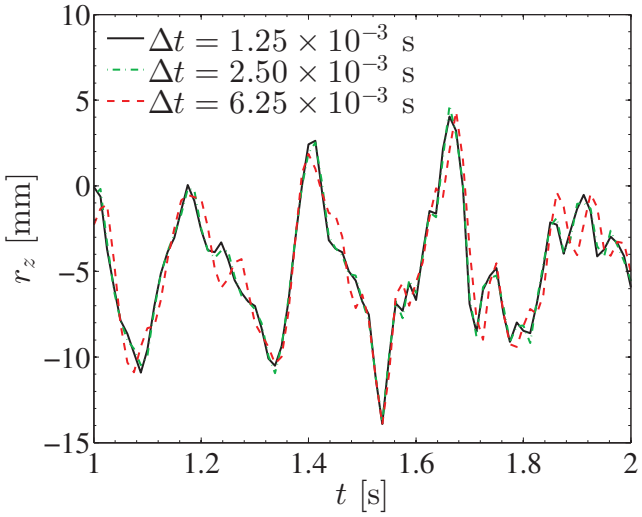

Figure 7.4.: Displacement r_z on a corner of the frame for different time step sizes.

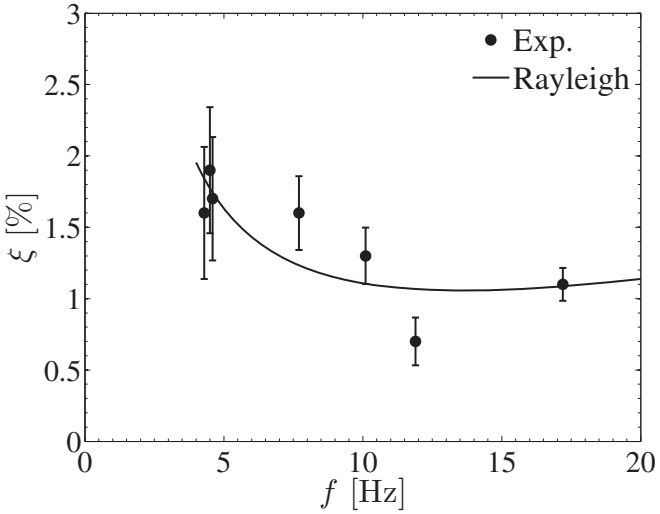

Figure 7.5.: Rayleigh damping approximation and experimental data from Tab. 5.3.

Structural damping is accounted for via the Rayleigh damping hypothesis described in Sect. 2.5. The Rayleigh coefficients $R_M = 9.039 \times 10^{-1}\,1/\mathrm{s}$ and $R_K = 1.237 \times 10^{-4}\,\mathrm{s}$ (see Eq. (2.34)) were computed by a least-squares algorithm. Figure 7.5 compares the damping coefficients from the modal analysis given in Tab. 5.3 with the Rayleigh approach as a function of the frequency. Due to the simplicity of this approach, only the level and trend of the damping coefficients can be approximated. Nevertheless, the values are within the accuracy of most of the experimental data points.

7.2. Results and discussion

Transient FE simulations were performed with the load conditions taken from the flow simulations including free-stream turbulence. The total deformation of the structure was evaluated at every load step. The deformations at the instant of the maximal displacement detected over the entire simulation time are shown in the bottom of Fig. 7.6 for different elevation angles. The orientation of the heliostat is similar to the illustrations of the 3D flow shown in Fig. 6.14. The deformations are amplified by a factor of 10 and the black edge lines represent the non-deformed state. The location of the largest displacements were identified at the lower left corners of the frame. When comparing the transient solution with the third mode shape from the modal analysis displayed in the top figures, it is evident that this deformation corresponds to mode 3. By analyzing animations of the transient results, it was confirmed that this mode, which describes an oscillation of the frame about its largest symmetry axis (y), is the most distinctive and frequently observed motion at all elevation angles investigated. This is due to the direction of this mode shape. As mentioned in Chap. 5, out-of-plane modes, such as mode 3, are more susceptible to pressure fluctuations as they excite the structure in surface-normal direction. Moreover, the presence of turbulence and vortex shedding induce fluctuations that affect the instantaneous moment M_y which is responsible for the oscillations of the frame about the elevation axis.

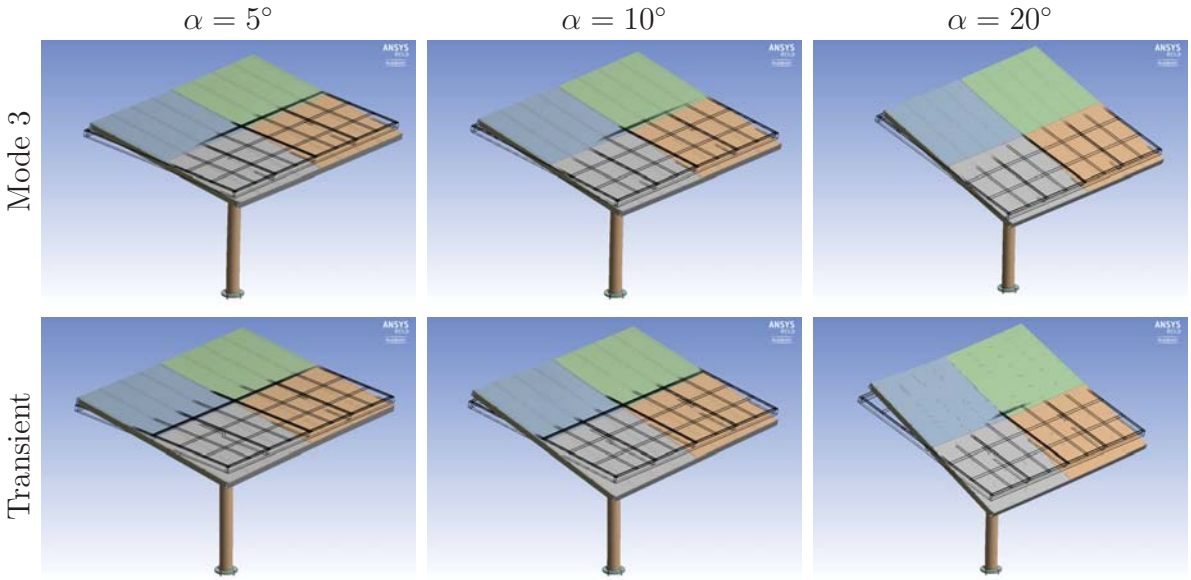

Figure 7.6.: Identification of the dominant mode shape for different elevation angles.

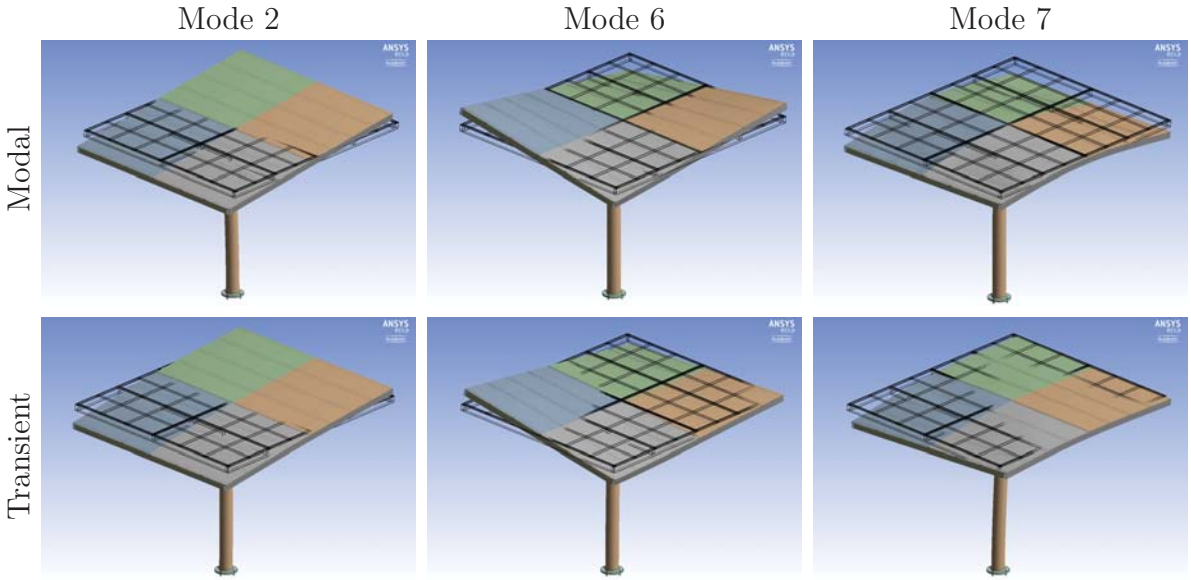

Figure 7.7.: Identification of distinctive mode shapes in transient results at $\alpha = 5°$.

Other less dominant mode shapes were revealed by analyzing in detail the transient results. Figure 7.7 illustrates three different instants when the oscillations are associated to different modes shapes. Oscillations of the frame about its shortest symmetry axis (x_t), corresponding to mode shape 2, were often observed in the animations, whereas motions resembling mode 6 and 7 were less frequent. These three types of oscillations are caused by instantaneous asymmetrical pressure distributions on the plate. Velocity fluctuations normal to the plate and self-induced turbulence phenomena, such as tip vortices, might be their main sources.

In the following analysis the heliostat structure subjected to wind loads is viewed as a system consisting of an input and output. The loads integrated from the pressure distribution are the input quantities denoted by the index *in*, while the reaction loads in the structure which include the effects of inertial forces are the output quantities denoted by *out*. In order to analyze resonance effects and the contribution of inertial forces on the dynamic loads, the output (reaction) moment about the elevation axis $M_{y,out}$ is evaluated. It is computed from the total forces acting on the elevation drive. For comparison purposes $M_{y,out}$ is multiplied by -1 throughout the analysis, yielding, by definition (see Fig. 3.2), the same sign as the input moment.

In Tab. 7.1 different statistical values of $M_{y,out}$ are presented for each elevation angle. In addition to conventional statistical values, e.g., mean $\overline{M}_{y,out}$, standard deviation $\sigma_{M_{y,out}}$ and maximum $\hat{M}_{y,out}$, three additional quantities are derived to evaluate the contribution of the fluctuating part of the output moment. The peak factor, which is used to estimate the peak value of a normal distributed quantity (see Sect. 8.1), is calculated from:

$$k_{M_{y,out}} = \frac{\hat{M}_{y,out} - \overline{M}_{y,out}}{\sigma_{M_{y,out}}}. \tag{7.1}$$

The ratio of standard deviation to mean value is given by:

$$T_{M_{y,out}} = \frac{\sigma_{M_{y,out}}}{\overline{M}_{y,out}}. \tag{7.2}$$

The gain factor G_{M_y}, which quantifies the average amplification of the input moment due to dynamic effects, is defined as the ratio of the standard deviations of the output to input moment by:

$$G_{M_y} = \frac{\sigma_{M_{y,out}}}{\sigma_{M_{y,in}}}. \tag{7.3}$$

The mean value of the output moment increases almost linearly with the elevation angle similar to the normalized input moment given by the moment coefficient $\overline{C}_{my}$ in Tab. 6.5. The standard deviation, which characterizes the fluctuating part of the output, remains nearly constant. This is due to the fact that the fluctuating part of the input moment, represented by $\sigma_{C_{my}}$, as well as the dynamic properties, described by the modal parameters f_n and ξ, are independent of α. This behavior implies that the contribution of the fluctuating component to the total output increases when decreasing α. This is reflected in $T_{M_{y,out}}$, which exhibits a threshold at $\alpha = 10°$ where static and averaged fluctuating components are equal. The peak factors of the output moment are in the range of 3-5 as expected for a Gaussian process [17] and increase linearly with α which is in accordance to the behavior of highly separated flows where peak factors of the pressure coefficient have been found between 6-7 and up to 10 in [94, 95]. The gain factors, with values above 2 in all cases, indicate a significant amplification of the fluctuating wind loads caused mainly by resonance effects associated to the excitation of the dominant mode 3 identified in Fig. 7.6.

α [°]	$\overline{M}_{y,out}$ [Nm]	$\sigma_{M_{y,out}}$ [Nm]	$\hat{M}_{y,out}$ [Nm]	$T_{M_{y,out}}$	$k_{M_{y,out}}$	G_{M_y}
5	196	497	1902	2.5	3.6	2.3
10	443	465	2254	1.0	4.1	2.2
20	846	493	3383	0.6	5.1	2.8

Table 7.1.: Statistics of output moment for different inclinations.

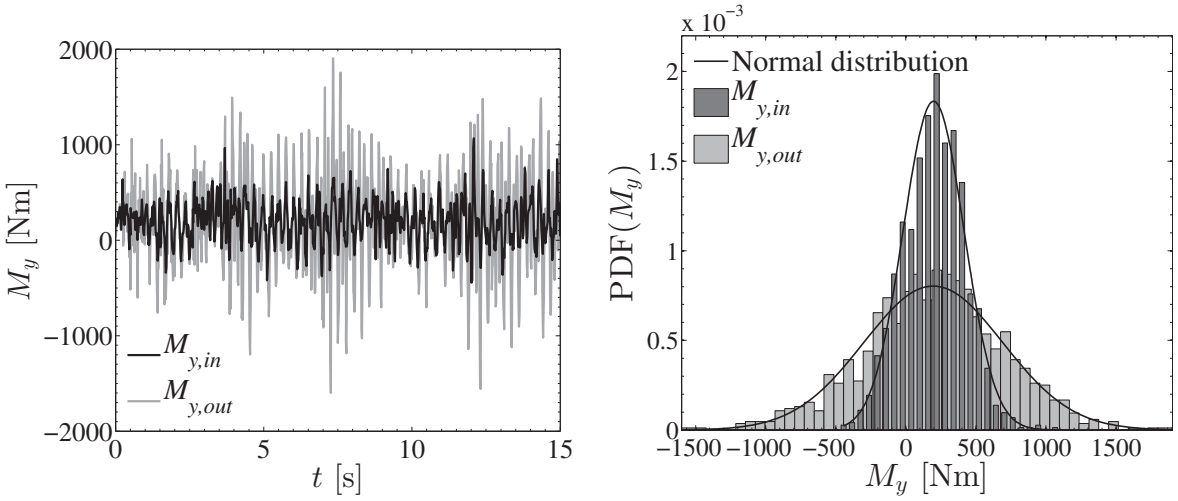

Figure 7.8.: Input and output moments about the elevation axis.

The dynamic effects on the loads are of special interest at low elevation angles at which the heliostats are set during strong wind conditions. Hence, for $\alpha = 5°$ the time signals and probability density function of the input and output moment is compared in Fig. 7.8. Both time signals exhibit a random behavior that follows a normal distribution with the same mean magnitudes. It is noticeable that the output signal reaches larger magnitudes which leads to a wide spread PDF.

In the frequency domain, the linear relationship between input and output moments is described by the frequency response (transfer) function $H_{M_y}(f)$. Its squared magnitude can be obtained from the ratio of the power spectral densities as:

$$|H_{M_y}(f)|^2 = \frac{S_{M_{y,out}}}{S_{M_{y,in}}} \tag{7.4}$$

If, at any frequency, the magnitude of the input and output are identical, then the transfer function is unity. If the system amplifies the vibration, then the transfer function will be greater than unity [96]. This behavior is reproduced in Fig. 7.9 where distinctive peaks, marked by circles on the graph, are identified at the natural frequencies of specific modes. As expected, mode 3 and 4, which have been associated above and in Sect. 5.4.1 with oscillations about the elevation axis, are identified in the FRF. Mode 7 and 8 (see Fig. C.2), which are bending modes of the frame about the x_t axis, are also detected in the FRF as they induce a moment about the elevation axis when the center position of

the trailing edge (i.e., position (1) in Fig. 3.2) oscillates out-of-phase with the corners of the frame.

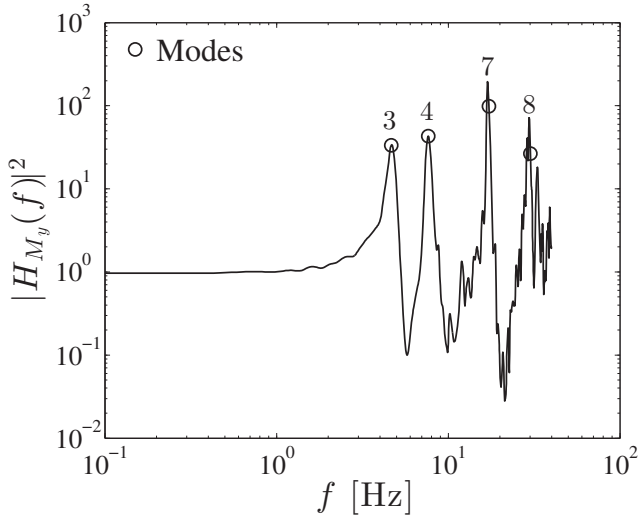

Figure 7.9.: Frequency response function (FRF) for the moment about the elevation axis.

The average displacement normal to the mirror surface $\overline{r}_{zi}$, its peak value $\hat{r}_{zi}$ and standard deviation $\sigma_{r_{zi}}$ were computed at the positions $i = 0, 1$, and 2 (see Fig. 3.2) on the bottom left facet of the frame. The values are presented in Tab. 7.2 for different elevation angles. It can be noticed that the mean value increases almost linearly with the elevation angle, while the standard deviations do not change significantly with α. A similar dependency on the elevation angle is observed in the statistical values of the corresponding load components $\overline{C}_{mx}$ and $\overline{C}_{my}$ presented in Tab. 6.5 for the cases including turbulence. The ratio $\sigma_{rz_1}/\sigma_{rz_2}$ is approximately 2 in all cases. The magnitude of $\hat{r}_z$ is relatively small in all cases and corresponds to less than 1% of the chord length c.

α	$\overline{r}_{z0}$	$\overline{r}_{z1}$	$\overline{r}_{z2}$	$\sigma_{r_{z0}}$	$\sigma_{r_{z1}}$	$\sigma_{r_{z2}}$	$\hat{r}_{z0}$	$\hat{r}_{z1}$	$\hat{r}_{z2}$
5°	-1.2	-1.3	0.0	4.9	4.5	2.0	-16.8	-14.8	7.2
10°	-2.5	-2.9	0.6	4.9	4.2	2.3	-22.1	-18.4	7.6
20°	-4.4	-5.3	1.9	4.9	4.4	2.1	-22.9	-21.6	8.9

Table 7.2.: Statistics of vertical displacement in [mm] at three positions (see Fig. 3.2).

For the case $\alpha = 20°$, which is an elevation angle that can be found during operation, the angular deviation δ of the mirror surface-normal vector with respect to its initial value was computed for each load step by averaging over 16 surface segments. The time-averaged value and standard deviation are $\overline{\delta} = 5.3\,\text{mrad}$ and $\sigma_\delta = 2.8\,\text{mrad}$, respectively. The slope error, which is given by the standard deviation of the nominal value, was computed from the root-mean-square as:

$$\text{RMS}(\delta) = \sqrt{\overline{\delta}^2 + \sigma_\delta^2} = 6.0\,\text{mrad} \tag{7.5}$$

The mean value has the largest contribution to the slope error and results from the static part of the wind load, while the standard deviation represents the dynamic effects and has a smaller contribution. Nonetheless, it still significantly influences the target value given in Sect. 2.1 by 1-2 mrad. Experimental results on large heliostats [97] measured a slope error of 3.9 mrad at a wind speed of 12 m/s.

The time signals of the vertical displacements follow a normal distribution as can be observed in Fig. 7.10. The angular deviation, however, is not Gaussian. Instead, δ follows the *non-central χ-distribution*. This is due to the fact that δ depends on both oscillations about the principal axes of the frame x_t and y. Therefore, δ can be determined from the vertical displacements r_{z1} and r_{z2} by assuming small deformations (see Eq. (8.28), (8.21) and (8.11)). For this reason, the non-central χ-distribution, that will be described in Sect. 8.4, fits very well to δ as it reproduces the PDF of a quantity that depends on two normal distributed variables.

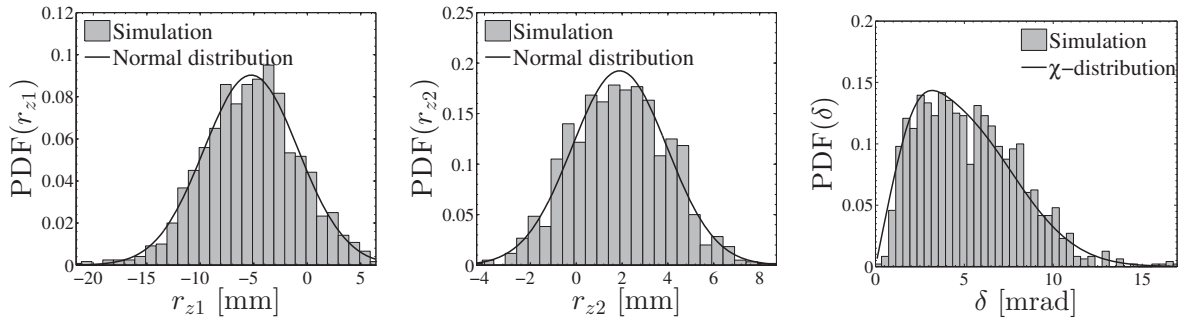

Figure 7.10.: Probability density functions of vertical displacements and angle deviations of the normal vector for the case $\alpha = 20°$.

7.3. Conclusions from dynamic simulations

The dynamic results have shown which modes are principally affected by fluctuating wind loads. As expected, mode shapes describing oscillations out of the mirror plane are the most characteristic motions in the transient results. The most frequently observed vibrations are associated with mode 3, which is also responsible for the largest displacements of the structure at all elevation angles investigated. The amplification of the reaction moment about the elevation axis is substantial and confirms the importance of accounting for dynamic effects. The maximal displacements were observed at the corners of the frame. However, the peak values are less than 1 % of the chord length which justifies the application of one-way coupling between the CFD and FEM analysis that relies on small deformations. The statistical values of the displacements indicate a linear behavior of the system. The analysis of the angular deviation of the mirror normal vector has revealed that under the critical wind conditions investigated, the slope error exceeds the target values usually given for heliostats. The dynamic loads have shown a significant contribution to the slope error.

8. Response prediction

The time-dependent deflection of a structure subjected to a transient load is referred to as response. It is characterized here by the vertical displacements r_{zi} at a specific location (i) in the structure. In order to predict the response of the structure and the time-dependent reaction loads accurately, simulations that use high temporal and spatial resolutions, as presented above, are required. However, a statistical treatment of the problem leads to simplified procedures that can be used to predict the relevant quantities for design purposes, such as loads and displacements, at a negligible computational effort.

In the case of wind loads on heliostats, turbulence in the atmospheric boundary layer is the main source of the fluctuating loads that lead to oscillations of the structure. Since turbulence is a stochastic process, the quantities involved in the analysis of the structural response are random in nature. This can be observed in the time histories displayed in Fig. 8.1, which show the streamwise velocity u at $z = h$ and the moment coefficient C_{my}, both obtained from the CFD simulation for the case $\alpha = 5°$, besides the vertical displacement r_{z1} from the dynamic FEM simulation evaluated above.

Despite the randomness of the quantities shown below, they can be characterized by their probability density functions. Since they follow a normal distribution, as shown in Fig. 8.2, they can be described by the mean and standard deviation. This practical property and the formulation of relationships between the quantities in the frequency domain via the admittance method (see Sect. 2.1.2) enables the prediction of peak values and the generation of synthetic time signals for further analysis as will be shown in this chapter. The effects of self-induced pressure fluctuations caused by vortex shedding are not explicitly modeled in the response prediction. However, their contribution on the fluctuating loads is contained in the frequency dependent transfer functions determined in the procedure.

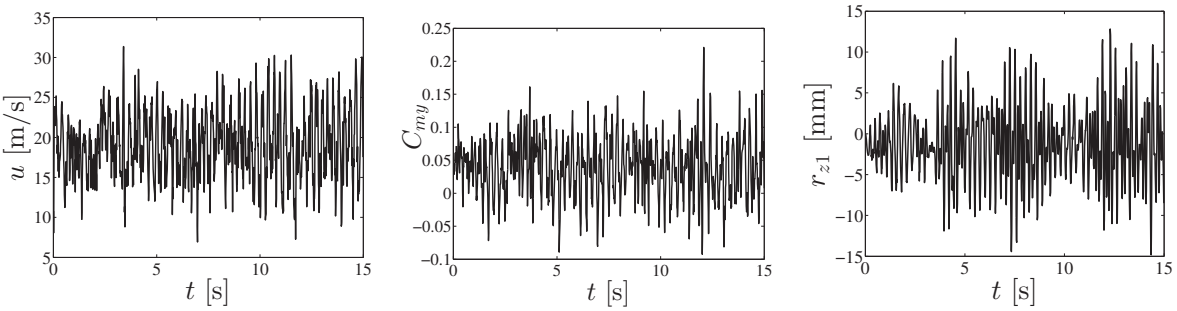

Figure 8.1.: Time histories of velocity u, moment coefficient C_{my} and displacement r_{z1}.

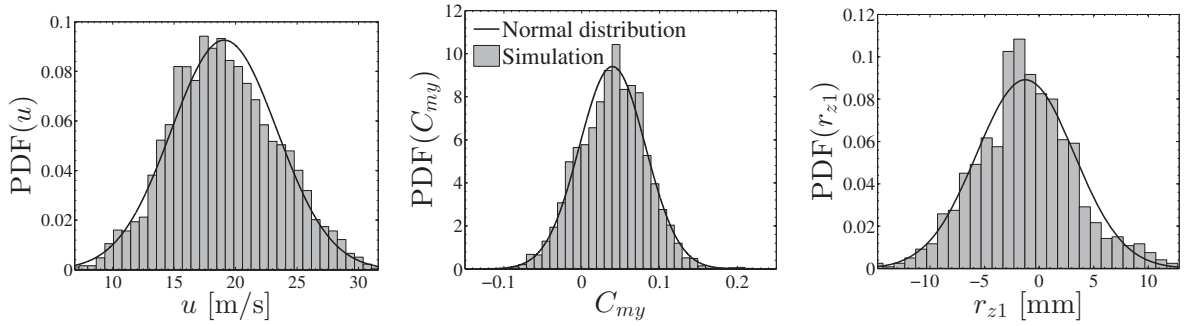

Figure 8.2.: Probability density functions of velocity, moment coefficient and displacement.

8.1. Peak values

The peak value $\hat{a}$ of a normally distributed quantity can be estimated as follows:

$$\hat{a} = \overline{a} + k_a \sigma_a, \tag{8.1}$$

where $\overline{a}$ and σ_a are the mean and standard deviation, respectively. The peak factor k_a is typically in the range between 3 and 5, covering more than 99% of the expected values of a normal distribution. For the quantities displayed in Fig. 8.1, the peak factors $k_u = 2.9$, $k_{C_{my}} = 4.9$ and $k_{r_{z1}} = 3.1$ are found. The following equation is proposed in [98] to estimate the peak factor of a random function:

$$k_a = \sqrt{2\ln(fT)} + \frac{\gamma}{\sqrt{2\ln(fT)}}, \tag{8.2}$$

where $\gamma = 0.577$ is Euler's constant, T is the period of observation and f is a characteristic cycling rate of the process. For the prediction of the maximal displacement in a vibrating structure, f is close to the natural frequency [24]. For a period $T = 15\,\mathrm{s}$ equal to the length of the time signals obtained above and using the natural frequency $f_{n3} = 4.7\,\mathrm{Hz}$ of mode 3 as characteristic cycling rate, the peak factor $k_{r_{z1}} = 3.1$ is obtained from Eq. (8.2) which matches the actual value presented above. Furthermore, this approximation can be used to calculate the peak factor for longer periods typically taken in wind load analysis, e.g., $T = 600\,\mathrm{s}$ (see Sect. 2.2.2), yielding a peak factor $k_{r_{z1}} = 4.1$.

8.2. Power spectral density and standard deviation

The calculation of peak values using Eq. (8.1) requires the mean and standard deviation of the quantity of interest. While the mean values can be, at least approximately, computed from steady-state CFD and static FE simulations, the standard deviation implies a transient analysis which is computationally more expensive. Alternatively, relationships to compute the standard deviations can be derived by means of spectral analysis.

The admittance method described in Sect. 2.1.2 is adopted here built upon the simulation results. This method is widely used in the investigation of unsteady loading of structures associated to buffeting. The following equations are derived similarly to the buffeting forces on suspension bridges [99]. The idea is to relate the velocity fluctuations, viewed as the input signal, to the loads and finally to the displacement, that represents the output signal. This assumes that the system behaves linearly, i.e., the loads are proportional to the velocity and the displacements are proportional to the loads.

The time-dependent variables are treated by Reynolds' approach as superposition of the fluctuating component and mean value. In a horizontally homogeneous flow, i.e., a constant mean wind speed and direction, the velocity vector reads:

$$\vec{U} = \begin{pmatrix} \overline{u} + u' \\ v' \\ w' \end{pmatrix}. \tag{8.3}$$

The moment $M_y(t)$ is calculated from Eq. (2.1b) using the square magnitude of the velocity vector and neglecting the square values of the fluctuations, which are small compared to the mean velocity, as follows:

$$M_y(t) = \frac{1}{2}\,\rho\,A\,c\,\overline{u}^2\left(1 + \frac{2}{\overline{u}}u'\right)C_{my}(\alpha). \tag{8.4}$$

The moment coefficient about the elevation axis C_{my} depends on the angle of attack or elevation angle α and can be approximated using the Taylor expansion evaluated at the mean elevation angle α_0 by ignoring the square terms as:

$$C_{my}(\alpha) = \overline{C}_{my} + \frac{\partial C_{my}}{\partial \alpha}(\alpha(t) - \alpha_0), \tag{8.5}$$

where the partial derivative is determined from the mean values of the moment coefficient at different elevation angles presented in Tab. 6.5. The instantaneous angle of attack $\alpha(t)$ depends on the angle of the velocity vector φ and the mean elevation angle α_0 (see Fig. 8.3) as:

$$\alpha(t) = \varphi(t) + \alpha_0. \tag{8.6}$$

For $\overline{u} \gg u', w'$ and using the small-angle approximation follows:

$$\tan(\varphi) \approx \frac{w'}{\overline{u}} \approx \varphi. \tag{8.7}$$

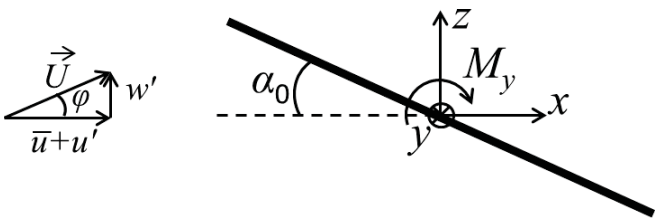

Figure 8.3.: Sketch of the response model for C_{my}.

Assuming that the products of the velocity fluctuations are negligible with respect to the square of the mean velocity [19], substituting Eq. (8.5), (8.6) and (8.7) in Eq. (8.4) and dividing by $\frac{1}{2}\,\rho\,A\,c\,\overline{u}^2$ yields:

$$C_{my}(t) = \overline{C}_{my} + \underbrace{\frac{2\,\overline{C}_{my}}{\overline{u}}u' + \frac{\partial C_{my}}{\partial \alpha}\frac{w'}{\overline{u}}}_{C'_{my}}. \tag{8.8}$$

The fluctuating part of the moment coefficient C'_{my} is transformed into the frequency domain by applying Eq. (E.4b) and a frequency-dependent function $|\chi_{aero,C_{my}}(f)|^2$, termed *aerodynamic admittance*, is introduced in order to obtain Eq. (8.9). This quantity takes into account the spatial characteristics of turbulence and its distribution over the body [20]. It represents a modifying adjustment (for an actual body) of the ideal case of a body surrounded by turbulence with full spatial correlation [19]:

$$S_{C_{my}}(f) = \frac{1}{\overline{u}^2}\left[4\,\overline{C}^2_{my}S_u(f) + \left(\frac{\partial C_{my}}{\partial \alpha}\right)^2 S_w(f)\right]|\chi_{aero,C_{my}}(f)|^2. \tag{8.9}$$

A linear relationship between the fluctuating load and displacement is achieved by modeling the plate as a rigid body that oscillates around the y-axis. The torsional moment is defined by:

$$M_y(t) = \frac{1}{2}\,\rho\,A\,c\,\overline{u}^2 C_{my}(t) = k_y\delta_y(t), \tag{8.10}$$

where k_y represents the rotational stiffness of the system and δ_y the time-dependent angle of rotation about y as illustrated in Fig. 8.4, where the dotted line represents the twisted plate. Assuming that the axis of rotation is fixed (i.e., deflections of the pylon that supports the drives and mirror frame are neglected) and for small oscillations around y, the rotation angle and the vertical displacement r_{z1} are related as follows:

$$\tan(\delta_y) = \frac{2\,r_{z1}}{c} \approx \delta_y. \tag{8.11}$$

By substituting Eq. (8.11) in Eq. (8.10) and adopting the separation of mean and fluctuating components given by Eq. (8.8), the time-dependent vertical displacement yields:

$$r_{z1}(t) = \frac{\rho\,A\,c^2\,\overline{u}^2}{4\,k_y}\left(\overline{C}_{my} + C'_{my}\right). \tag{8.12}$$

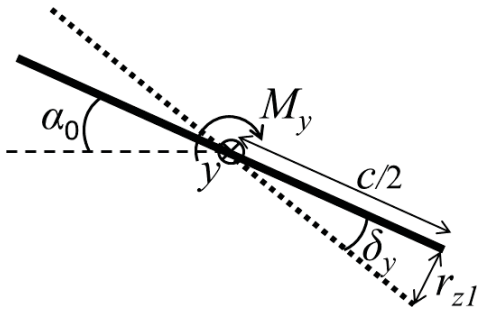

Figure 8.4.: Sketch of the response model for r_{z1}.

The first product on the right-hand side of Eq. (8.12) represents the mean vertical displacement $\overline{r}_{z1}$ and the second product the fluctuating part r'_{z1} that can be expressed in the following form:

$$r'_{z1} = \frac{\overline{r}_{z1}}{\overline{C}_{my}} C'_{my}. \tag{8.13}$$

Equation (8.13) is then transformed into the frequency domain and the frequency-dependent function $|\chi_{mech,r_{z1}}(f)|^2$, termed *mechanical admittance*, is introduced:

$$S_{r_{z1}}(f) = \left(\frac{\overline{r}_{z1}}{\overline{C}_{my}}\right)^2 S_{C_{my}}(f)|\chi_{mech,r_{z1}}(f)|^2. \tag{8.14}$$

The mechanical admittance represents the relationship of the fluctuating load (C'_{my}) to the response (r'_{z1}) of the structure in the frequency domain. Its shape is dictated by the natural frequencies, hence it is described in [20] as the square of the resonance curve.

For the moment and oscillations around the tangential axis x_t a similar derivation as above is conducted on the $y-z_n$ plane normal to the mirror frame as displayed in Fig. 8.5 and 8.6. The direction of the velocity vector on this plane is described by the angle of attack β defined by:

$$\beta = \arctan\left(\frac{v'}{w_n}\right), \tag{8.15}$$

where the normal velocity component is defined by $w_n = \sin(\alpha_0)(\overline{u}+u')+\cos(\alpha_0)w'$. The moment $M_x(t)$ is calculated by Eq. (2.1b) using the square magnitude of the velocity vector and neglecting the square values of the fluctuations. Hence, it follows:

$$M_x(t) = \frac{1}{2}\,\rho\, A\, c\, \overline{u}^2 \left(1 + \frac{2}{\overline{u}}u' + \frac{2}{\overline{u}}\cot(\alpha_0)w'\right) C_{mx}(\beta). \tag{8.16}$$

A relationship between the angle of attack and the moment coefficient is derived from the linear terms of the Taylor expansion of C_{mx} evaluated at the mean angle β_0 as:

$$C_{mx}(\beta) = \overline{C}_{mx} + \frac{\partial C_{mx}}{\partial \beta}(\beta(t) - \beta_0). \tag{8.17}$$

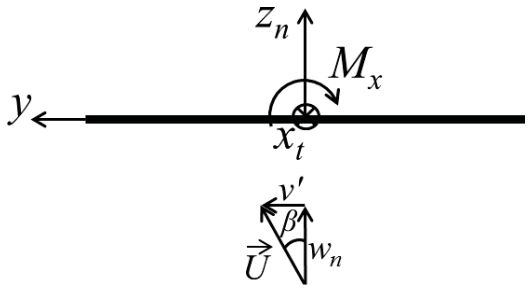

Figure 8.5.: Sketch of the response model for C_{mx}.

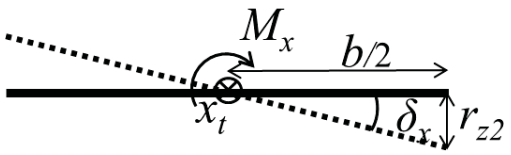

Figure 8.6.: Sketch of the response model for r_{z2}.

Substituting Eq. (8.17) in Eq. (8.16) and dividing by $\frac{1}{2}\,\rho\,A\,c\,\overline{u}^2$ yields:

$$C_{mx}(t) = \overline{C}_{mx} + \underbrace{\frac{2\,\overline{C}_{mx}}{\overline{u}}(u' + \cot(\alpha_0)w') + \frac{\partial C_{mx}}{\partial \beta}\left(\beta' + \frac{2}{\overline{u}}\beta' u' + \frac{2}{\overline{u}}\cot(\alpha_0)\beta' w'\right)}_{C'_{mx}}. \quad (8.18)$$

After transformation into the frequency domain of the fluctuating part of the moment coefficient from Eq. (8.18) and the introduction of the aerodynamic admittance function $|\chi_{aero,C_{mx}}(f)|^2$, one obtains:

$$\begin{aligned} S_{C_{mx}}(f) = \Bigg[&\left(\frac{2\,\overline{C}_{mx}}{\overline{u}}\right)^2 \left(S_u(f) + \cot^2(\alpha_0) S_w(f)\right) + \\ &\left(\frac{\partial C_{mx}}{\partial \beta}\right)^2 \left(S_\beta(f) + \frac{4}{\overline{u}^2}\left(S_{\beta u}(f) + \cot^2(\alpha_0) S_{\beta w}(f)\right)\right)\Bigg] |\chi_{aero,C_{mx}}(f)|^2. \end{aligned} \quad (8.19)$$

A linear relationship between the moment coefficient C_{mx} and the vertical displacement r_{z2} is derived from the model displayed in Fig. 8.6 that represents a rigid plate that oscillates around the x_t-axis. Its torsional moment is given by:

$$M_x(t) = \frac{1}{2}\,\rho\,A\,b\,\overline{u}^2 C_{mx}(t) = k_x \delta_x(t), \quad (8.20)$$

where δ_x is the time-dependent angle of rotation around x_t and k_x represents the rotational stiffness that can be determined from static FE simulations. Applying the small-angle approximation, one obtains:

$$\tan(\delta_x) = \frac{2\,r_{z2}}{b} \approx \delta_x. \quad (8.21)$$

After substitution of Eq. (8.21) in Eq. (8.20) and using the separation of mean and fluctuating components of the moment coefficient, the vertical displacement yields:

$$r_{z2}(t) = \frac{\rho\,A\,b^2\,\overline{u}^2}{4\,k_x}\left(\overline{C}_{mx} + C'_{mx}\right). \quad (8.22)$$

The second term on the right-hand side of Eq. (8.22) is transformed into the frequency domain to obtain the following equation by introducing the mechanical admittance function $|\chi_{mech,r_{z2}}(f)|^2$:

$$S_{r_{z2}}(f) = \left(\frac{\rho\,A\,b^2\,\overline{u}^2}{4\,k_x}\right)^2 S_{C_{mx}}(f)|\chi_{mech,r_{z2}}(f)|^2. \quad (8.23)$$

The admittance functions can be computed from the equations where they have been introduced (Eq. (8.9), (8.14), (8.19) and (8.23)) provided that all other quantities are known. The flow simulation results provide the necessary information to compute the aerodynamic admittance functions and, in combination with the dynamic simulation results, the mechanical admittance functions.

Figure 8.7 shows the admittance functions calculated from the simulation results for $\alpha = 5°$. The aerodynamic admittance functions present the largest values at low frequencies and, for $f\,c/\overline{u} > 1$, decrease with increasing frequency. This is due to the fact that towards low frequencies the ratio of the wavelength of the turbulent fluctuations to the size of the body increases and the response approaches a quasi-steady behavior, i.e., the velocity and load fluctuations approach full correlation (see Sect. 2.1.2). At higher frequencies the smaller turbulent eddies have shorter wavelengths; thus those eddies with higher frequencies will suffer a loss of coherence more rapidly than the large eddies [19]. Consequently, the small eddies do not have a strong impact on the structure. A similar behavior is reproduced by wind tunnel tests on bridge sections in [100–102]. A pronounced peak in the aerodynamic admittance functions, as can be present in cases where vortex shedding takes place [103], is not observed here which confirms the dominant role of atmospheric turbulence mentioned before.

In [103, 104] it is shown that for a given body shape $|\chi_{aero}(f)|^2$ is a function of the body size and wind speed. By formulating the aerodynamic admittances as a function of the non-dimensional frequency $(f \cdot c/\overline{u})$ they can be used for similar heliostats of different size and for different wind speeds. To compute the spectral distribution of the moments, equations (8.9) and (8.19) are used with mean quantities that are already known (e.g., $\overline{C}_{my}, \frac{\partial C_{my}}{\partial \alpha}, \frac{\partial C_{mx}}{\partial \beta}$) for a given wind direction. Spectral information of the velocity (i.e., $S_u, S_w, S_\beta, S_{\beta u}, S_{\beta w}$) is also required to prescribe the turbulence conditions. These spectra can be obtained from wind data analysis or, alternatively, S_u and S_w can be modeled by the spectra given by Eq. (2.12) and (2.14).

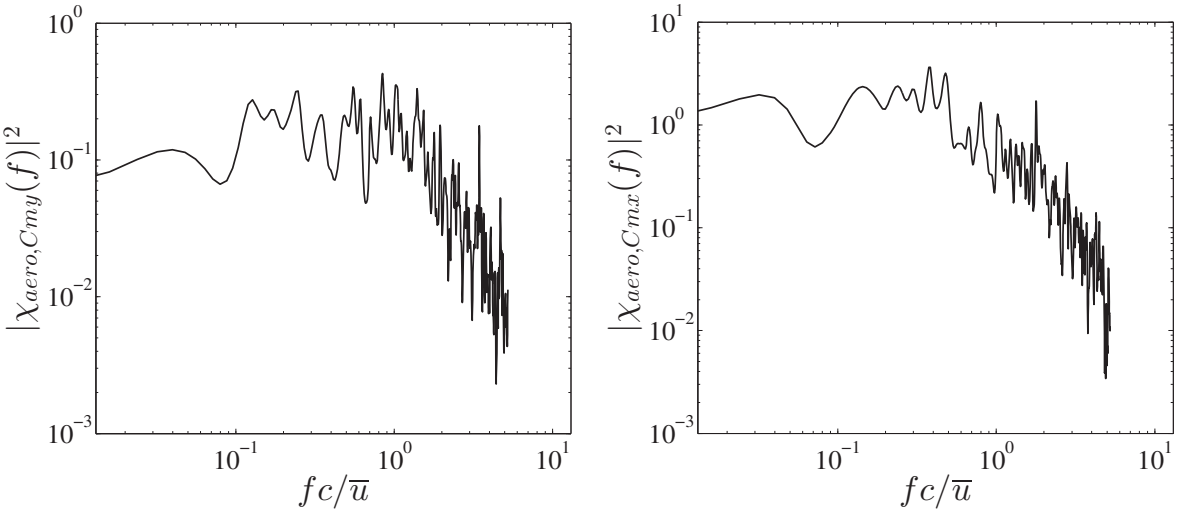

Figure 8.7.: Aerodynamic admittance functions for $\alpha = 5°$.

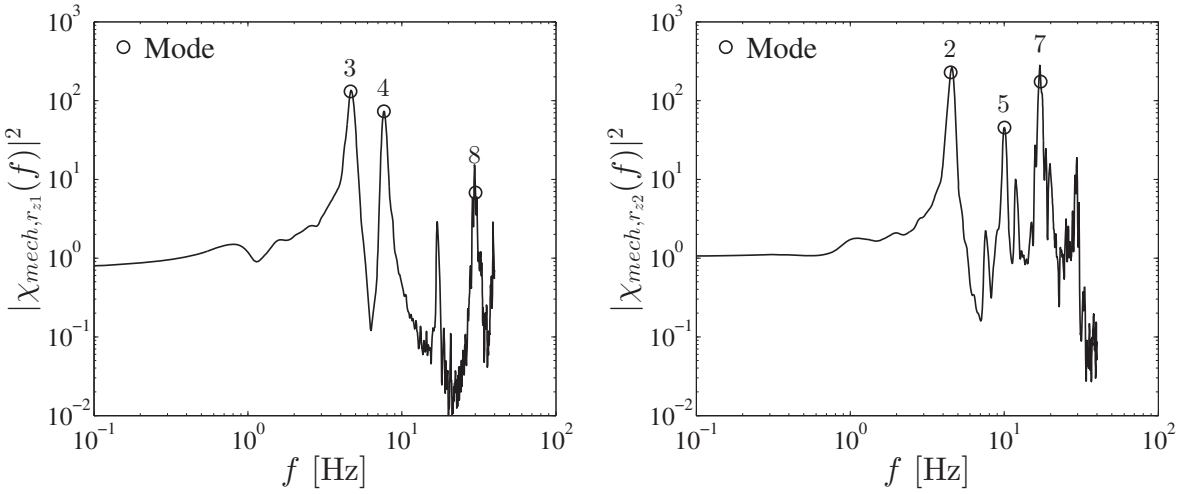

Figure 8.8.: Mechanical admittance functions for $\alpha = 5°$.

The mechanical admittance functions presented in Fig. 8.8 exhibit several distinctive peaks (resonant peaks) located at the natural frequencies of the modes that are most affected by the excitation of the structure in a specific direction. For $|\chi_{mech,r_{z1}}(f)|^2$, which relates the vertical displacement r_{z1} to the moment coefficient C_{my}, the modes associated with oscillations around the y-axis are distinguishable, whereas for $|\chi_{mech,r_{z2}}(f)|^2$, which relates the vertical displacement r_{z2} to the moment coefficient C_{mx}, the modes associated with oscillations around the x_t-axis are the distinctive modes. This is in accordance with the characteristic modes associated in Sect. 5.4.1 and Sect. 7.2 with oscillations around the axes x_t and y and their corresponding moments. Equations (8.14) and (8.23) can be used to compute the spectral distribution of the displacements by using mean quantities that can be calculated from linear relationships (e.g., $\overline{r}_{z1}$ from Eq. (8.10)) or from static FE simulations for a given wind speed.

The aerodynamic admittance functions are usually assumed to be independent of the turbulence intensity. This subject was studied in [105] by wind tunnel measurements on bridge deck sections, and the results did not show any noticeable changes in the aerodynamic admittance when increasing I_u from 6.8% to 9.1%. Nonetheless, it must be noted that the linear relationship between the fluctuating wind and the fluctuating loads described by the aerodynamic admittance functions does not hold for arbitrary turbulence conditions. Due to neglecting the square terms of the velocity fluctuations an error is introduced which increases with the turbulence intensity. However, for most wind engineering problems the error is small, e.g., for $I_u = 20\,\%$ the error is only 4% [103].

The PSD of the reaction moment $S_{M_{y,out}}$ can be calculated from this procedure by:

$$S_{M_{y,out}} = |H_{M_y}(f)|^2 S_{M_{y,in}} = |H_{M_y}(f)|^2 \left(\frac{1}{2}\,\rho\,\overline{u}^2\,A\,c\right)^2 S_{C_{my}}(f), \tag{8.24}$$

where $|H_{M_y}(f)|^2$ is the FRF determined from dynamic simulations by Eq. (7.4).

As mentioned before, the quantities of interest are random in nature and can only be described statistically. Their variance can be integrated from the PSDs by:

$$\sigma^2_{C_{mx}} = \int_0^{f_s/2} S_{C_{mx}} df, \quad \sigma^2_{C_{my}} = \int_0^{f_s/2} S_{C_{my}} df, \quad \sigma^2_{M_{y,out}} = \int_0^{f_s/2} S_{M_{y,out}} df, \tag{8.25a}$$

$$\sigma^2_{r_{z1}} = \int_0^{f_s/2} S_{r_{z1}} df, \qquad \sigma^2_{r_{z2}} = \int_0^{f_s/2} S_{r_{z2}} df, \tag{8.25b}$$

where f_s is the sampling frequency. The square root of the variance, i.e., the standard deviation, can then be used to estimate maximal values from mean quantities using Eq. (8.1).

The procedure to estimate the statistical values of the output moment from the set of equations presented above is summarized in the following steps:

1. Define the reference wind speed U at $z = 10\,\mathrm{m}$ or estimate it from wind data
2. Define the surface roughness height z_0 for a given terrain
3. Calculate the mean wind speed $\overline{u}$ at $z = h$ from Eq. (2.5)
4. Compute S_u and S_w from wind data or Eq. (2.12) and (2.14)
5. Determine $\overline{C}_{my}$, $\frac{\partial C_{my}}{\partial \alpha}$, $|\chi_{aero,C_{my}}(f)|^2$ and $|H_{M_y}(f)|^2$ from simulations
6. Calculate the mean value $\overline{M}_{y,out}$ from Eq. (2.1b)
7. Compute $S_{C_{my}}(f)$ from Eq. (8.9)
8. Compute $S_{M_{y,out}}$ from Eq. (8.24)
9. Calculate the standard deviation $\sigma_{M_{y,out}}$ from Eq. (8.25a)
10. Estimate the peak value $\hat{M}_{y,out}$ from Eq. (8.1) using a peak factor $3 < k_M < 5$

Two specific operating conditions that are of special interest for the structural design were selected to compute the output moment following the procedure described above. The reference wind speed $U = 40\,\mathrm{m/s}$ was applied to the case $\alpha = 5°$ approximating thereby storm conditions. For $\alpha = 20°$ the maximal operating wind speed $U = 10\,\mathrm{m/s}$ was specified to represent critical conditions during power generation. The velocity spectra S_u and S_w were computed from the empirical formulas given in Eq. (2.12) and (2.14) for a roughness height $z_0 = 8\,\mathrm{cm}$[1] corresponding to the turbulence characteristics of the wind data analyzed in Sect. 4.3.2. The required quantities in step 5 of the procedure were taken from the simulations for the corresponding elevation angle. The peak values $\hat{M}_{y,out}$ were computed from Eq. (8.1) using the peak factors given in Tab. 7.1 for the corresponding case. The statistical results are presented in Tab. 8.1. The peak values can be used to evaluate the design against structural failure due to overstressing by estimating maximal stresses on critical parts, e.g., the shaft of the elevation drive.

[1]The selection of this values instead of the reference value $z_0 = 4\,\mathrm{cm}$ used for the CFD simulations is done under the assumption that the aerodynamic admittance functions are independent of the turbulence intensity as discussed above.

α [°]	U [m/s]	$\overline{M}_{y,out}$ [Nm]	$\sigma_{M_{y,out}}$ [Nm]	$\hat{M}_{y,out}$ [Nm]
5	40	430	725	3076
20	10	116	45	252

Table 8.1.: Statistics of reaction moment for different operating conditions.

8.3. Synthetic signals

In order to evaluate structural failure due to fatigue, time signals of the loads are required. They can be recovered from the frequency components by means of *Fourier synthesis* which is the opposite process of the *Fourier analysis*. When dealing with discrete signals the operation known as *Inverse Discrete Fourier Transform* IDFT is used. Applied to the fluctuating part of the reaction moment, the transformation reads:

$$M'_{y,out}[k] = \frac{1}{N} \sum_{n=0}^{N-1} \breve{M}[n]\, e^{i2\pi nk/N}, \tag{8.26}$$

where k is the index of the time samples and n and N are the index and total number of the frequency samples, respectively. $\breve{M}$ are the complex Fourier coefficients that contain the magnitude and phase information of the individual terms of the sum called *harmonics* [106]. Even though the PSD only contains information about the magnitude of the harmonics, it is possible to synthesize the signals from the spectrum by assuming a normally distributed random phase $\phi \in \{0, ..., 2\pi\}$ and computing the complex Fourier coefficients from:

$$\breve{M}[n] = \left(S_{M_{y,out}}[n]\, F_s/2\right)^{1/2} e^{i\phi[n]}. \tag{8.27}$$

Time signals of the reaction moment were generated artificially using this procedure after computing the PSD from Eq. (8.24) for the operating conditions described in Tab. 8.1. The synthetic time signals and their corresponding PDFs are plotted in Fig. 8.9. Similar to the simulation results displayed in Fig. 7.8, it can be observed that the synthetic signals are characterized by random fluctuations that follow a normal distribution. These signals can be used to perform fatigue analysis by converting them into equivalent stresses on elements of the elevation drive and then applying the method described in Sect. 2.1.3.

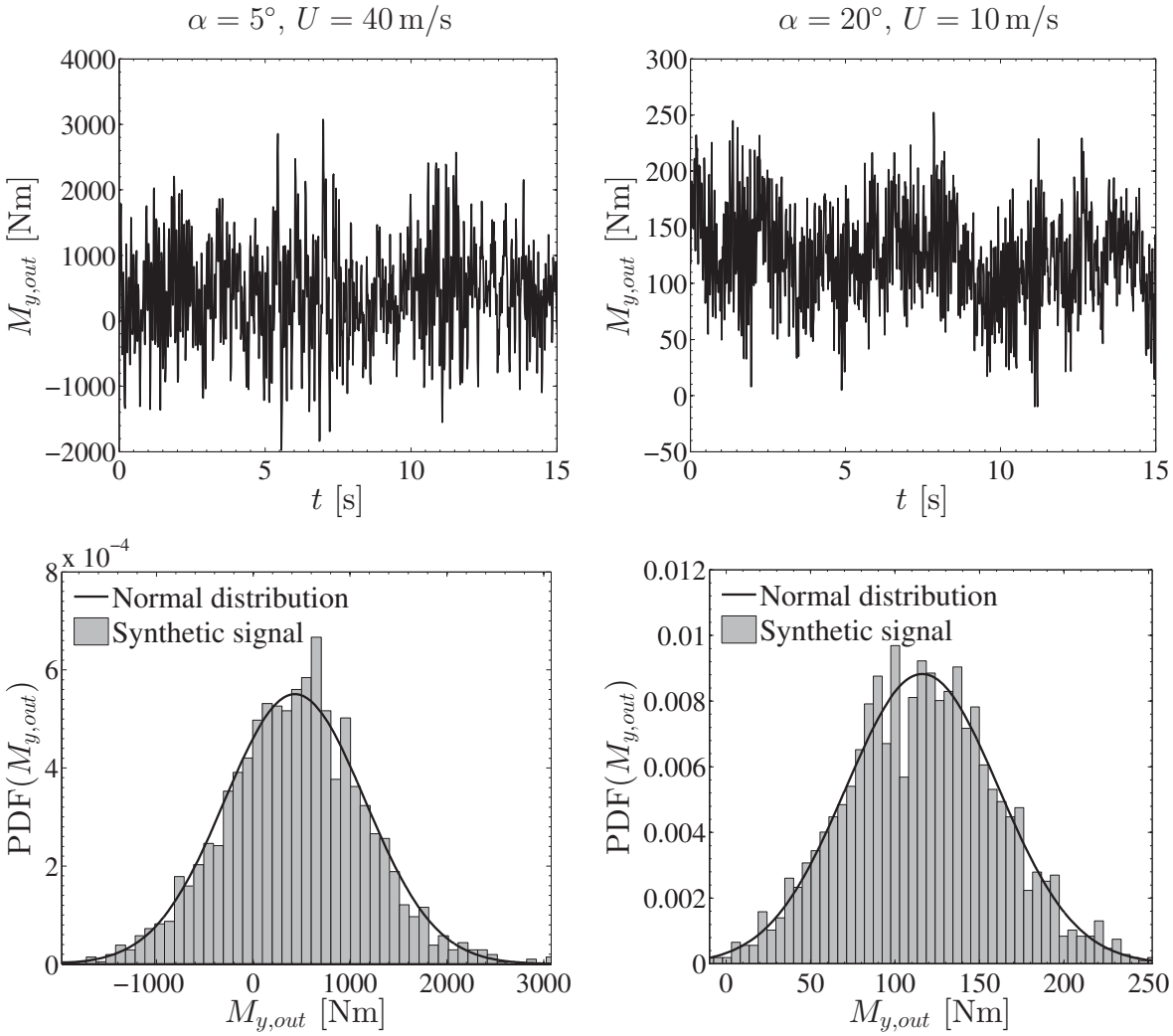

Figure 8.9.: Synthetic time signals and probability density functions of the reaction moment for different operating conditions.

8.4. Distribution of the angle deviation

The non-central χ-distribution with unequal variances derived in [107] describes the distribution of the magnitude, or *Euclidean norm*, of a 2D vector with normally distributed components. By modeling the mirror frame as a rigid body with two DOFs, namely the rotation around x_t and y axes, and assuming small deformations, it can be shown that the angle deviation of the surface normal vector is:

$$\delta = \sqrt{{\delta_x}^2 + {\delta_y}^2}, \tag{8.28}$$

where δ_x and δ_y are the angle deviations defined by Eq. (8.21) and (8.11) which can be viewed as the components of the 2D vector δ. Since they are proportional to the normal displacements, they are also normally distributed. Using their mean values $\overline{\delta}_x$, $\overline{\delta}_y$ and

standard deviations σ_{δ_x}, σ_{δ_y} as parameters, the χ-distribution of δ reads:

$$\mathrm{PDF}(\delta) = \frac{\delta}{2\pi\sigma_{\delta_x}\sigma_{\delta_y}} \int_0^{\pi/2} \left[e^{\frac{-(\delta\sin(\theta)-\overline{\delta}_x)^2}{2\sigma^2_{\delta_x}}} + e^{\frac{-(\delta\sin(\theta)+\overline{\delta}_x)^2}{2\sigma^2_{\delta_x}}} \right] \left[e^{\frac{-(\delta\sin(\theta)-\overline{\delta}_y)^2}{2\sigma^2_{\delta_y}}} + e^{\frac{-(\delta\sin(\theta)+\overline{\delta}_y)^2}{2\sigma^2_{\delta_y}}} \right] d\theta. \tag{8.29}$$

Equation (8.29) was numerically integrated over θ to compute the PDF of δ displayed in Fig. 7.10. Thereby the required parameters were derived from the dynamic simulation results and it was shown that this approximation fits very well the actual distribution. These parameters can also be determined by the method presented in Sect. 8.2 for given wind conditions. For this purpose, high resolution wind data is required to resolve the relevant part of the spectrum which comprises, on the high frequency end, the natural frequency of the highest mode of the structure that has a significant contribution to δ and, on the low frequency end, the slowest rates of variations in wind speed within the micro-meteorological range (see Sect. 2.2.2).

The following steps are followed to compute the distribution of δ:

1. Compute mean wind speed $\overline{u}$ and velocity spectra S_u, S_w from wind data
2. Determine $\overline{r}_{z1}, \overline{C}_{my}, \frac{\partial C_{my}}{\partial\alpha}, |\chi_{aero,C_{my}}(f)|^2$ and $|\chi_{mech,r_{z1}}(f)|^2$ from simulations
3. Compute the spectrum of vertical displacement $S_{r_{z1}}$ from Eq. (8.14)
4. Calculate $\sigma_{r_{z1}}$ from Eq. (8.25b)
5. Calculate the statistics of δ_y from $\overline{\delta}_y = 2\,\overline{r}_{z1}/c$ and $\sigma_{\delta_y} = 2\,\sigma_{r_{z1}}/c$
6. Compute $\beta, S_\beta, S_{\beta u}$ and $S_{\beta w}$ from wind data
7. Determine $k_x, \frac{\partial C_{mx}}{\partial\beta}, |\chi_{aero,C_{mx}}(f)|^2$ and $|\chi_{mech,r_{z2}}(f)|^2$ from simulations[2]
8. Compute the spectrum of vertical displacement $S_{r_{z2}}$ from Eq. (8.23)
9. Compute $\sigma_{r_{z2}}$ from Eq. (8.25b)
10. Calculate the standard deviation of δ_x from $\sigma_{\delta_x} = 2\,\sigma_{r_{z2}}/b$
11. Estimate the distribution of δ from Eq. (8.29)[2]

A wind measurement with the highest average wind speed found in the data, namely 7.9 m/s, was selected to predict the angle deviation under real conditions for the case $\alpha = 20°$. The data was sampled at 20 Hz for a period of 10 min. Such a wind data block satisfies the requirements mentioned above as it contains both, the low frequency end of the micro-meteorological range found at about 1 cycle/5 min (see Fig. 2.2) and the high frequency end given by the natural frequency $f_n = 9.9$ Hz of mode 5 identified as the highest oscillation about the principal axes of the mirror frame. Time signals of the velocity components and the corresponding spectral quantities required in the procedure are displayed in Fig. 8.10.

[2]For $\beta_0 = 0$, i.e., the mean wind direction is perpendicular to the leading edge, the parameters $\overline{C}_{mx} = \overline{\delta}_x = 0$ due to symmetry conditions around the x_t-axis..

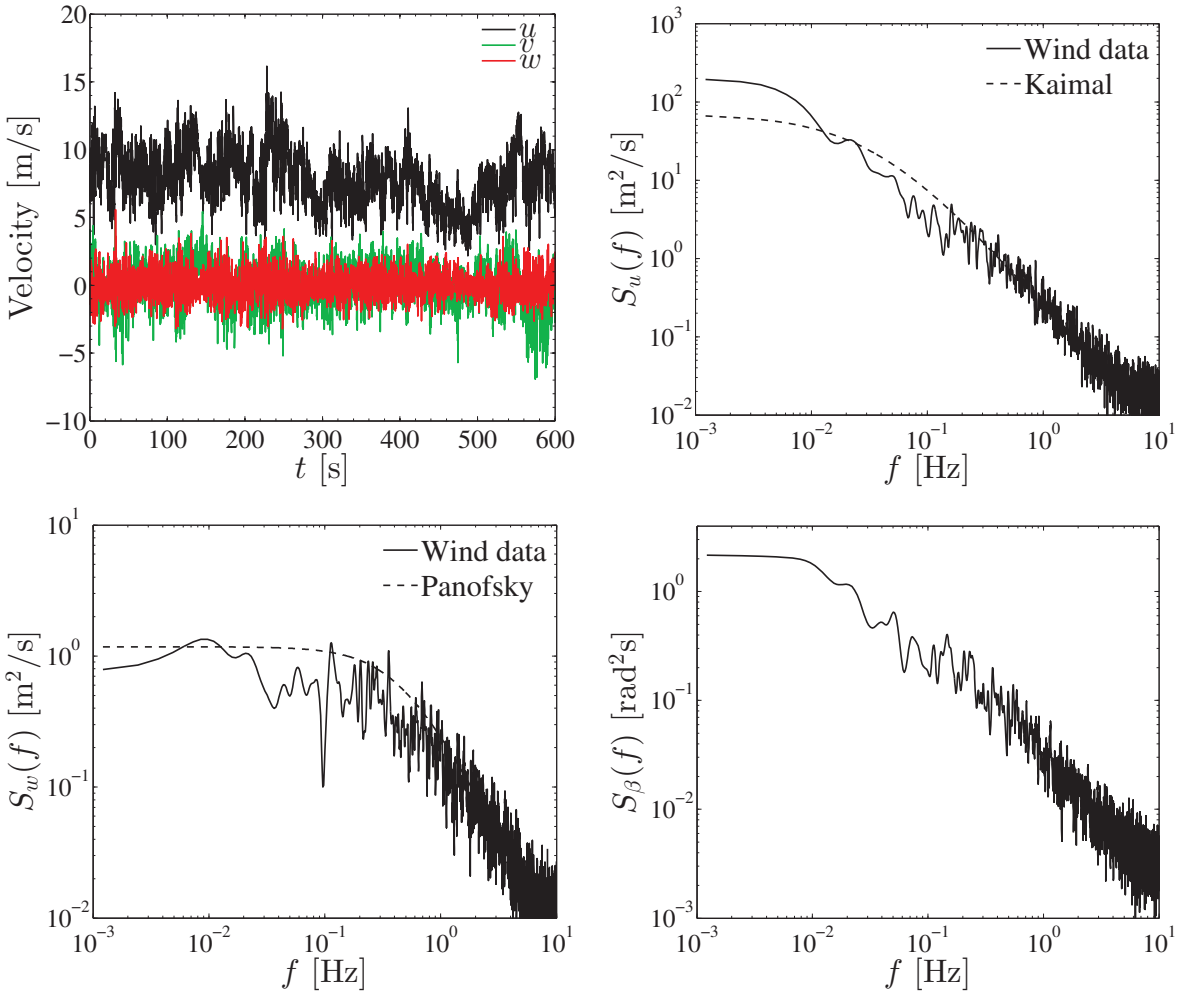

Figure 8.10.: Input signals of velocity.

The distribution of δ, based on the velocity signals presented above, is displayed in Fig. 8.11. Its main statistical quantities are determined by numerical integration of the following equations:

$$\overline{\delta} = \int_0^\infty \delta \cdot \mathrm{PDF}(\delta) d\delta \qquad \text{and} \qquad \sigma_\delta^2 = \int_0^\infty (\delta - \overline{\delta})^2 \cdot \mathrm{PDF}(\delta) d\delta. \tag{8.30}$$

The RMS value is computed from the mean ($\overline{\delta}$) and variance (σ_δ^2) by Eq. (7.5). The statistical values of the angle deviation and its individual components are given in Tab. 8.2. The slope error, described by the RMS value of δ, is close to the range of 1-2 mrad found in [15]. It can be noticed that the statistics of δ_y are close to the values of the total angle deviation δ. Here, as well as in the dynamic simulations, the difference between the RMS values is less than 7%. The large contribution of δ_y reproduces the dominant presence of the oscillations around the y-axis observed in Sect. 7.2 and indicates that the slope error can be approximated solely by the RMS of δ_y.

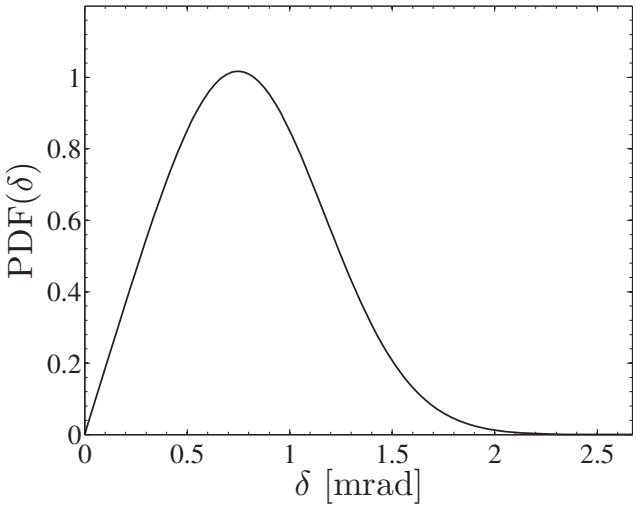

Figure 8.11.: χ-distribution of angle deviation.

	Mean	Std.	RMS
δ_x	0.00	0.30	0.30
δ_y	0.72	0.43	0.83
δ	0.81	0.37	0.89

Table 8.2.: Statistics of angle deviation in [mrad].

If the contribution of δ_x is neglected, the procedure presented above can be reduced to the first 5 steps. Thereby, only the velocity spectra S_u and S_w are required to estimate the slope error. These spectra can be determined from Eq. (2.12) and (2.14) instead of wind data as demonstrated in Fig. 8.10 and 4.7. Furthermore, neglecting the contribution of δ_x enables the prediction of a yearly averaged slope error $\overline{\mathrm{RMS}(\delta_y)}$ by computing a weighted average as:

$$\overline{\mathrm{RMS}(\delta_y)} = \int_0^\infty \mathrm{RMS}(\delta_y(U)) \cdot \mathrm{PDF}(U) dU, \tag{8.31}$$

where $\mathrm{RMS}(\delta_y(U))$ is the root-mean-square angle deviation for individual wind speeds U with a probability distribution given by $\mathrm{PDF}(U)$. To estimate the slope error during power generation, the $\mathrm{PDF}(U)$ shown in Fig. 4.3(b) was used. After computing the slope error for each individual wind speed of the distribution, Eq. (8.31) was integrated numerically to obtain a yearly averaged value of 0.20 mrad. This value is clearly below the recommended value of 1 mrad given in [14] for a cost-effective heliostat and suggests that the structural design can be further optimized. However, it must be noted that the yearly averaged slope error was determined specifically for one elevation angle $\alpha = 20°$.

In order to obtain a more general conclusion about the optical efficiency, various elevation angles found during operation must be investigated. The wind induced slope

errors can be translated to a yearly averaged power loss using ray tracing codes. In [108] such calculations were performed for a large heliostat in combination with static FE simulations. In accordance with the present results, they found that the averaged wind-induced deflections were very small (<0.1 mrad) and that the effect on the annual yield was insignificant.

8.5. Conclusions from response prediction

A simplified method to describe statistically the loads and displacements of heliostat structures was derived in this section. The method uses admittance functions, determined previously from numerical simulations, to relate input and output quantities under arbitrary wind conditions. It was shown that the quantities involved in the procedure follow a Gaussian distribution. This practical property was used to predict maximal values and generate synthetic time signals of the moment under extreme wind conditions. Furthermore, it was demonstrated how to evaluate the optical error under realistic wind conditions and to predict a yearly averaged slope error by using wind data. For one specific operating point, the optical error was estimated and the value is small compared to recommendations found in the literature for a cost-effective design. Due to the negligible computational effort compared to numerical simulations, the method proposed here is very useful to investigate the optical efficiency and to provide the necessary information to perform fatigue analysis on heliostats.

9. Summary and Conclusions

A methodology for simulating dynamic wind loads on heliostats was proposed in the present work. It consists of different system components that were modeled separately and linked with others to finally provide time-dependent loads and deformations of the structure. The first step required the definition of boundary conditions. Since the methodology was applied to a heliostat unit located at the edge of a heliostat field, flow boundary conditions were described by the undisturbed ABL. By analyzing different wind data sets collected by DLR's Institute of Solar Research at the Plataforma Solar de Almeria (PSA) located at a representative solar site in south Spain it was shown that empirical formulas found in the literature can be used to describe the main statistical quantities of wind and define, therefore, the boundary conditions required for a CFD model. Even though the present investigation was limited to a particular wind condition, the wind data analysis at the PSA provided also information to examine different operational conditions that the heliostats are exposed to. For this purpose, a classification of the wind conditions was accomplished by evaluating the wind speed and wind direction from a whole year of data. Valuable information was derived from this analysis, such as the expected wind speed and direction and their corresponding probability, categorized by their magnitudes in different ranges. In addition, diurnal and nocturnal conditions were identified by the use of solar irradiance data. The analysis included turbulence quantities as well, such as turbulence intensities and spectral distributions. Together with the mean wind speed data, a full description of the wind conditions was achieved.

The development of the dynamic model consists basically of two steps: First the generation of a structural model that reproduces the dynamic behavior of the structure, and secondly the coupling of the model with realistic load data to predict the dynamic response. The first step was accomplished by means of modal analysis. A FE model of a full-scale heliostat was generated and its modal parameters were computed. Likewise, the reference heliostat structure was examined experimentally to validate the numerical results and to determine the damping properties of the structure. The agreement between simulations and experiments was satisfactory at all operating points investigated. Mode shapes more likely to be excited by fluctuating pressure loads were identified, besides potentially critical conditions caused by vortex shedding using the Strouhal numbers of inclined flat plates from experimental data found in the literature.

In order to provide realistic time-dependent load signals for the dynamic analysis, flow simulations were performed based on LES. Due to the high computational costs of the CFD simulations, a simplified heliostat model was applied that consisted of an inclined flat plate immersed in the ABL. To reproduce the ABL, synthetic turbulence was gen-

erated via the vortex method. By fitting the model parameters of the VM, the desired turbulent inflow conditions were obtained. By comparing with simulations without inflow turbulence, the importance of accounting for turbulence was shown, especially for the fluctuating load components. In the absence of experimental data to validate the simulations, the plausibility of the results was evaluated by comparing the findings with previous numerical and experimental investigations on flat plates. This included studies on the effects of free-stream turbulence and a benchmark test case of a high resolution LES simulation that was replicated with an excellent agreement. The computational time for one CFD simulation of the heliostat plate was approx. 10^4 CPU-h.

After performing CFD simulations, time signals of the pressure difference along the plate were translated to the FE model to perform dynamic simulations in a one-way coupled manner. The transient results confirmed that out-of-plane modes were principally affected by fluctuating wind loads. Particularly mode 3, which describes an oscillation about the elevation axis, had a dominating role and was responsible for the largest displacements at all operating points investigated. The maximal displacements were less than 1 % of the chord length and justified the application of one-way coupling between the CFD and FEM analysis that relies on small deformations. Even though only a few quantities were analyzed from the dynamic simulations, the results provide explicit information about the time-dependent reaction forces and moments at any location of interest for design purposes. The computational time for one FEM simulation of the heliostat structure was approx. 400 CPU-h.

Motivated by the high computational effort involved in the simulations, relationships to predict peak values and standard deviations of the quantities of interest, e.g., moments about the principal axes of the mirror frame and displacements in the normal direction of the mirror surface, were derived. The relationships, termed admittance functions, were obtained from the transient results in analogy to the prediction of buffeting vibrations in other wind engineering applications. The procedure enables the prediction of the response of the structure under arbitrary wind conditions by performing less expensive static simulations that provide the required mean values. These are then combined with the admittance functions to obtain the spectral distribution and standard deviation of the relevant quantities for the design. It was shown that the quantities involved in the procedure, namely velocities, loads and displacements, follow a normal distribution. This property enabled the estimation of peak values and the reconstruction of time signals of loads and displacements under extreme wind conditions. Furthermore, the method was applied using real wind data to estimate a yearly averaged optical error, which was small compared to reference values found in the literature.

Unlike previous numerical studies, the present work provides a comprehensive description of suitable numerical methods to analyse and predict dynamic wind loads and their effects on heliostats. Compared to experimental investigations in wind tunnels and at full scale, the dynamic simulation of a heliostat provides much more detailed information for the design, as dynamic loads can be evaluated at any part of interest in the structure. Even though the simulations performed in the present work are computation-

ally expensive, it was shown that a full-scale heliostat structure can still be examined at an acceptable computational effort. Furthermore, the practical procedure based on the admittance method proposed for the prediction of dynamic wind loads on heliostats represents a more suitable alternative to wind codes commonly used in civil engineering applications.

Increasing interest from the industry on the subject of dynamic wind loads on heliostats has facilitated further investigations currently under development at DLR Institute of Solar Research within two projects financed by the German Federal Ministry for Economic Affairs and Energy (BMWi). The methodology proposed in the present work to tackle this problem will be applied on commercially available heliostats as well as on novel heliostat designs. Numerical and experimental modal analysis have been performed recently as part of the project HelFer (0325458C) on a commercially available heliostat design with very satisfactory results regarding the agreement between simulations and experiments. Wind tunnel as well as full-scale measurements under real wind conditions are also part of the current project AutoR (0325629D) with the objective to provide validation data for the simulations. These investigations will also examine fatigue loading in order to predict the service life of specific components. In cases where fatigue loading turns out to be critical, measures to reduce dynamic wind loads, e.g., by using tuned mass dampers, can be developed using dynamic FE models. Further work is still necessary to examine dynamic wind loads on the units located inside the heliostat field. This requires larger models that include several heliostats and, hence, more computational resources. However, by the advances in high-performance computing in recent years, this type of simulations are realistic.

A. LES benchmark test case

The separated turbulent flow past an inclined flat plate, investigated in [75], was selected to evaluate the numerical methods and CFD code used in the present work. The test case was selected because of the similarities to the flow around a heliostat, which can be simplified to an inclined flat plate with sharp edges. The simplicity of the case, the detailed description and extensive data given in [75] makes it suitable for a benchmark. Furthermore, the reference case was computed with a well-known academic code called *LESOCC* [109, 110] that has been validated with a variety of test cases [74, 109–112].

A.1. Geometry and boundary conditions

The configuration consists of an inclined flat plate at an angle $\alpha = 18°$ with a chord length c as shown in Fig. A.1. The plate is located in the center of a channel of height $3c$ and 2 chord lengths from the inlet plane. The spanwise extension of the channel and plate is one chord length. The configuration represents a quasi two-dimensional geometry. Therefore, periodic boundary conditions are set in spanwise direction which has an extension of c. At the inlet, a constant velocity without perturbations is prescribed. The Reynolds number based on the chord length is $Re = 2.0 \times 10^4$. At the surfaces of the plate no-slip boundary conditions are applied. At the walls of the channel, slip boundary conditions are used. In the reference simulations a convective boundary condition given by

$$\frac{\partial u_i}{\partial t} + U_{oo}\frac{\partial u_i}{\partial x} = 0 \tag{A.1}$$

is implemented at the outlet to ensure that the vortices pass through the outflow without any significant effects on the upstream flow field. Since the convective boundary

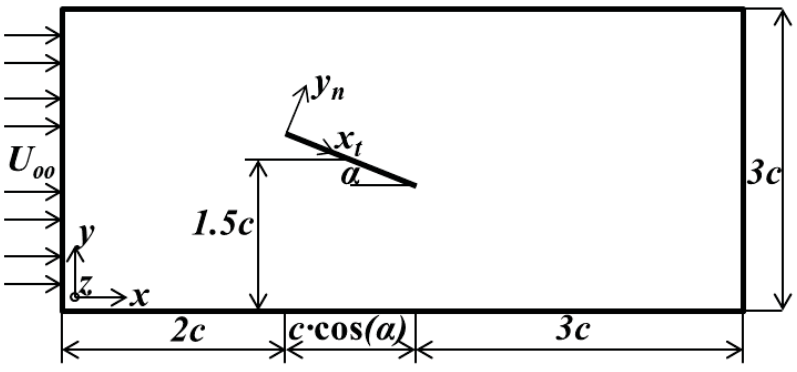

Figure A.1.: Sketch of the flow configuration.

condition is not available in the CFD code Fluent [52] used in the present work, an average pressure specification available in the code is chosen to allow for local variations caused by vortices, while maintaining the averaged specified value across the outlet. This reduces the reflectivity of the boundary compared to a uniform pressure boundary condition. The pressure $p_{f,i}$ of each face element of the outlet plane is computed using weighted interior cell values to satisfy the specified average pressure as:

$$p_{f,i} = 0.5(p_{c,i} + p_{out}) + \Delta p_i, \tag{A.2}$$

where $p_{c,i}$ is the pressure of the neighboring cell in the normal direction of the plane, p_{out} is the specified outlet pressure and Δp_i is the pressure difference calculated as:

$$\Delta p_i = p_{out} - \frac{1}{A}\sum_{i=1}^{N} 0.5(p_{c,i} + p_{out})A_i, \tag{A.3}$$

where A_i is the area of face i and A is the total area of the outlet plane consisting of N faces.

A.2. Numerical setup and grids

LES predictions were performed using the finite-volume CFD code Fluent to solve the incompressible NS-equations. In analogy to the reference simulations, the central differencing scheme (CDS) was used to approximate the convective terms in the momentum equations, and a second-order implicit method was used for time integration. The SIMPLEC algorithm was used for pressure-velocity coupling in the present work, while the reference simulations adopted a predictor-corrector scheme combined with the momentum interpolation technique [113]. The unresolved turbulence scales were computed by simple algebraic eddy-viscosity models; the reference simulations were performed using the Smagorinsky model [114] with a Van Driest damping function, whereas in the present study the Wall-Adapted Local Eddy Viscosity (WALE) model [49] was chosen due to the advantages of returning the correct eddy viscosity for wall-bounded flows as well as for laminar shear layers [115]. In wall regions where the viscous sublayer is not resolved, wall-functions are used by default in Fluent. The three-layer log-law proposed in [77] is used for this purpose. The boundary layer is described in normalized form by the velocity u^+ and the wall distance y^+ defined as:

$$u^+ = \frac{\widetilde{u}}{u_\tau} \qquad \text{and} \qquad y^+ = \frac{\rho u_\tau y}{\mu}, \tag{A.4}$$

where $\widetilde{u}$ is the resolved velocity at the wall-nearest point and y is the wall-normal distance. In the innermost layer, called *viscous sublayer*, the flow is nearly laminar due to the dominant role of the molecular viscosity. In this region, located at $y^+ < 5$, the velocity profile is given by:

$$u^+ = y^+. \tag{A.5}$$

In the outer layer, called *log-law region*, the effect of the molecular viscosity on the mean velocity profile is negligible and the flow is turbulent. This region, found at $y^+ > 60$ is described by:

$$u^+ = \frac{1}{\kappa} \ln\left(Ey^+\right), \tag{A.6}$$

where κ is the von Karman constant and $E = 9.793$. The region between the viscous sublayer and the log-law region, called *buffer layer*, is approximated by blending Eq. (A.5) and (A.6) as:

$$u^+ = e^{\psi} y^+ + e^{1/\psi} \frac{1}{k} \ln\left(Ey^+\right), \tag{A.7}$$

where the blending parameter ψ is given by:

$$\psi = -\frac{a(y^+)^4}{1 + by^+}, \tag{A.8}$$

with $a = 0.01$ and $b = 5$.

Two computational grids with different resolutions were used in the present investigation. Both grids consist of hexahedral cells clustered in the vicinity of the flat plate and towards the leading and trailing edges as displayed in Fig. A.2. Information on the grid resolutions is presented in Tab. A.1 together with the reference simulations [75]. The medium grid resolution (LES-WALE-M) is notably coarser than the reference case, while keeping the same wall-normal distance to achieve $y^+ \leq 1$. The coarsest grid (LES-WALE-C), however, has a wall-normal spacing ten times higher than the other cases, in order to investigate the use of wall functions. Time step sizes of $\Delta t = 0.001 \times c/U_\infty$ and $\Delta t = 0.005 \times c/U_\infty$ were used for the medium and coarse grid, respectively, to achieve $CFL < 1$ as in the reference case. The simulations were performed for a total of 220 convective time units $t \cdot U_\infty/c$ and the flow quantities used in the analysis were averaged over the last 200 units to exclude initialization effects.

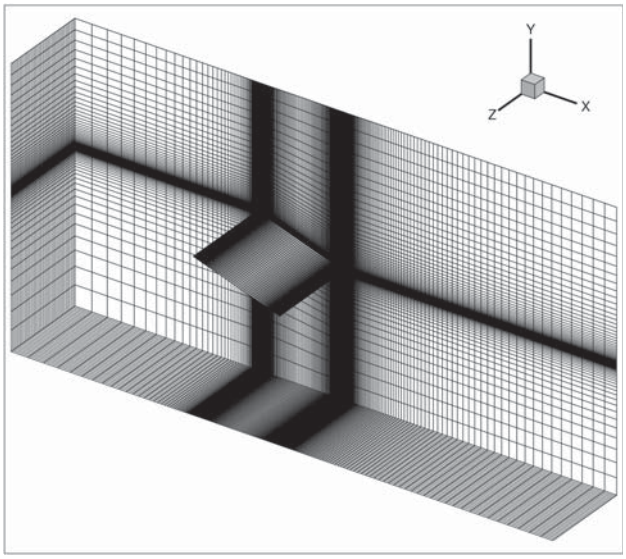

Figure A.2.: Computational grid.

Case	Total No. of CVs	CVs along plate length	CVs along plate width	Wall-normal spacing
Breuer et al., 2003	8.97×10^6	298	76	$0.001 \times c$
LES-WALE-M	2.63×10^6	198	54	$0.001 \times c$
LES-WALE-C	0.74×10^6	100	36	$0.01 \times c$

Table A.1.: Grid information.

A.3. Results and discussion

The mean flow field is compared in Fig. A.3 by the time-averaged streamlines which are characterized by two recirculation regions on the leeward side. The large clockwise rotating vortex separates at the leading edge and the smaller counter-clockwise rotating vortex originates at the trailing edge. All simulations exhibit a very similar flow field. To quantify the differences, the location of the center of the vortices is compared in Tab. A.2 in normalized form. The agreement to the reference data is very good in both cases. The maximal difference is found at the coarse grid at the trailing-edge vortex with a deviation of 2.9% of the chord length.

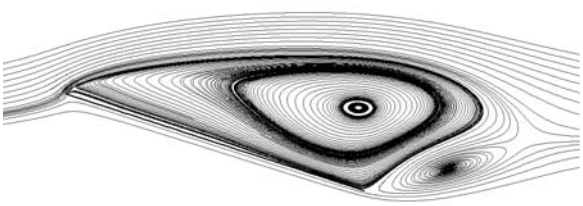

(a) LES-WALE-C

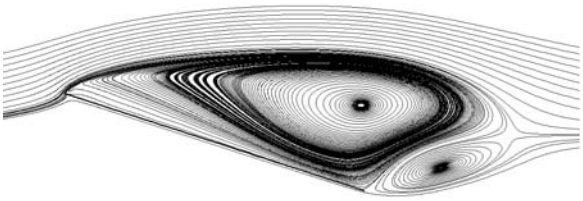

(b) LES-WALE-M

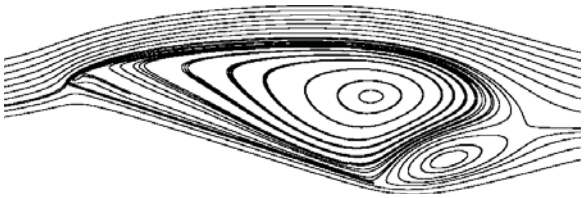

(c) Breuer et al., 2003 (reproduced with permission)

Figure A.3.: Time-averaged streamlines.

	leading-edge vortex			trailing-edge vortex		
Case	x_t/c	y_n/c	deviation [%]	x_t/c	y_n/c	deviation [%]
Breuer et al., 2003	0.912	0.254	0	1.201	0.142	0
LES-WALE-M	0.906	0.256	0.6	1.207	0.145	0.7
LES-WALE-C	0.925	0.254	1.3	1.230	0.144	2.9

Table A.2.: Location of the center of vortices.

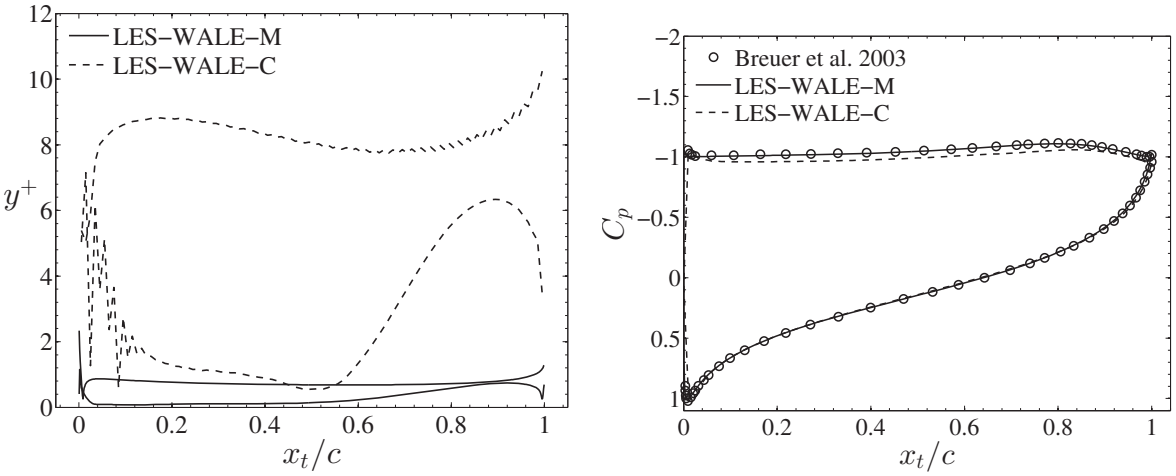

Figure A.4.: Profiles of averaged pressure coefficient C_p and y^+.

Case	$\overline{C}_l$	$\overline{C}_d$	σ_{C_l}	σ_{C_d}	St
Breuer et al., 2003	1.13	0.38	0.070	0.022	0.62
LES-WALE-M	1.12	0.38	0.069	0.022	0.63
LES-WALE-C	1.07	0.36	0.070	0.022	0.63

Table A.3.: Statistical values of force coefficients for different grid resolutions.

Despite values of $1 < y^+ < 10$ found at the coarse grid, the normalized pressure distribution along the surface is in good agreement between all cases as shown in Fig. A.4, where slight differences of $< 5\%$ are found at the leeward side in LES-WALE-C. The mean lift and drag coefficients, as well as their standard deviations are presented in Tab. A.3 together with the Strouhal number. As above, the mean quantities are in very good agreement with the reference simulation with a maximal deviation of 5% found in $\overline{C}_l$ at the coarse grid. The standard deviations and Strouhal number, which are a measure of the fluctuating loads, are almost identical in all cases.

A more detailed quantitative comparison is conducted by analyzing profiles of the time-averaged velocity and Reynolds stresses along four different lines normal to the plate located at $x/c = 0.2, 0.6, 1.0$ and 1.2. As can be observed in Fig. A.5, the normalized tangential velocity component (i.e., in x_t direction) from the present simulations agree very well at all locations with the reference data and resolve accurately the velocity gradients resulting from the recirculating regions. In the profiles of the Reynolds stresses, however, some discrepancies can be observed, specially at the coarse grid which is not capable of resolving the gradients and fails to return the peak values. The medium grid resolution comes very close to the reference data, particularly concerning the normal stresses. The largest discrepancies are, in general, found for the shear stresses displayed in Fig. A.8.

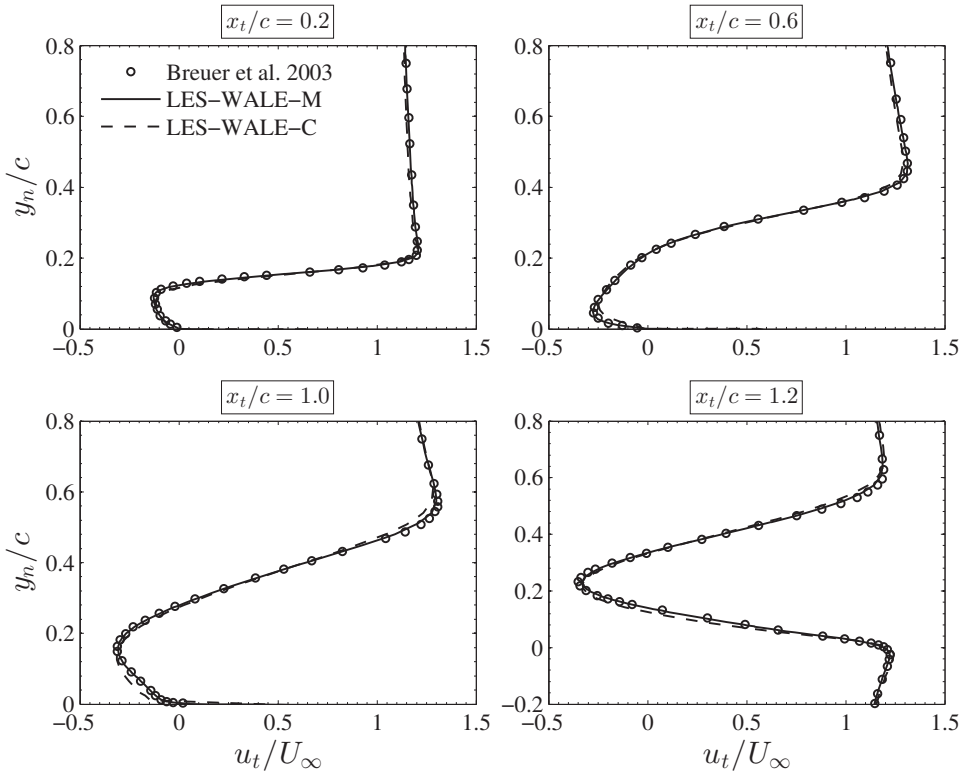

Figure A.5.: Profiles of the tangential velocity.

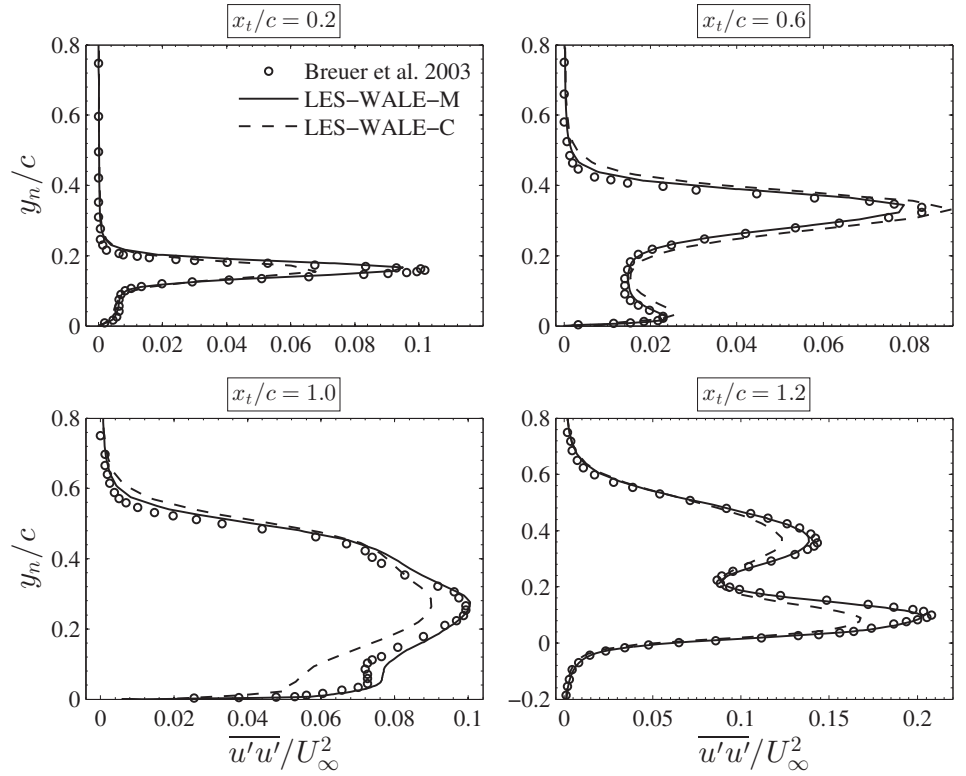

Figure A.6.: Profiles of the normal Reynolds stress $\overline{u'u'}/U_\infty^2$.

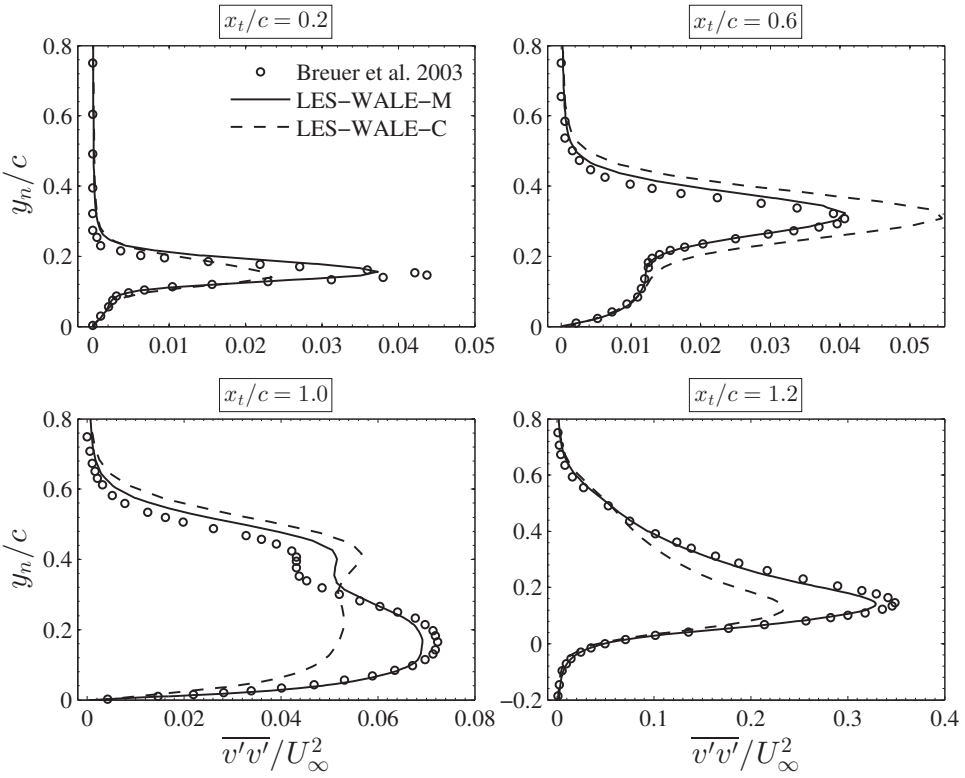

Figure A.7.: Profiles of the normal Reynolds stress $\overline{v'v'}/U_\infty^2$.

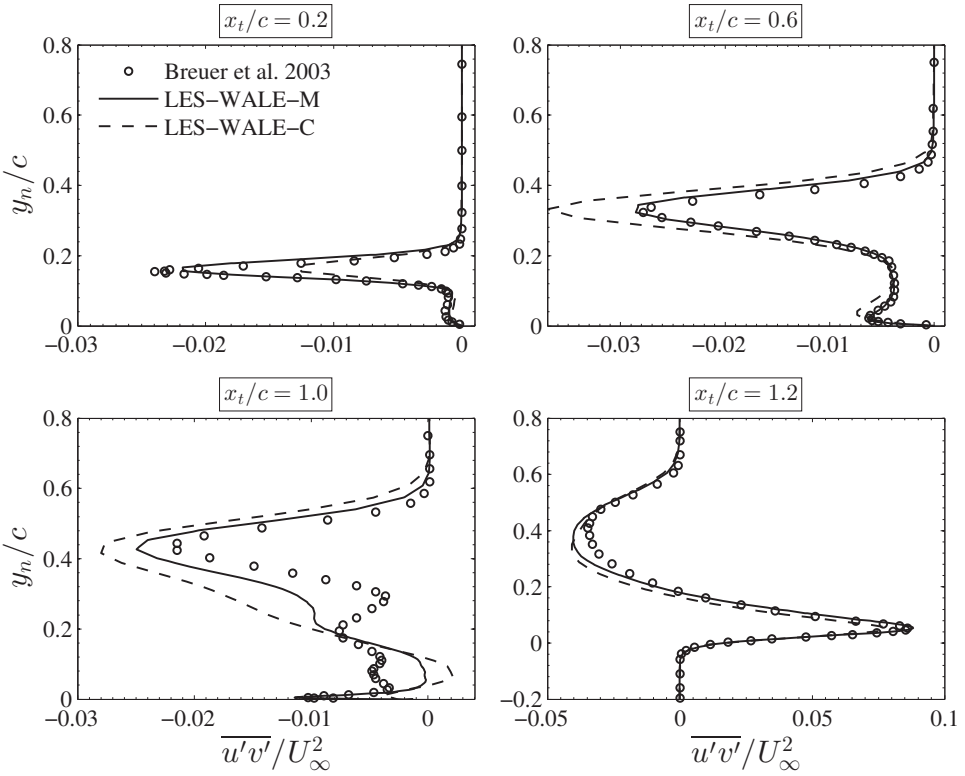

Figure A.8.: Profiles of the shear Reynolds stress $\overline{u'v'}/U_\infty^2$.

A.4. Conclusions from benchmark test case

The numerical methods adopted in the present study were verified by reproducing the results of a highly-resolved LES prediction. Considering the large differences in the grid resolutions compared to the reference case, the results presented above are very satisfactory and indicate that such a flow configuration can be simulated accurately at a relatively low computational effort. Based on the very good agreement obtained by the medium grid, it can be concluded that the influence of the SGS model, which is one of the main differences to the reference case, is negligible. By further coarsening the grid and the adoption of wall-functions, the results were still satisfactory for the prediction of the mean flow field and in terms of mean and fluctuating components of the forces. Only higher-order statistics, given by the Reynolds stresses, showed noticeable differences for the coarsest resolution.

B. Flow simulation results

B.1. Statistical convergence

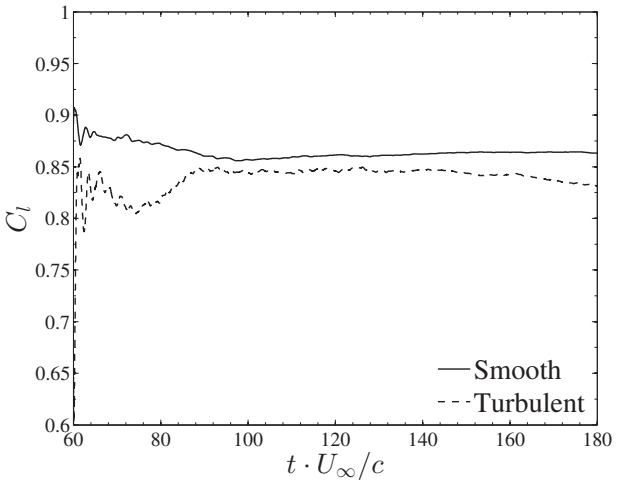

Figure B.1.: Running average of the lift coefficient for the case $\alpha = 20°$ computed after the initial transient period $t \cdot U_\infty / c > 60$. For $t \cdot U_\infty / c > 100$ the running averages change less than 0.7% and 1.6% of their corresponding final mean for the Smooth and Turbulent inflow conditions, respectively.

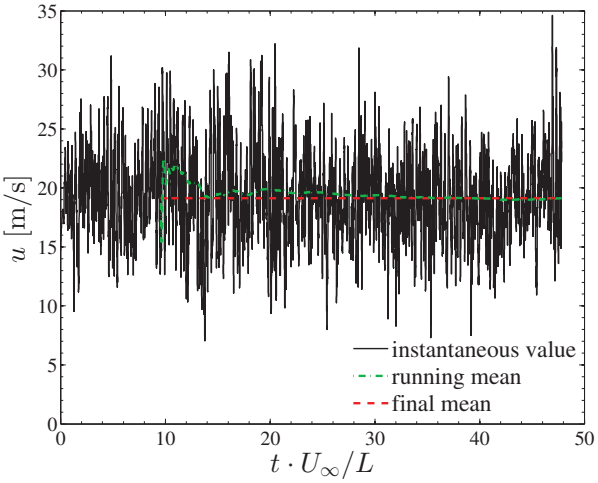

Figure B.2.: Time history of the streamwise velocity used to determine the simulation time required for the mean quantities to converge statistically in the study of the synthetic turbulence. For $t \cdot U_\infty / L > 30$ the running mean is nearly constant, where L is the length of the domain in streamwise direction.

B.2. Grid dependency

The mean flow field compared at different grid resolutions does not show noticeable differences as shown below in the time-averaged flow field around the plate.

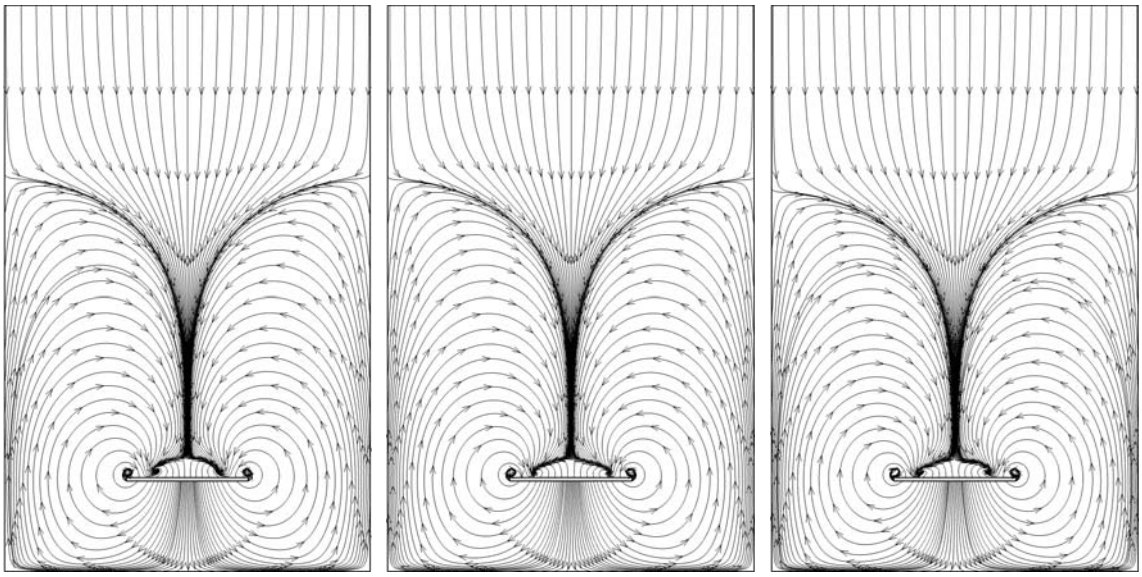

(a) coarse (b) medium (c) fine

Figure B.3.: Time-averaged streamlines at mid-chord plane $x_t/c = 0.5$.

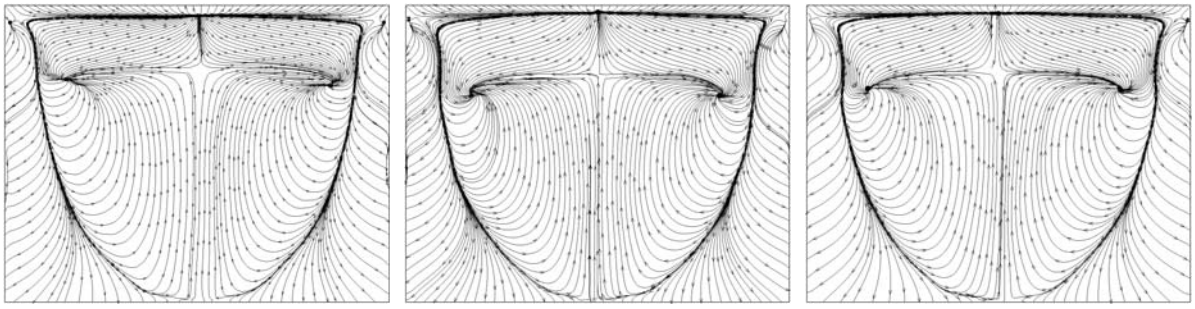

(a) coarse (b) medium (c) fine

Figure B.4.: Time-averaged streamlines on top surface.

The PSD of the lift coefficient shown in Fig. B.5 match relatively well for different grid resolutions. Only a minor difference can be observed at the peak associated to the tip vortices found at about 40 Hz, where the magnitude increases with the grid resolution. The main features of the turbulence field shown in Fig. B.6 are well reproduced by all grid resolutions and the eddy viscosity ratio does not increase significantly when decreasing the grid resolution. However, in the coarse grid small-scale turbulence structures are less abundant than at higher resolutions.

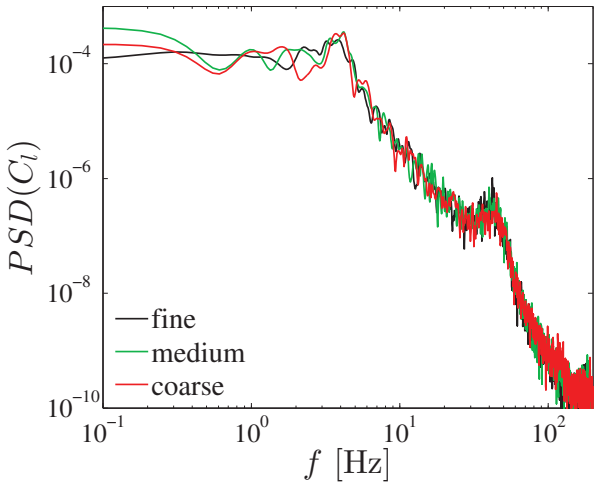

Figure B.5.: Power spectral density of the lift coefficient.

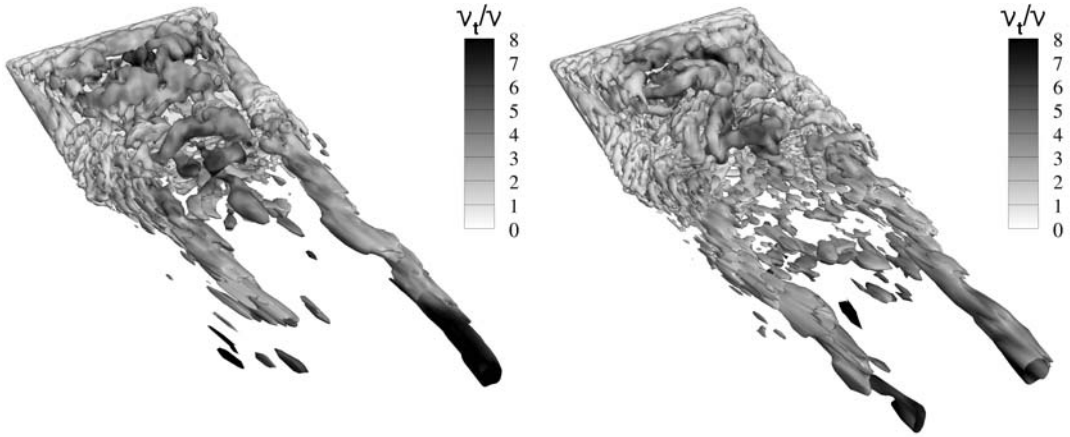

(a) coarse

(b) medium

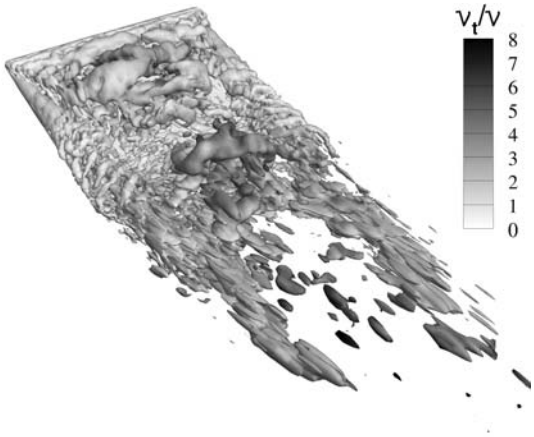

(c) fine

Figure B.6.: Instantaneous snapshots of turbulence structures represented by isosurfaces of $\lambda_2 = -500$ and shaded by the eddy viscosity ratio ν_t/ν which gives the level of unresolved turbulence as the ratio increases.

B.3. Inflow conditions

The figures below show the influence of the turbulent dissipation rate ϵ as parameter of the vortex method (see Eq. (2.25)) on the vortex size and energy spectra. By increasing ϵ the vortex size decreases as shown in Fig. B.7. This, in turn, affects the spectral distribution of the velocity components by displacing energy to higher frequencies as can be observed in Fig. B.8. The peak of the spectra, associated to the size of the largest vortices, is displaced to higher frequencies as well. The peak frequency for $\epsilon = 24\,\mathrm{m}^2/\mathrm{s}^3$ is found at approximately 2.7 Hz and for $\epsilon = 48\,\mathrm{m}^2/\mathrm{s}^3$ at about 5.2 Hz.

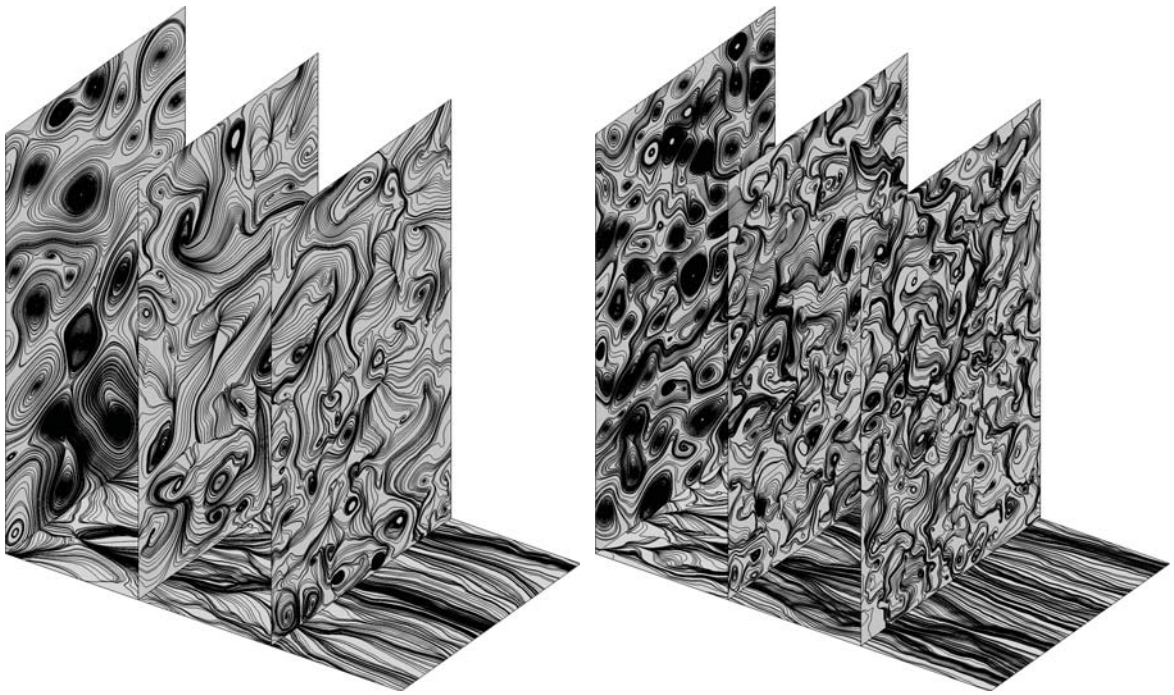

(a) $\epsilon = 24\,\mathrm{m}^2/\mathrm{s}^3$ (b) $\epsilon = 48\,\mathrm{m}^2/\mathrm{s}^3$

Figure B.7.: Streamlines of the instantaneous flow for different turbulent dissipation rates ϵ as parameter of the VM.

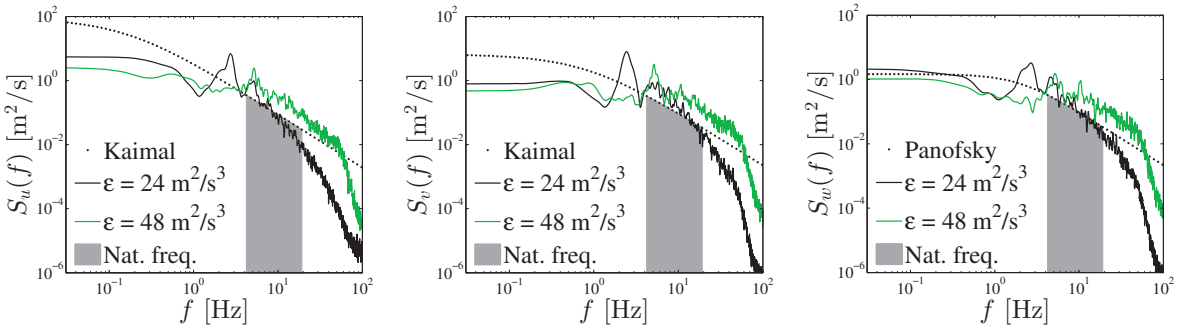

Figure B.8.: Power spectral density of the velocity components for different turbulent dissipation rates ϵ as parameter of the VM.

C. Modal and dynamic analysis results

Figure C.1 shows that the mode shapes predicted numerically agree very well with the experimental results at $\alpha = 0°$ and 60°. Furthermore, it can be observed that the mode shapes do not depend on the elevation angle.

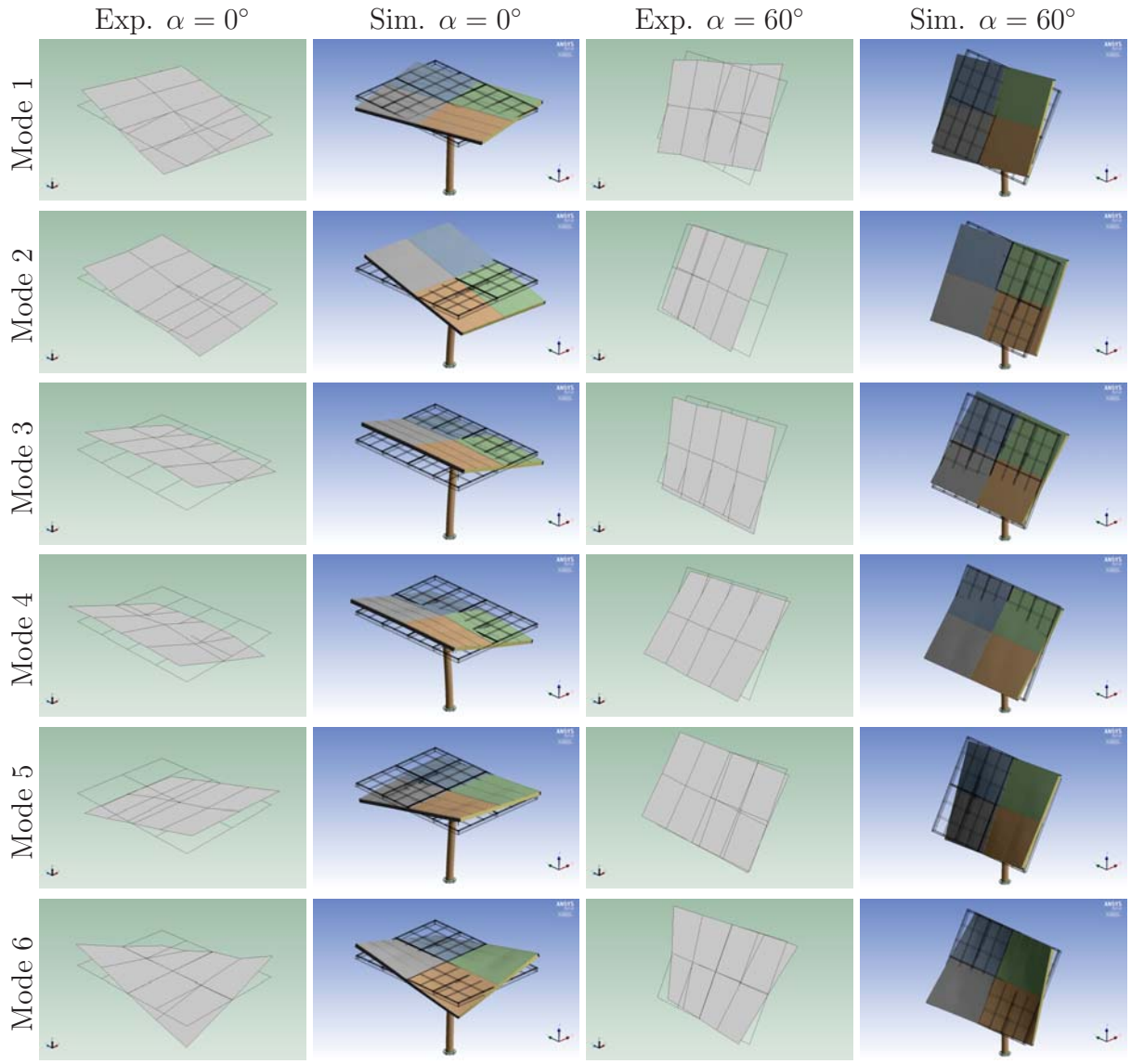

Figure C.1.: Mode shapes at $\alpha = 0°$ and 60°.

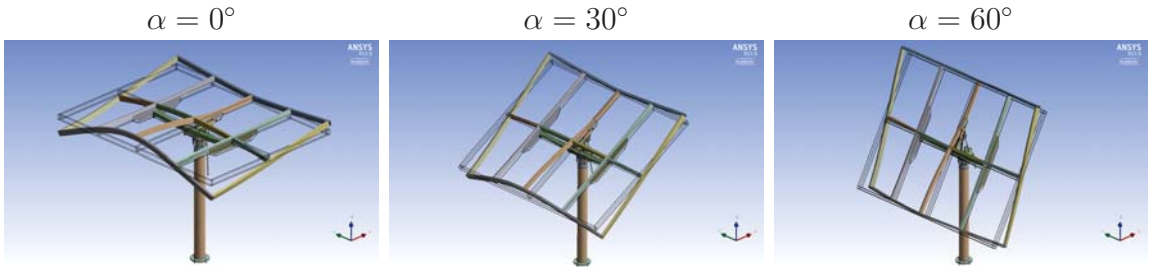

Figure C.2.: Mode 8 at different elevation angles. This is a bending mode of the mirror frame at 30 Hz that has been detected in the frequency response function for the moment about the elevation axis.

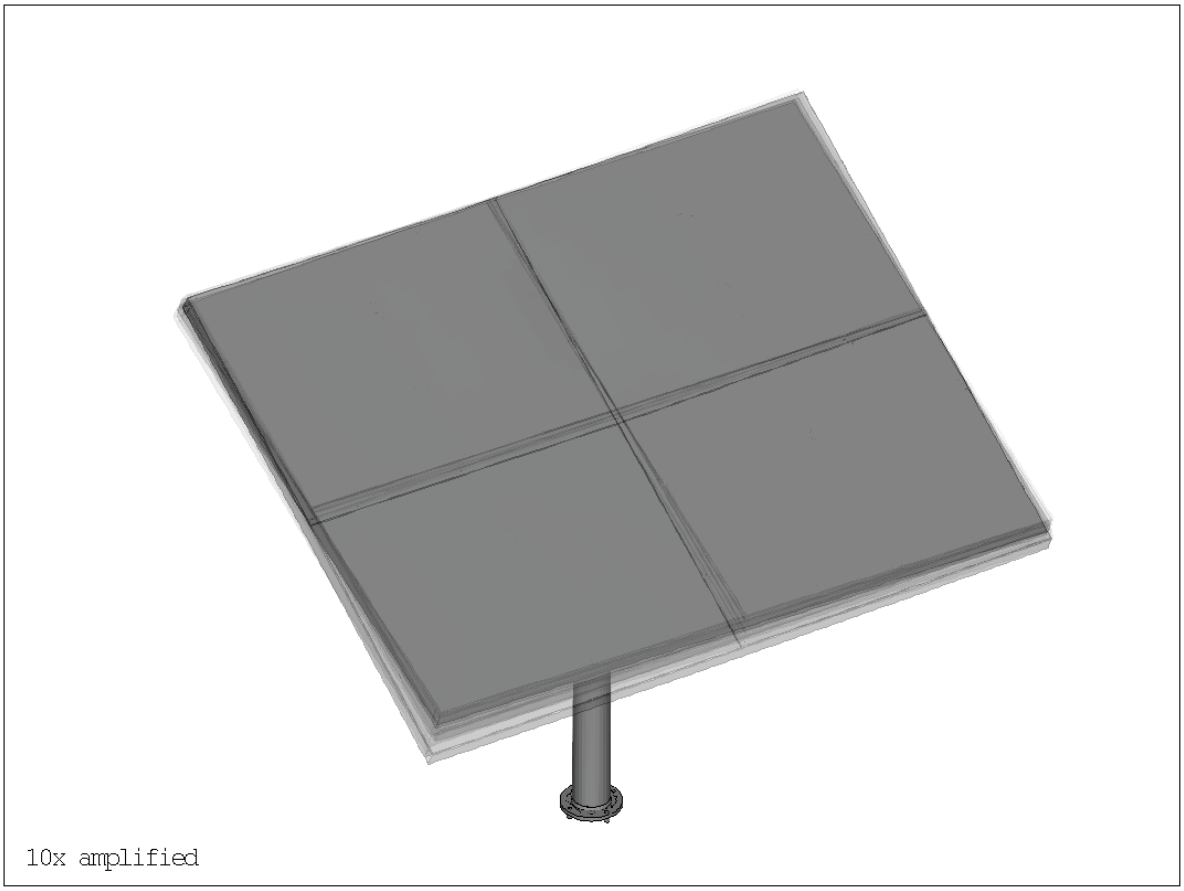

Figure C.3.: Overlapped sequence of snapshots from the transient FE results that create a motion effect of the oscillation of the mirror frame about the elevation axis for the case $\alpha = 5°$.

D. Wind data results

The darkest bars in the wind rose shown below correspond to the wind data samples with magnitudes above 3 m/s used to analyze atmospheric turbulence. It can be noticed that most of these samples are from the south-west direction.

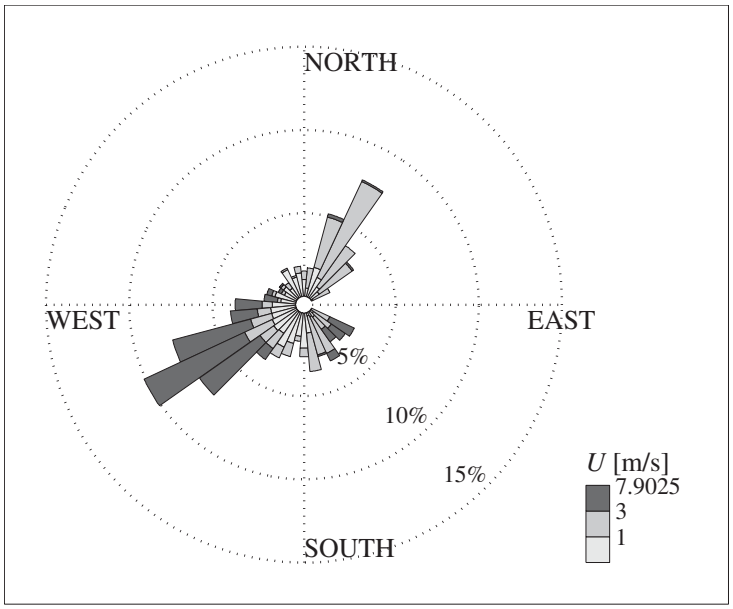

Figure D.1.: Wind rose over multiple periods of 10 min sampled at 20 Hz.

E. Statistical analysis

E.1. Statistical moments

The first statistical moment, or mean value, of a signal x is defined as:

$$\overline{x} = \int_{-\infty}^{\infty} x PDF(x) dx, \tag{E.1}$$

where $PDF(x)$ is the probability density function of x. The second statistical moment, or variance, is given by:

$$\sigma_x^2 = \int_{-\infty}^{\infty} (x - \overline{x})^2 PDF(x) dx. \tag{E.2}$$

The square root of the variance is the standard deviation σ. The root-mean-square, or RMS value, of x can be computed from:

$$RMS(x) = \sqrt{\overline{x}^2 + \sigma_x^2} \tag{E.3}$$

E.2. Autocorrelation function and Power Spectral Density

The Autocorrelation function R_{xx} and the Power Spectral Density S_x of the time signal $x(t)$ are related by Eq. (E.4b)

$$R_{xx}(\tau) = \lim_{T \to \infty} \frac{1}{T} \int_{-T/2}^{T/2} x(t)\, x(t+\tau) dt \tag{E.4a}$$

$$S_x(f) = 2 \int_{-\infty}^{\infty} R_{xx}(\tau) \cos(2\pi f \tau) d\tau \tag{E.4b}$$

where τ and T are the time-lag between samples and the time period, respectively. The integral of the spectrum over the frequency is the variance of the signal:

$$\sigma_x^2 = \int_0^{\infty} S_x df. \tag{E.5}$$

For $y(t) = c\, x(t)$, with $c = const.$, the spectral densities are related by:

$$S_y(f) = c^2 S_x(f). \tag{E.6}$$

Bibliography

[1] Kolb, G. J., Ho, C. H., Mancini, T. R. and Gary, J. A. *Power Tower Technology Roadmap and Cost Reduction Plan*. Tech. Rep. SAND2011-2419, Sandia National Laboratories, Albuquerque, NM, 2011.

[2] Peterka, J., Tan, Z., Cermak, J. and Bienkiewicz, N. Mean and peak wind loads on heliostats. *Journal of Solar Energy Engineering,* **111**(2), pp. 158–164, 1989.

[3] Peterka, J. A. and Derickson, R. G. *Wind Load Design Methods for Ground-Based Heliostats and Parabolic Dish Collectors*. Tech. Rep. SAND92-7009, Sandia National Laboratories, Albuquerque, NM, 1992.

[4] Peglow, S. G. *Wind Tunnel Study of a Full-Scale Heliostat*. Tech. Rep. SAND79-8034, Sandia National Laboratories, Livermore, CA, 1979.

[5] Huss, S., Traeger, Y. D., Shvetz, Z., Rojansky, M., Stoyanov, S. and Garber, J. Evaluating effects of wind loads in heliostat design. In *Proc. of the 17th SolarPACES Int. Conference*, Granada, Spain, Sept. 20–23 2011.

[6] Cook, N. J. *The Designer's Guide to Wind Loading of Building Structures. Part 1: Background, Damage, Wind Data and Structural Classification*. Butterworths, London, 1985.

[7] Griffith, D. T., Moya, A. C., Ho, C. K. and Hunter, P. S. Structural dynamics testing and analysis for design evaluation and monitoring of heliostats. In *Proc. of the 5th Int. Conference on Energy Sustainability*, ES2011-54222, pp. 567–576, ASME, Washington, DC, Aug. 7–10 2011.

[8] Ho, C. K., Griffith, D. T., Moya, A. C., Sment, J., Christian, J., Yuan, J. and Hunter, P. Dynamic testing and analysis of heliostats to evaluate impacts of wind on optical performance and structural fatigue. In *Proc. of the 18th SolarPACES Int. Conference*, Marrakech, Marocco, Sept. 11–14 2012.

[9] Sment, J. and Ho, C. Wind patterns over a heliostat field. In *Proc. of the 19th SolarPACES Int. Conference*, Las Vegas, USA, Sept. 17–20 2013.

[10] Zang, C., Christian, J., Yuan, J., Sment, J., Moya, A., Ho, C. and Wang, Z. Numerical simulation of wind loads and wind induced dynamic response of heliostats. In *Proc. of the 19th SolarPACES Int. Conference*, Las Vegas, USA, Sept. 17–20 2013.

[11] Rebolo, R., Lata, J. and Vázquez, J. Design of heliostats under extreme and fatigue wind loads. In *Proc. of the 17th SolarPACES Int. Conference*, Granada, Spain, Sept. 20–23 2011.

[12] EN 1991-1-4:2005. *Eurocode 1: Actions on structures - Part 1-4: General actions - Wind actions*.

[13] DIN 1055-4:2005-03. *Einwirkungen auf Tragwerke - Teil 4: Windlasten.*

[14] Weinrebe, G. *Technische, ökologische und ökonomische Analyse von solarthermischen Turmkraftwerken.* PhD thesis, Universität Stuttgart, 2000.

[15] Mancini, T. R. *Catalogue of solar heliosats.* Tech. Rep. III-1/00, IEA SolarPACES, Albuquerque, NM, 2000.

[16] Dyrbye, C. and Hansen, S. O. *Wind Loads on Structures.* John Wiley & Sons, Chichester, England, 1997.

[17] Cook, N. J. *The Designer's Guide to Wind Loading of Building Structures. Part 2: Static Structures.* Butterworths, London, 1990.

[18] Plate, E. J., ed. *Engineering Meteorology, Studies in Wind Engineering and Industrial Aerodynamics, Vol. 1.* Elsevier, Amsterdam - Oxford - New York, 1982.

[19] Simiu, E. and Scanlan, R. H., eds. *Wind Effects on Structures.* John Wiley & Sons, New York, 1996.

[20] Davenport, A. G. Gust loading factors. *Journal of the Structural Division, ASCE,* **93**(3), pp. 11–34, 1967.

[21] Holmes, J. D. *Wind Loading of Structures.* Spon Press, London, 2001.

[22] Gong, B., Li, Z., Wang, Z. and Wang, Y. Wind-induced dynamic response of heliostat. *Renewable Energy,* **38**(1), pp. 206 – 213, 2012.

[23] Pfahl, A., Brucks, A. and Holze, C. Wind load reduction for light-weight heliostats. In *Proc. of the 19th SolarPACES Int. Conference*, Las Vegas, USA, Sept. 17–20 2013.

[24] Davenport, A. G. and King, J. P. C. Vibration of structures induced by wind. In *Harris' Shock and Vibration Handbook*, 6th ed., A. G. Piersol and L. T. Paez, eds., pp. 31.1–31.26, McGraw-Hill, New York, 2009.

[25] Miner, M. Cumulative damage in fatigue. *Journal of Applied Mechanics,* **67**, pp. 159–164, 1945.

[26] Matsuishi, M. and Endo, T. Fatigue of metals subjected to varying stress. In *Kyushu Branch Meeting of the Japan Society of Mechanical Engineers*, pp. 37–40, Fukuoka, Japan, March 1968.

[27] Bearman, P. and Morel, T. Effect of free-stream turbulence on the flow around bluff bodies. *Progress in Aerospace Sciences,* **20**, pp. 97–123, 1983.

[28] Scruton, C., Rogers, E., Menzies, J. and Scorer, R. Steady and unsteady wind loading of buildings and structures. *Phil. Trans. of the Royal Society of London. Series A,* **269**(1199), pp. 353–383, 1971.

[29] Hoerner, S. *Fluid-Dynamic Drag.* published by the author, Midland Park, NJ, 1965.

[30] Flachsbart, O. Messungen an ebenen und gewölbten Platten. *Ergebnisse der Aerodynamischen Versuchsanstalt zu Göttingen,* **4**, pp. 96–100, 1932.

[31] Abernathy, F. Flow over an inclined plate. *Transactions of the ASME. Series D, Journal of Basic Engineering,* **61**(Sept.), pp. 380–388, 1962.

[32] Bearman, P. An investigation of the forces on flat plates normal to a turbulent flow. *Journal of Fluid Mechanics,* **46**, pp. 177–198, 1971.

[33] Vickery, B. Fluctuating lift and drag on a long cylinder of square cross-section in a smooth and in a turbulent stream. *Journal of Fluid Mechanics,* **25**, pp. 481–494, 1966.

[34] Bearman, P. Turbulence effects on bluff body mean flow. In *Proc. of the 3rd U.S. Nat. Conf. on Wind Engineering*, Gainesville, FL, March 1978.

[35] Hillier, R. *Investigation of the Mean Flow Properties in the Separated Region downstream of a Forward-Facing Step*. Tech. Rep. RD/L/N242/75, C.E.R.L., 1976.

[36] Bergeles, G. and Athanassiadis, N. The flow past a surface-mounted obstacle. *ASME. J. Fluids Eng.,* **105**(4), pp. 461–463, 1983.

[37] Davenport, A. G. The relationship of wind structure to wind loading. In *Proc. of the Symposium on Wind Effects on Buildings and Structures*, Vol. 1, pp. 53–102, National Physical Laboratory, Her Majesty's Stationery Office, London, 1965.

[38] Breuer, M. *Direkte Numerische Simulation und Large-Eddy Simulation turbulenter Strömungen auf Hochleistungsrechnern*. Berichte aus der Strömungstechnik. Shaker Verlag, Aachen, 2002.

[39] Pope, S. B. *Trubulent Flows*. Cambridge University Press, 2000.

[40] Van der Hoven, I. Power spectrum of horizontal wind speed in the frequency range from 0.0007 to 900 cycles per hour. *Journal of Meteorology,* **14**, pp. 160–164, 1956.

[41] Kaimal, J., Wyngaard, J., Izumi, Y. and Cote, O. Spectral characteristics of surface-layer turbulence. *J. Royal Meteorol. Soc.,* **96**, pp. 563–589, 1972.

[42] Lumley, J. and Panofsky, H. *The Structure of Atmospheric Turbulence*. Interscience Publishers, New York, 1964.

[43] Ferziger, J. and Perić, M. *Computational Methods for Fluid Dynamics*. Springer Verlag, Berlin, 2002.

[44] Mockett, C. *A comprehensive study of detached-eddy simulation*. PhD thesis, TU-Berlin, 2009.

[45] Casey, M. and Wintergerste, T., eds. *Best Practice Guidelines*. ERCOFTAC Special Interest Group on Quality and Trust in Industrial CFD, 2000.

[46] Fröhlich, J. and von Terzi, D. Hybrid LES/RANS methods for the simulation of turbulent flows. *Progress in Aerospace Sciences,* **44**, pp. 349–377, 2008.

[47] Ferziger, J. Large-eddy numerical simulations of turbulent flows. *AIAA Journal,* **15**(9), pp. 1261–1267, 1977.

[48] Fröhlich, J., Mellen, C., Rodi, W., Temmerman, L. and Leschziner, M. Highly resolved large-eddy simulation of separated flow in a channel with streamwise periodic restrictions. *Journal of Fluid Mechanics,* **526**, pp. 19–66, 2005.

[49] Ducros, F., Nicoud, F. and Poinsot, T. Wall-adapting local eddy-viscosity models for simulations in complex geometries. In *6th ICFD Conference on Numerical Methods for Fluid Dynamic*, M. Baines, ed., pp. 293–299, Oxford Univesity Computing Laboratory, Oxford, 1998.

[50] Hinze, J. *Turbulence*, 2nd ed. McGraw-Hill, New York, 1975.

[51] Fröhlich, J. *Large-Eddy Simulation turbulenter Strömungen.* Teubner Verlag, Wiesbaden, 2006.

[52] ANSYS Inc. *ANSYS Fluent User's Guide.* Release 15.0. Canonsburg, PA, 2013.

[53] Tabor, G. R. and Baba-Ahmadi, M. H. Inlet conditions for large-eddy simulation: A review. *Computers & Fluids,* **39**, pp. 553–567, 2010.

[54] Sergent, E. *Vers une Méthodologie de Couplage entre la Simulation des Grandes Echelles et les Modèles Statistiques.* PhD thesis, L'Ecole Centrale de Lyon, 2002.

[55] Mathey, F., Cokljat, D., Bertoglio, J. and Sergent, E. Assessment of the vortex method for large-eddy simulation inlet conditions. *Progress in Computational Fluid Dynamics,* **6**(1/2/3), pp. 58–67, 2006.

[56] Avitabile, P. Experimental modal analysis: A simple non-mathematical presentation. *Sound and Vibration*, pp. 1–11, 2001.

[57] Maia, N. M. M. and Montalvao e Silva, J. *Theoretical and Experimental Modal Analysis.* John Wiley & Sons, New York, 1997.

[58] Ewins, D. J. *Modal Testing: Theory, Practice and Application*, 2nd ed. Research Studies Press Ltd., Philadelphia, PA, 2000.

[59] Stelzmann, U., Groth, C. and Müller, G. *FEM für Praktiker - Band 2: Strukturdynamik.* 5. Aufl. Expert Verlag, Renningen, 2008.

[60] ANSYS Inc. *ANSYS Mechanical APDL Structural Analysis Guide.* Release 15.0. Canonsburg, PA, 2013.

[61] Wilbert, S. *Determination of Circumsolar Radiation and its Effect on Concentrating Solar Power.* PhD thesis, RWTH-Aachen, 2014.

[62] Wolfertstetter, F. and Wilbert, S. Unpublished meteorological data collected between 2009 and 2014. DLR Institute of Solar Research, Department of Qualification, Plataforma Solar de Almeria, Spain.

[63] ISO 9060:1990. *Solar energy - Specification and classification of instruments for measuring hemispherical solar and direct solar radiation.*

[64] Welch, P. D. The use of fast Fourier transform for the estimation of power spectra: A method based on time averaging over short, modified periodograms. *IEEE Trans. Audio Electroacustics,* **15**, pp. 70–73, 1967.

[65] ESDU-8520. *Characteristics of Atmospheric Turbulence Near the Ground. Part II: Single Point Data for Strong Winds (Neutral Atmosphere).* 2001.

[66] Vásquez-Arango, J. F., Buck, R. and Pitz-Paal, R. Dynamic properties of a heliostat structure determined by numerical and experimental modal analysis. *Journal of Solar Energy Engineering,* **137**(5), 2015.

[67] Brüel & Kjaer. *PUSLE LabShop Documentation.* Naerum, Denmark, 2012.

[68] Brüel & Kjaer. *PUSLE Reflex Documentation.* Naerum, Denmark, 2012.

[69] Døssing, O. *STRUCTURAL TESTING Part I: Mechanical Mobility Measurements.* Brüel & Kjaer. Naerum, Denmark, 1988.

[70] Böning, G. and Kunert, J. Antriebstechnologie für Heliostate - Auslegung und Beispiele. In *Sonnenkolloquium*, Köln, Jun. 24 2008.

[71] Grimes, R., Lewis, J. and Knisely, H. S. W. A shifted block Lanczos algorithm for solving sparse symmetric generalized eigenproblems. *SIAM Journal on Matrix Analysis Applications,* **15**(1), pp. 228–272, 1996.

[72] Fage, A. and Johansen, F. C. On the flow of air behind an inclined flat plate of infinite span. *Proc. of the Royal Society of London. Series A,* **116**(773), pp. 170–197, 1927.

[73] Knisely, C. W. Strouhal numbers of rectangular cylinders at incidence: A review and new data. *Journal of Fluids and Structures,* **4**(4), pp. 371–393, 1990.

[74] Breuer, M., Jovičić, N. and Mazaev, K. Separated flow around a flat plate at high incidence: An LES investigation. *Journal of Turbulence,* **2**, pp. 1–15, 2001.

[75] Breuer, M., Jovičić, N. and Mazaev, K. Comparison of DES, RANS, and LES for the separated flow around a flat plate at high incidence. *Int. J. for Numerical Methods in Fluids,* **41**, pp. 357–388, 2003.

[76] ANSYS Inc. *ANSYS ICEM CFD User's Manual.* Release 15.0. Canonsburg, PA, 2013.

[77] Kader, B. Temperature and concentration profiles in fully turbulent boundary layer. *Int. J. Heat and Mass Transfer,* **24**(9), pp. 1541–1544, 1981.

[78] ANSYS Inc. *ANSYS ICEM CFD Help Manual*, release 15.0 ed. Canonsburg, PA, 2013.

[79] Breuer, M. and Jovičić, N. High-performance computing for the investigation of the flow past an airfoil with trailing-edge stall. In *High Performance Computing in Science and Engineering, Garching/Munich 2007*, S. Wagner, M. Steinmetz, A. Bode, and M. Brehm, eds. pp. 227–240. Springer Verlag, Berlin-Heidelberg, 2009.

[80] Piomelli, U. and Balaras, E. Wall-layer models for large-eddy simulations. *Annual Review of Fluid Mechanics,* **34**, pp. 349–374, 2002.

[81] Leonard, B. P. The ultimate conservative difference scheme applied to unsteady one-dimensional advection. *Computer Methods in Applied Mechanics and Engineering,* **88**, pp. 17–74, 1991.

[82] Jeong, J. and Hussain, F. On the identification of a vortex. *Journal of Fluid Mechanics,* **285**, pp. 69–94, 1995.

[83] Freymuth, P., Finaish, F. and Bank, W. Further visualization of combined wing tip and starting vortex systems. *AIAA Journal,* **25**(9), pp. 1153–1159, 1987.

[84] Mitchell, A., Morton, S. and Forsythe, J. Analysis of delta wing vortical substructures using detached-eddy simulation. *AIAA Journal,* **44**(5), pp. 964–972, 2006.

[85] Torres, E. and Mueller, T. J. Low aspect ratio aerodynamics at low Reynolds numbers. *AIAA Journal,* **42**(5), pp. 865–873, 2004.

[86] Davidson, L. Large-eddy simulations: How to evaluate the resolution. *Int. J. Heat and Fluid Flow,* **30**, pp. 1016–1025, 2009.

[87] Lignarolo, L., Gorlé, C. and Benocci, A. Large-eddy simulation of the atmospheric boundary layer using OpenFOAM. In *Proc. of the ICWE13*, Amsterdam, Jul. 10–15 2011.

[88] Cushman-Roisin, B. and Beckers, J. M. *Introduction to Geophysical Fluid Dynamics: Physical and Numerical Aspects*. Academic Press, 2011.

[89] Forestern, W. *Flow visualization in the separation bubble of a rectangular low aspect ratio wing using a smoke wire technique*. Tech. Rep. VKI SR 1981-14, von Karman Institute, 1981.

[90] Westerhoven, P. V. *Flow around a rectangular low aspect ratio wing and the effect of compressibility. Addendum on Flow Visualization*. Tech. Rep. VKI PR 1981-29, von Karman Institute, 1981.

[91] Crompton, M. J. and Barret, R. V. Investigation of the separation bubble formed behind the sharp leading edge of a flat plate at incidence. *Proceedings of the Institution of Mechanical Engineers, Part G: Journal of Aerospace Engineering,* **214**, pp. 157–176, 2000.

[92] Nyquist, H. Certain topics in telegraph transmission theory. *Transactions of the American Institute of Electrical Engineers,* **47**, pp. 617–644, 1928.

[93] Hilber, H. M., Hughes, T. J. R. and Taylor, R. L. Improved numerical dissipation for time integration algorithm in structural dynamics. *Proceedings of the Institution of Mechanical Engineers, Part G: Journal of Aerospace Engineering,* **5**(283), 1977.

[94] Dangliesh, W. A. Statistical treatment of peak gusts on cladding. *Proceedings of the American Society of Civil Engineers, Structural Division,* **97**, pp. 2173–2187, 1971.

[95] K. J. Eaton, J. R. M. and Cook, N. J. Wind loads on low-rise buildings - effects of roof geometry. In *Proc. of the 4th Int. Conference on Wind Effects on Buildings and Structures*, K. Eaton, ed., pp. 95–110, Cambridge University Press, Heathrow, September 1975.

[96] Mansfield, N. J., ed. *Human Response to Vibration*. CRC Press, Boca Raton, Fl, 2005.

[97] Strachan, J. W. and Houser, R. M. *Testing and Evaluation of Large-Area Heliostats for Solar Thermal Applications*. Tech. Rep. SAND92-1381, Sandia National Laboratories, Albuquerque, NM, 1992.

[98] Cartwright, D. E. and Longuet-Higgins, M. S. The statistical distribution of the maxima of a random function. *Proceedings of the Royal Society of London. Series A, Mathematical and Physical Sciences,* **237**(1209), pp. 212–232, 1956.

[99] Davenport, A. G. The response of slender, line-like structures to a gusty wind. *Proceedings of the Institution of Civil Engineers,* **23**, pp. 389–408, 1962.

[100] Hatanaka, A. and Tanaka, H. New estimation method of aerodynamic admittance function. *Journal of Wind Engineering and Industrial Aerodynamics,* **90**, pp. 2073–2086, 2002.

[101] Larose, G. L. Experimental determination of the aerodynamic admittance of a bridge deck segment. *Journal of Fluids and Structures,* **13**, pp. 1029–1040, 1998.

[102] Davenport, A. G., King, J. P. C. and Larose, G. L. Taut strip model tests. In *1st International Symposium on Aerodynamics of Large Bridges*, A. Larsen, ed., pp. 113–124, Balkema, Rotterdam, 1992.

[103] Ruscheweyh, H., ed. *Dynamische Windwirkung an Bauwerken*. Bauverlag GmbH, Wiesbaden und Berlin, 1982.

[104] Vickery, B. J. and Davenport, A. G. A comparison of theoretical and experimental determination of the response of elastic structures to turbulent flow. In *Proc. of the Int. Research Seminar on Wind Effects on Buildings and Structures*, Ottawa, Canada, 1967.

[105] Larose, G. L. *The dynamic action of gusty winds on long-span bridges*. PhD thesis, Technical University of Denmark, 1997.

[106] Osgood, B. *Lecture Notes for EE 261 The Fourier Transform and its Applications*. CreateSpace Independent Publishing Platform, Electrical Engineering Department, Stanford University, 2008.

[107] Chan, F. K. Miss distance - generalized variance non-central chi distribution. In *Proc. of the 21st AAS/AIAA Space Flight Mechanics Meeting*, New Orleans, LA, Feb. 13–17 2011.

[108] Teufel, E., Buck, R., Pfahl, A., Böing, A. and Kunert, J. Dimensioning of heliostat components under wind and gravity load: The map approach. In *Proc. of the 14th SolarPACES Int. Conference*, Las Vegas, NV, March 4–7 2008.

[109] Breuer, M. and Rodi, W. Large-eddy simulation of complex turbulent flows of practical interest. In *Flow Simulation with High-Performance Computers II*, E. H. Hirschel, ed., Notes on Numerical Fluid Mechanics. Vol. 52. pp. 258–274. Vieweg Verlag, Braunschweig, 1996.

[110] Breuer, M. Large-eddy simulation of the sub-critical flow past a circular cylinder: numerical and modeling aspects. *International Journal for Numerical Methods in Fluids,* **28**, pp. 1281–1302, 1998.

[111] Breuer, M. A challenging test case for large-eddy simulation: high reynolds number circular cylinder flow. *International Journal for Numerical Methods in Fluids,* **21**(5), pp. 648–654, 2000.

[112] Breuer, M. and Jovičić, N. An LES investigation of the separated flow past an airfoil at high angle of attack. In *Proc. of the 4th Workshop on Direct and Large-Eddy Simulation, Enschede, The Netherlands, 18-20 July 2001*, B. J. Geurts, R. Friedrich, and O. Métais, eds., ERCOFTAC Series, Direct and Large-Eddy Simulation IV. Vol. 8. pp. 165–172. Kluwer Academic Publishers, Dordrecht, 2001.

[113] Rhie, C. M. and Chow, W. L. A numerical study of the turbulent flow past an isolated airfoil with trailing edge separation. *AIAA Journal,* **21**, pp. 1525–1532, 1983.

[114] Smagorinsky, J. General circulation experiments with the primitive equations. 1. the basic experiment. *Monthly Weather Review,* **91**, pp. 99–165, 1963.

[115] Menter, F. R. *Best Practice: Scale-Resolving Simulations in ANSYS CFD.* ANSYS Germany GmbH, Version 1.02. Otterfing, 2012.